A globally conservative finite element MHD code and its application to the study of compact torus formation, levitation and magnetic compression

Carl Dunlea[1,2,(a)], and Ivan Khalzov[2], General Fusion Team, Akira Hirose

[1]University of Saskatchewan, 116 Science Pl, Saskatoon, SK S7N 5E2, Canada
[2]General Fusion, 106 - 3680 Bonneville Pl, Vancouver, BC V3N 4T5, Canada
[(a)]Current address: Tokamak Energy Ltd., Milton Park, Oxfordshire, OX14 4SD, England. Author to whom correspondence should be addressed: cpd716@mail.usask.ca

Abstract

The DELiTE (Differential Equations on Linear Triangular Elements) framework was developed for spatial discretisation of partial differential equations on an unstructured triangular grid in axisymmetric geometry. The framework is based on discrete differential operators in matrix form, which are derived using linear finite elements and mimic some of the properties of their continuous counterparts. A single-fluid two-temperature MHD model is implemented in this framework. The inherent properties of the operators are used in the code to ensure global conservation of energy, particle count, toroidal flux, and (in some scenarios) angular momentum. The code was applied to study a novel experiment in which a compact torus (CT), produced with a magnetized Marshall gun, is magnetically levitated off an insulating wall and then magnetically compressed through the action of currents in the levitation/compression coils located outside the wall. We present numerical models for CT formation, levitation, and magnetic compression, and comparisons between simulated and experimental diagnostics.

1 Introduction

Ideally, a numerical discretisation method should, as well as accurately representing the continuous form of the mathematical equations that describe a particular physical system, reproduce the physical properties of the system being modelled. In practice, such properties are often expressed as conservation laws, and their maintenance can be just as important as standard numerical method assessment gauges like convergence, stability, accuracy, and range of applicability. Numerical solutions that contradict basic physical principles by, for example, destroying mass or energy are inherently unreliable when applied to novel physical regimes. On the other hand, many numerical methods do not have strong conservation properties, or conserve only some naturally conserved quantities, but can still regularly produce informative results that have a resemblance to real-world observations. However, as more complicated physical systems are modelled, physically incorrect numerical solutions can go unnoticed. This is especially true in simulating complex physical models, such as fluid dynamics or magnetohydrodynamics (MHD), where the maintenance of conservation laws puts more constraints on numerical schemes and, thus, helps to avoid spurious solutions. It is best to deal with the physical fidelity of the model at the numerical method design level [1], and try to

replicate, in the discretised form, as many of the conservation laws inherent to the original physical system as possible.

Numerical methods with discrete conservation properties are well known in computational fluid dynamics (for example, [1, 2, 3, 4]), and in computational MHD [5, 6, 7]. In this paper we present a novel numerical scheme for a two-dimensional (axisymmetric) compressible MHD system, which is based on a continuous Galerkin linear finite element method applied to an unstructured triangular mesh. By construction, the scheme has global (for the whole domain) conservation of mass, energy, toroidal flux and angular momentum. A novelty of the code is that all discrete spatial differential operators are represented as matrices, and the discretized MHD equations are obtained by simply replacing the original continuous differentiations with the corresponding matrix operators.

Note that by global conservation of a quantity in our numerical method, we imply that there is a discretised analogue of the continuity equation for that quantity, and, when integrated over the volume, its fluxes are completely cancelled in the interior of the domain, even though the explicit form of these fluxes are not always given. As shown in [8] and [1], global conservation for a method with local support (*i.e.*, local stencil) also implies local conservation. To enable the development of a numerical formulation with the aforementioned conservation properties, the discrete differential operators must obey a property equivalent, for a scalar field $u(\mathbf{r})$ and a vector field $\mathbf{p}(\mathbf{r})$, to

$$\int u \nabla \cdot \mathbf{p} \, dV + \int \mathbf{p} \cdot \nabla u \, dV = \int \nabla \cdot (u\mathbf{p}) \, dV = \int u\mathbf{p} \cdot d\mathbf{\Gamma} \tag{1.1}$$

so that the discrete forms of the differential product rule and divergence theorem are satisfied [9]. This is the essence of mimetic schemes, also known as support operator methods, to which this work is closely related [1, 10].

In section 2, we use the finite element method to derive various discrete differential matrix operators for a two-dimensional domain with axial symmetry in cylindrical coordinates, and discuss their properties. These operators satisfy the discrete form of equation 1.1, and constitute the base of the DELiTE (Differential Equations on Linear Triangular Elements) framework, which is implemented in MATLAB. In section 3, the discrete single-fluid two-temperature MHD equations are constructed within the framework. The formal process of equation development is detailed in [11]. Here, using inherent properties of the differential operators, we demonstrate global conservation of mass, toroidal flux, angular momentum, and energy. In section 4, an overview of the magnetic compression experiment is presented - more details can be found in [11, 12]. The magnetic compression experiment at General Fusion was a repetitive non-destructive test to study plasma physics applicable to magnetic target fusion compression. A compact torus (CT) is formed with a co-axial gun into a containment region with an hour-glass shaped inner flux conserver, and an insulating outer wall. External coil currents hold the CT off the outer wall (radial "levitation") and then rapidly compress it inwards. In section 5, we present the details of our numerical models for simulating CT formation, magnetic levitation, and compression within the DELiTE framework. The model includes coupling between the poloidal external vacuum field solution in the part of the domain representing the insulating wall, and the full MHD solutions in the remainder of the domain. In section 6, we present principal code input parameters and simulation results, and simulated diagnostics are compared with the experimentally measured counterparts. With inclusion of the insulating wall in the model, the effect of reduced plasma/wall interaction with an improved levitation/compression coil configuration, as observed in the experiment, is reproduced with MHD simulations. In the conclusion, section 7, we present a summary of principal code features and suggest possible further extensions. A detailed derivation of the first order node-to-element differential operator is presented in Appendix A. Further node-to element and node-to-node operator identities are demonstrated in Appendices B and C respectively. In Appendix D, it is shown how energy and momentum conservation can be maintained when artificial density diffusion is included in the model.

2 Finite element discretisation and differential operators

In this section, we start with a brief description of the discretisation and finite element method, and introduce notations, then we derive several types of discrete differential operators used in the code and discuss their properties.

2.1 Discretisation and finite element method overview

The two-dimensional computational domain, with azimuthal symmetry in cylindrical coordinates, is represented by an unstructured triangular mesh. To develop the finite element discretisation, we drew inspiration from material presented in [13], which in turn, is based on material in [14], in which a finite element method is used to solve Laplace and Poisson equations in two dimensions. The freely-available mesh generator DISTMESH [15, 16, 17] was adapted to provide the computational grid. Nodes are located at triangle vertices. In the linear finite element method, any continuous function $u(\mathbf{r})$ is approximated as a piecewise continuous function $U(\mathbf{r})$ that is linear across each triangular element:

$$u(\mathbf{r}) \approx U(\mathbf{r}) = \sum_{e=1}^{N_e} U^e(\mathbf{r}) \tag{2.1}$$

where N_e is the number of elements, and $U^e(\mathbf{r})$ is the contribution to $U(\mathbf{r})$ from within element e:

$$U^e(\mathbf{r}) = A^e + B^e r + C^e z \tag{2.2}$$

Here, A^e, B^e and C^e are constants that are specific to element e. The mechanics of the derivations of these coefficients is presented briefly in in appendix A, and an overview of the matrix operator asssembly is shown. Equivalent to equation 2.1, $U(\mathbf{r})$ may be defined using a combination of basis functions as

$$u(\mathbf{r}) \approx U(\mathbf{r}) = \sum_{n=1}^{N_n} U_n \, \phi_n(\mathbf{r}) \tag{2.3}$$

where N_n is the number of nodes, U_n represents the values of $U(\mathbf{r})$ at node n, and $\phi_n(\mathbf{r}) \equiv \phi_n(r, z)$ is the basis function associated with node n.
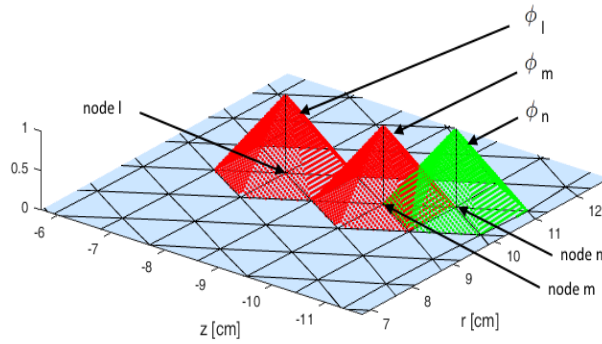

Figure 1: Linear basis function depiction for triangular elements

The linear basis functions have the forms of pyramids, as depicted in figure 1, which indicates a portion of a computation mesh, with depictions of the basis functions for example nodes l, m and n. Each node n

is associated with a pyramid function ϕ_n, which has an elevation of one above the node, and falls linearly to zero at the immediately surrounding nodes. Each pyramid function ϕ_n has e_n sides, where e_n is the node-specific number of triangular elements surrounding node n. Note that the pyramid shapes associated with basis functions for nodes on the domain boundary have, in addition, one or more vertical sides at the boundaries. The remaining individual pyramid-side functions are defined by sections of planes that are tilted relative to the $r - z$ plane. Thus, each node is associated with e_n tilted planes. In total, there are K tilted planes defined in the solution domain, where $K = \sum\limits_{n=1}^{N_n} e_n = 3N_e$. Each triangular element is associated with three tilted planes. The tilted planes are truncated to constitute pyramid sides by defining the functions representing the pyramid sides as

$$\psi_n^e(\mathbf{r}) = a_n^e + b_n^e r + c_n^e z \tag{2.4}$$

with the additional truncating property that $\psi_n^e(\mathbf{r}) = 0$ for all points located at $\mathbf{r}$ which lie outside the triangular element associated with ψ_n^e. The notation ψ_n^e indicates that each pyramid side function is associated with a particular node n, *and* with a particular triangular element e. The coefficients a_n^e, b_n^e, and c_n^e are also associated with a particular node and element, and are such that $\psi_n^e = 1$ at its associated node n, and $\psi_n^e = 0$ at the other two nodes in the triangular element e. In summary, the basis functions $\phi_n(\mathbf{r})$, which define pyramid shapes with a peak elevation of one at node n, can be expressed as

$$\phi_n(\mathbf{r}) = \overset{e_n}{\Sigma} \psi_n^e(\mathbf{r}) \tag{2.5}$$

where the summation is over the pyramid side functions associated with node n, each of which is non-zero only over its associated triangular element. The basis functions have the property that $\phi_n(r_j, z_j) = \delta_{nj}$, where δ_{nj} is the Kronecker delta, and (r_j, z_j) are the coordinates of node j. Noting that the volume of a pyramid is given by $V_{pyramid} = sH/3$, where s is the pyramid base area and H is the pyramid height, this leads naturally, for any continuous function $U(\mathbf{r})$ (including the piecewise linear approximation), to the property

$$\int \phi_n(\mathbf{r}) \, U(\mathbf{r}) \, dr \, dz = (U_n + \mathcal{O}(h_e)) \int \phi_n(\mathbf{r}) \, dr \, dz \approx \frac{U_n \, s_n}{3} \tag{2.6}$$

where $U_n = U(r_n, z_n)$, s_n is the support area of node n (area of the base of the pyramid function defined by $\phi_n(\mathbf{r})$), pyramid height $H = 1$, and h_e is the typical element size. This identity is analogous to the integral property of the Dirac delta function. In deriving the property, it is assumed that the function $U(\mathbf{r})$ is sufficiently smooth that it is approximately constant (to order h_e) in the support area of node n. We neglect the term of order h_e because our numerical scheme has overall the first order accuracy, as defined by the use of linear basis functions.

Another important property of the basis functions is related to partition of unity - the sum of all the basis functions in the domain, at any point in the domain (*i.e.*, at non-nodal locations, as well as at nodal locations), is equal to one. This property also hold for the pyramid side functions, *i.e.*, $\overset{N_n}{\underset{n=1}{\Sigma}} \phi_n(\mathbf{r}) = \overset{N_n}{\underset{n=1}{\Sigma}} \psi_n(\mathbf{r}) = 1$.

2.2   Notations for matrices and operations

The notation $\overline{X}$ (or $\overline{x}$) is used to denote vectors of dimensions $[N_n \times 1]$ that contain node-associated quantities, while $\widehat{X} [N_e \times 1]$ denotes vectors of element-associated quantities. The notation $\widehat{\overline{X}}$ will be used to denote matrices of dimensions $[N_e \times N_n]$ that operate on vectors of nodal quantities $\overline{X}$, to produce vectors of elemental quantities $\widehat{Y}$, while $\overline{\widehat{X}} [N_n \times N_e]$ operates on vectors of elemental quantities $\widehat{X}$ to produce

vectors of nodal quantities $\overline{Y}$. Finally, $\overline{\overline{X}}$ and $\widehat{\widehat{X}}$ denote square matrices with dimensions $[N_n \times N_n]$ and $[N_e \times N_e]$ respectively. Notations defining the various matrix dimensions are collected in table 1.

		# columns		
		1	N_n	N_e
# rows	N_n	$\overline{X}$	$\overline{\overline{X}}$	$\widehat{\overline{X}}$
	N_e	$\widehat{X}$	$\overline{\widehat{X}}$	$\widehat{\widehat{X}}$

Table 1: Notations for matrices of various dimensions

Defining operation notations, a space between two arrays of equal size represents the Hadamard product, piecewise element-by element multiplication (*e.g.*, $(\overline{a}\,\overline{b})_i = a_i b_i$), and the symbol / represents Hadamard division, piecewise element-by element division (*e.g.*, $(\overline{a}\,/\,\overline{b})_i = a_i/b_i$). The symbol $*$ between two matrices (*e.g.*, $\overline{\overline{C}} = \overline{\overline{A}} * \overline{\overline{B}}$) implies regular matrix multiplication. The superscript T implies the transpose operation, *e.g.*, $\overline{\overline{B}} = \overline{\overline{A}}^T$, and the superscript -1 implies the inverse operation.

2.3 Element-node mapping operators

The connectivity operator $\widehat{\overline{M}}$, used to map between nodal and elemental quantities, has dimensions $[N_e \times N_n]$. Each row of $\widehat{\overline{M}}$ corresponds to a particular triangular element, and has only three non-zero entries. $\widehat{\overline{M}}(e,\,n) = 1$ for the column indexes n corresponding to the indexes n of the nodes located at the vertices of the triangle with index e. We introduce node-to-element averaging as

$$< \overline{X} >^e = \frac{1}{3}\widehat{\overline{M}} * \overline{X} \tag{2.7}$$

For example, the radial coordinates of the element centroids are defined with $\widehat{r} = (r_1^e, r_2^e, ...r_{N_e}^e)^T = < \overline{r} >^e$, where $\overline{r} = (r_1, r_2, ...r_{N_n})^T$ contains the radial coordinates of the nodes. Similarly, the axial centroid coordinates are defined as $\widehat{z} = < \overline{z} >^e$. The vector of nodal support areas $\overline{s}$, containing the areas of the bases of the pyramid functions associated with the nodes, is related to $\widehat{s}$, the vector of elemental areas, as $\overline{s} = \widehat{\overline{M}}^T * \widehat{s}$.

Volume integrals over the computational domain can be approximated in two ways, corresponding to nodal or elemental representations of the integrand function

$$\int u(\mathbf{r})\,dV \approx \overline{dV}^T * \overline{U} \quad \text{or} \quad \int u(\mathbf{r})\,dV \approx \widehat{dV}^T * \widehat{U}$$

where $\overline{dV} = \frac{2\pi}{3}\overline{s}\,\overline{r}$ contains the volumes associated with each node, which are found by integrating the node-associated areas from 0 to 2π in the toroidal direction, and $\widehat{dV} = 2\pi\,\widehat{s}\,\widehat{r}$ contains the elemental volumes. The factor of three in the former expression arises because each elemental area is shared by three nodes. Note that these two approximations do not give identical results for vectors related by equation 2.7, unless the original integrand function $u(\mathbf{r})$ is constant.

Defining $\overline{\overline{R}}$, $\overline{\overline{S}}$, $\widehat{\widehat{R}}$ and $\widehat{\widehat{S}}$ as the diagonal arrays constructed from $\overline{r}$, $\overline{s}$, $\widehat{r}$, and $\widehat{s}$, we define a volume-averaging operator

$$\widehat{\overline{W}} = \overline{\overline{R}}^{-1} * \overline{\overline{S}}^{-1} * \widehat{\overline{M}}^T * \widehat{\widehat{S}} * \widehat{\widehat{R}}$$

that is used to map element-based quantities to node-based quantities, as

$$< \widehat{U} > = \overline{\widehat{W}} * \widehat{U} \tag{2.8}$$

This operator satisfies the following identity:

$$\overline{dV}^T * \left(\overline{Q} \left(\overline{\widehat{W}} * \widehat{U} \right) \right) = \widehat{dV}^T * \left(\widehat{Q} \ \widehat{U} \right) \tag{2.9}$$

where $\widehat{U}$ and $\widehat{Q}$ are the discrete representations, defined at the element centroids, of the approximations to the continuous functions $u(\mathbf{r})$ and $q(\mathbf{r})$, and $\overline{Q}$ is the discrete representation, defined at the nodes, of $q(\mathbf{r})$, and is related to $\widehat{Q}$ by equation 2.7. A proof of this identity follows:

$$
\begin{aligned}
\overline{dV}^T * \left(\overline{Q} \left(\overline{\widehat{W}} * \widehat{U} \right) \right) &= \frac{2\pi}{3} \left(\overline{s} \ \overline{r} \right)^T * \left(\overline{Q} \left(\overline{\overline{R}}^{-1} * \overline{\overline{S}}^{-1} * \overline{\widehat{M}}^T * \widehat{S} * \widehat{R} * \widehat{U} \right) \right) \\
&= \frac{2\pi}{3} \overline{Q}^T * \left(\overline{\widehat{M}}^T * \widehat{S} * \widehat{R} * \widehat{U} \right) \\
&= 2\pi \left(\widehat{S} * \widehat{R} * \widehat{U} \right)^T * \left(\frac{1}{3} \overline{\widehat{M}} * \overline{Q} \right) && \text{(transpose the scalar)} \\
&= \widehat{dV}^T * \left(\widehat{Q} \ \widehat{U} \right) && \text{(use equation 2.7)}
\end{aligned}
$$

Note that the matrix transpose relation

$$\left(\mathbb{A} * \mathbb{B} \right)^T = \mathbb{B}^T * \mathbb{A}^T \tag{2.10}$$

for matrices $\mathbb{A}$ and $\mathbb{B}$, is used to transpose the scalar on the right side of the equation in the second last step of the derivation above. In the particular case with $\overline{Q} = \overline{1}$, the identity becomes

$$\overline{dV}^T * \left(\overline{\widehat{W}} * \widehat{U} \right) = \widehat{dV}^T * \widehat{U} \tag{2.11}$$

2.4 First order node-to-element differential operators
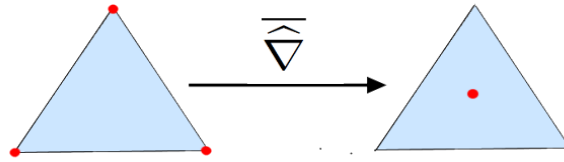

Figure 2: Node-to-element differential operator mechanism

The node-to-element derivative operator matrices are defined such that

$$\widehat{U}'_r = \overline{\widehat{Dr}} * \overline{U}$$
$$\widehat{U}'_z = \overline{\widehat{Dz}} * \overline{U}$$

Referring for example to the radial derivative operator, application of $\overline{\widehat{Dr}}$, a matrix with dimensions $[N_e \times N_n]$, to the vector $\overline{U}$, returns $\widehat{U}'_r$ $[N_e \times 1]$, containing the values for the radial derivatives of $U(\mathbf{r})$

inside the triangular elements. The node-to-element gradient and divergence operations, for cylindrical coordinates with azimuthal symmetry are

$$\overline{\overline{\nabla}} \, \overline{U} = \left(\overline{\overline{Dr}} * \overline{U} \right) \hat{\mathbf{r}} + \left(\overline{\overline{Dz}} * \overline{U} \right) \hat{\mathbf{z}} \tag{2.12}$$

and

$$\overline{\overline{\nabla}} \cdot \mathbf{P} = \left(\left(\overline{\overline{Dr}} * \left(\overline{r} \, \overline{P}_r \right) \right) + \left(\overline{\overline{Dz}} * \left(\overline{r} \, \overline{P}_z \right) \right) \right) / \widehat{r}$$

where where $\hat{\mathbf{r}}$ and $\hat{\mathbf{z}}$ are the unit vectors in the radial and axial directions, and $\overline{P}_r$ and $\overline{P}_z$ are the nodal representations of the r and z components the continuous vector field $\mathbf{p}(\mathbf{r})$. A schematic of the node-to-element gradient operation mechanism is indicated in figure 2. To derive the $\widehat{\overline{Dr}}$ and $\widehat{\overline{Dz}}$ operators we use the elemental representation of $U(\mathbf{r})$, equations 2.1 and 2.2. Equation 2.2 defines the values of the contributions to $U(\mathbf{r})$ at the nodes of a particular element as

$$U_\varepsilon^e = A^e + B^e r_\varepsilon + C^e z_\varepsilon \tag{2.13}$$

where $\varepsilon = i$, j, k denotes the indexes of the nodes at the vertices of triangular element e. As shown in appendix A, the expressions for the spatial derivatives of $U(\mathbf{r})$ at the interior of each element are:

$$\frac{\partial U^e}{\partial r} = \sum_\varepsilon U_\varepsilon^e b_\varepsilon^e$$
$$\frac{\partial U^e}{\partial z} = \sum_\varepsilon U_\varepsilon^e c_\varepsilon^e \tag{2.14}$$

where the coefficients b_ϵ^e and c_ϵ^e are defined in equation 2.4. $\overline{\overline{Dr}}$ and $\overline{\overline{Dz}}$ are initially defined as sparse all-zero arrays. The values b_i^e, b_j^e and b_k^e are inserted in row e of $\overline{\overline{Dr}}$ with placements at the column indexes i, j, k. Similarly, the values c_i^e, c_j^e and c_k^e, for each element, are used to assemble $\overline{\overline{Dz}}$. The resulting derivative operators produce exact derivatives for nodal functions with linear dependence on r and z, and have first order accuracy (*i.e.*, $\mathcal{O}(h_e)$) when applied to nonlinear functions. The operators introduced in the following subsections are all based on these node-to-element derivative operators, and so they all have the same accuracy.

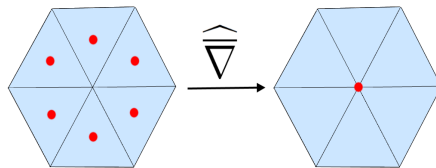## 2.5 First order element-to-node differential operators

Figure 3: Element-to-node differential operator mechanism

The element-to-node derivative operator matrices are defined such that

$$\overline{U}'_r = \widehat{\overline{Dr}} * \widehat{U}$$
$$\overline{U}'_z = \widehat{\overline{Dz}} * \widehat{U}$$

Referring for example to the radial derivative operator, application of the $\widehat{\overline{Dr}}$ operator, which is a matrix with dimensions $[N_n \times N_e]$, to the vector $\widehat{U}$ $[N_e \times 1]$, which contains the values of $U(\mathbf{r})$ at the element centroids, returns $\overline{U}'_r$ $[N_n \times 1]$, the values for the radial derivatives of $U(\mathbf{r})$ at the nodes. The element-to-node gradient and divergence operations, for cylindrical coordinates with azimuthal symmetry are

$$\widehat{\overline{\nabla}}\,\widehat{U} = \left(\widehat{\overline{Dr}} * \widehat{U}\right)\hat{\mathbf{r}} + \left(\widehat{\overline{Dz}} * \widehat{U}\right)\hat{\mathbf{z}} \tag{2.15}$$

and

$$\widehat{\overline{\nabla}}\cdot\widehat{\mathbf{P}} = \left(\left(\widehat{\overline{Dr}} * \left(\hat{r}\,\widehat{P}_r\right)\right) + \left(\widehat{\overline{Dz}} * \left(\hat{r}\,\widehat{P}_z\right)\right)\right) / \overline{r} \tag{2.16}$$

A schematic of the element-to-node gradient operation mechanism is indicated in figure 3. The element-to-node differential operators are derived in relation to the node-to-element operators by requiring the discrete form of equation 1.1 to hold:

$$\overline{dV}^T * \left[\mathbf{P}\cdot\left(\widehat{\overline{\nabla}}\,\widehat{U}\right)\right] + \widehat{dV}^T * \left[\widehat{U}\,\left(\widehat{\overline{\nabla}}\cdot\mathbf{P}\right)\right] = 0 \tag{2.17}$$

or

$$\overline{dV}^T * \left[\overline{U}\,\left(\widehat{\overline{\nabla}}\cdot\widehat{\mathbf{P}}\right)\right] + \widehat{dV}^T * \left[\widehat{\mathbf{P}}\cdot\left(\widehat{\overline{\nabla}}\,\overline{U}\right)\right] = 0 \tag{2.18}$$

In this derivation, it is assumed that the boundary term $\int u\mathbf{p}\cdot d\mathbf{\Gamma} = 0$, *i.e.*, there is no flux of the continuous vector field $u\mathbf{p}$ through the boundary. For arbitrary discrete nodal representations $\overline{\mathbf{P}}$ (equation 2.17) and $\overline{U}$ (equation 2.18), a consequence of this assumption is that the element-to-node gradient operator produces valid results at the boundary nodes only if the original continuous function u is zero at the boundary (*i.e.*, $u|_\Gamma = 0$). Similarly, the element-to-node divergence operator produces valid results at the boundary nodes only if the original continuous function $\mathbf{p}$ has no component perpendicular to the boundary (*i.e.*, $\mathbf{p}_\perp|_\Gamma = 0$). In the following, we will refer to these conditions as the natural boundary conditions. For the terms involving radial derivatives, equation 2.18 implies that

$$\overline{dV}^T * \left(\overline{U}\,\left(\left(\widehat{\overline{Dr}} * \left(\hat{r}\,\widehat{P}_r\right)\right) / \overline{r}\right)\right) \quad = -\widehat{dV}^T * \left(\widehat{P}_r\,\left(\overline{\overline{Dr}} * \overline{U}\right)\right)$$
$$\Rightarrow \frac{2\pi}{3}\overline{s}^T * \left(\overline{U}\,\left(\widehat{\overline{Dr}} * \left(\hat{r}\,\widehat{P}_r\right)\right)\right) \quad = -2\pi\,\hat{s}^T * \left(\hat{r}\,\widehat{P}_r\,\left(\overline{\overline{Dr}} * \overline{U}\right)\right)$$
$$\Rightarrow \frac{1}{3}\overline{U}^T * \left(\overline{\overline{S}} * \left(\widehat{\overline{Dr}} * \left(\hat{r}\,\widehat{P}_r\right)\right)\right) \quad = -\left(\hat{r}\,\widehat{P}_r\right)^T * \left(\widehat{\overline{S}} * \overline{\overline{Dr}} * \overline{U}\right)$$
$$\Rightarrow \frac{1}{3}\overline{U}^T * \left(\overline{\overline{S}} * \left(\widehat{\overline{Dr}} * \left(\hat{r}\,\widehat{P}_r\right)\right)\right) \quad = -\overline{U}^T * \left(\overline{\overline{Dr}}^T * \widehat{\overline{S}} * \left(\hat{r}\,\widehat{P}_r\right)\right) \qquad \text{(transpose scalar on RHS)}$$

Hence, the element-to-node derivative operators are

$$\widehat{\overline{Dr}} = -3\overline{\overline{S}}^{-1} * \left(\overline{\overline{Dr}}^T * \widehat{\overline{S}}\right)$$
$$\widehat{\overline{Dz}} = -3\overline{\overline{S}}^{-1} * \left(\overline{\overline{Dz}}^T * \widehat{\overline{S}}\right) \tag{2.19}$$

These definitions can alternatively be obtained using equation 2.17. Noting the particular case when $\overline{U} = \overline{1}$, then equation 2.18 leads to the identity

$$\overline{dV}^T * \left[\widehat{\overline{\nabla}}\cdot\widehat{\mathbf{P}}\right] = 0 \tag{2.20}$$

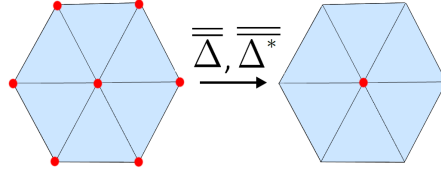## 2.6 Second order node-to-node differential operators

Figure 4: Node-to-node second order differential operator mechanism

Discrete forms of node-to-node second order differential operators, with dimensions $[N_n \times N_n]$, can be constructed using combinations of the first order node-to-element and element-to-node operators. For example, the discrete form of the Laplacian operator in cylindrical coordinates, with azimuthal symmetry, is

$$\overline{\overline{\Delta}}\ \overline{U} = \widehat{\overline{\nabla}} \cdot \widehat{\overline{\nabla}}\ \overline{U} = \left(\left(\widehat{\overline{Dr}} * \left(\widehat{r}\ \left(\widehat{\overline{Dr}} * \overline{U} \right) \right) \right) + \left(\widehat{\overline{Dz}} * \left(\widehat{r}\ \left(\widehat{\overline{Dz}} * \overline{U} \right) \right) \right) \right) / \overline{r} \tag{2.21}$$

Note that $\overline{\overline{\Delta}}\ \overline{U}$ may be expressed as $\widehat{\overline{\nabla}} \cdot \widehat{\mathbf{P}}$, where $\widehat{\mathbf{P}} = \widehat{\overline{\nabla}}\ \overline{U}$. Therefore, equation 2.20 implies that

$$\overline{dV}^T * \left[\overline{\overline{\Delta}}\ \overline{U} \right] = 0 \tag{2.22}$$

The condition $\mathbf{p}_\perp|_\Gamma = 0$, required for correct evaluation of $\widehat{\overline{\nabla}} \cdot \widehat{\mathbf{P}}$ at the boundary nodes, is equivalent to having the normal component of the gradient of the continuous function u equal to zero at the boundary. Thus, the operation $\overline{\overline{\Delta}} * \overline{U}$ produces correct results at the boundary nodes only if the natural boundary condition is satisfied, which in this case is $(\nabla_\perp u)|_\Gamma = 0$.

The discrete form of the elliptic operator used in the Grad-Shafranov equation, in cylindrical coordinates with azimuthal symmetry is

$$\overline{\overline{\Delta^*}}\ \overline{U} = \overline{r}^2\ \left(\widehat{\overline{\nabla}} \cdot \left(\left(\widehat{\overline{\nabla}}\ \overline{U} \right) / \widehat{r}^2 \right) \right) = \overline{r}\ \left(\widehat{\overline{Dr}} * \left(\left(\widehat{\overline{Dr}} * \overline{U} \right) / \widehat{r} \right) + \widehat{\overline{Dz}} * \left(\left(\widehat{\overline{Dz}} * \overline{U} \right) / \widehat{r} \right) \right) \tag{2.23}$$

The $\overline{\overline{\Delta}}$ and $\overline{\overline{\Delta^*}}$ operator mechanisms are indicated in figure 4. Note that equation 2.20 implies that

$$\overline{dV}^T * \left[\left(\overline{\overline{\Delta^*}}\ \overline{U} \right) / \overline{r}^2 \right] = 0 \tag{2.24}$$

Again, the operation $\overline{\overline{\Delta^*}}\ \overline{U}$ produces correct results at the boundary nodes only if the natural boundary condition is satisfied, which in this case is $\left((\nabla_\perp u) / r^2 \right)|_\Gamma = 0$. As shown in [11], the standard Galerkin method may be used to derive these second order node-to-node differential operators directly.

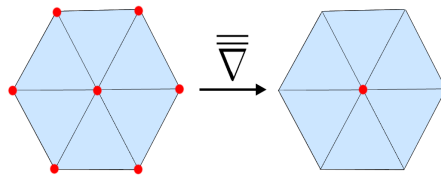## 2.7 First order node-to-node differential operators

Figure 5: Node-to-node differential operator mechanism

The node-to-node derivative operator matrices $\overline{\overline{Dr}}$ and $\overline{\overline{Dz}}$, with dimensions $[N_n \times N_n]$, are used to evaluate, at the nodes, the radial and axial derivatives of any function $U(\mathbf{r})$ that is defined at the nodes, and are defined as

$$\overline{U}'_r = \overline{\overline{Dr}} * \overline{U}$$
$$\overline{U}'_z = \overline{\overline{Dz}} * \overline{U}$$

The node-to-node gradient and divergence operations, for cylindrical coordinates with azimuthal symmetry are

$$\overline{\overline{\nabla}} \, U = \left(\overline{\overline{Dr}} * \overline{U}\right) \hat{\mathbf{r}} + \left(\overline{\overline{Dz}} * \overline{U}\right) \hat{\mathbf{z}} \tag{2.25}$$

and

$$\overline{\overline{\nabla}} \cdot \mathbf{P} = \left(\left(\overline{\overline{Dr}} * \left(\overline{r} \ \overline{P}_r\right)\right) + \left(\overline{\overline{Dz}} * \left(\overline{r} \ \overline{P}_z\right)\right)\right) / \overline{r} \tag{2.26}$$

A schematic of the node-to-node gradient operation mechanism is indicated in figure 5. Here, we will look at the derivation of $\overline{\overline{Dr}}$, the derivation of $\overline{\overline{Dz}}$ is analogous. The node-to-node operators can be expressed in terms of the node-to-element operators by considering the expansion of $U(\mathbf{r})$ in terms of the piecewise-linear functions $U^e(\mathbf{r})$:

$$U(\mathbf{r}) = \underset{e}{\Sigma} U^e(\mathbf{r})$$

This implies that

$$U'_r(\mathbf{r}) = \underset{e}{\Sigma} U^{e'}_r(\mathbf{r})$$

Applying the Galerkin method, we obtain

$$\int \phi_j(\mathbf{r}) \, U'_r(\mathbf{r}) \, dr \, dz = \int \phi_j(\mathbf{r}) \, \underset{e}{\Sigma} U^{e'}_r(\mathbf{r}) \, dr \, dz \tag{2.27}$$

where integral is taken over the support area of the basis function $\phi_j(\mathbf{r})$. Note that $U^{e'}_r = B^e$ (equation 2.2). Expanding the right side of equation 2.27 in terms of pyramid side functions according to equation 2.5, and using equation 2.6 to expand the left side, this implies that

$$\frac{U'_{rj} s_j}{3} = \overset{e_j}{\Sigma} \int \psi^e_j(\mathbf{r}) \, B^e \, dr \, dz$$
$$= \overset{e_j}{\Sigma} B^e \int \psi^e_j(\mathbf{r}) \, dr \, dz$$
$$= \overset{e_j}{\Sigma} B^e \frac{s^e}{3}$$

Therefore, in our method the derivative at a node is defined as the area-weighted average of the elemental derivatives in the support of that node. With use of connectivity operator $\widehat{\overline{M}}$, this definition can be written as:

$$\overline{U}'_r = \left(\overline{\overline{S}}^{-1} * \left(\widehat{\overline{M}}^T * \widehat{\overline{S}} * \widehat{\overline{Dr}}\right)\right) * \overline{U}$$
$$\Rightarrow \overline{\overline{Dr}} = \overline{\overline{S}}^{-1} * \left(\widehat{\overline{M}}^T * \widehat{\overline{S}} * \widehat{\overline{Dr}}\right) \tag{2.28}$$

The derivation of $\overline{\overline{Dz}}$ follows from that of $\overline{\overline{Dr}}$, with $\overline{\overline{Dz}} = \left(\overline{\overline{S}}^{-1} * \left(\widehat{\overline{M}}^T * \widehat{\overline{S}} * \widehat{\overline{Dz}}\right)\right)$.

The element-to-node differential operators are defined from the basic node-to-element counterpart operators by enforcing the disrete form of the combined expression for the divergence therorem and the differential product rule (equation 1.1). The node to node differential operators obey the same laws:

$$\overline{dV^T} * \left[\left(\overline{U} \ \left(\overline{\overline{\nabla}} \cdot \mathbf{P} \right) + \left(\overline{\overline{\nabla}} \ \overline{U} \right) \cdot \mathbf{P} \right) \right] = 0 \qquad \left(\text{if } \overline{U} \,|_\Gamma = 0 \text{ or } \mathbf{P}_\perp |_\Gamma = 0 \right) \qquad (2.29)$$

For the particular case of $\overline{U} = \overline{1}$, this implies that

$$\overline{dV^T} * \left[\overline{\overline{\nabla}} \cdot \mathbf{P} \right] = \overline{0} \qquad \left(\text{if } \mathbf{P}_\perp |_\Gamma = 0 \right) \qquad (2.30)$$

More details and the proof can be found in appendix C.

3 Discrete form of MHD equations and conservation laws

In this section we present the discretised equations for a two-temperature MHD model, which are constructed so as to preserve the global conservation laws inherent to the original continuous system of equations.

3.1 Axisymmetric two-temperature MHD model

A two-temperature plasma MHD model, in which the electrons and ions are allowed to have different temperatures, is a compromise between the single-fluid and two-fluid MHD models. It has the relative computational simplicity of the single-fluid model, but from the energy point of view it treats electrons and ions as two separate fluids, and allows implementation of different thermal diffusion coefficients for the electrons and ions. In the following, SI units will be used, but temperatures will be expressed in Joules unless otherwise indicated. The continuous forms of the two-temperature MHD equations are:

$$\dot{n} = -\nabla \cdot (n\mathbf{v}) \qquad (3.1)$$

$$\dot{\mathbf{v}} = -\mathbf{v} \cdot \nabla \mathbf{v} + \frac{1}{\rho} \left(-\nabla p - \nabla \cdot \underline{\boldsymbol{\pi}} + \mathbf{J} \times \mathbf{B} \right) \qquad (3.2)$$

$$\dot{p}_i = -\mathbf{v} \cdot \nabla p_i - \gamma p_i \nabla \cdot \mathbf{v} + (\gamma - 1) \left(-\nabla \cdot \mathbf{q}_i + Q_{ie} - \underline{\boldsymbol{\pi}} : \nabla \mathbf{v} \right) \qquad (3.3)$$

$$\dot{p}_e = -\mathbf{v} \cdot \nabla p_e - \gamma p_e \nabla \cdot \mathbf{v} + (\gamma - 1) \left(-\nabla \cdot \mathbf{q}_e - Q_{ie} + \eta' \mathbf{J}^2 \right) \qquad (3.4)$$

$$\dot{\mathbf{B}} = \nabla \times (\mathbf{v} \times \mathbf{B}) - \nabla \times (\eta \nabla \times \mathbf{B}), \ \nabla \cdot \mathbf{B} = 0 \qquad (3.5)$$

Here, a dot above a symbol implies a partial time derivative, μ_0 is the magnetic constant, $\eta' [\Omega - \mathrm{m}]$ is the plasma resistivity, $\eta [\mathrm{m}^2/\mathrm{s}] = \eta'/\mu_0$ is magnetic diffusivity, and the adiabatic index $\gamma = \frac{5}{3}$ is the same for

ions and electrons. Note that n is the ion number density, so that the electron number density is $n_e = Zn$, where Z is the (volume averaged) ion charge, and $\rho = m_i n$ is the plasma fluid mass density. We assume ideal gas laws for ions and electrons:

$$\begin{aligned} p_i &= nT_i \\ p_e &= ZnT_e \end{aligned} \tag{3.6}$$

Total plasma fluid pressure is $p = p_i + p_e$. The remaining notations are standard. The boundary conditions and closure for this model (namely, definitions of thermal fluxes $\mathbf{q}_i$ and $\mathbf{q}_e$, viscous stress tensor $\underline{\boldsymbol{\pi}}$ and ion-electron heat exchange rate Q_{ie}) will be discussed in section 3.2.

With axisymmetry, the magnetic field can be represented in divergence-free form with the poloidal flux (per radian) function $\psi(r, z)$ and toroidal function $f(r, z) = rB_\phi$ as

$$\mathbf{B} = \nabla\psi \times \nabla\phi + f\nabla\phi \tag{3.7}$$

In this case, the current density is

$$\mathbf{J} = \frac{1}{\mu_0}\nabla \times \mathbf{B} = \frac{1}{\mu_0}\left(-\Delta^*\psi\,\nabla\phi + \nabla f \times \nabla\phi\right) \tag{3.8}$$

and the Lorentz force is

$$\mathbf{J} \times \mathbf{B} = -\frac{1}{\mu_0 r^2}\left(\Delta^*\psi\,\nabla\psi + f\,\nabla f\right) + \frac{\mathbf{B}\cdot\nabla f}{\mu_0 r}\hat{\boldsymbol{\phi}} \tag{3.9}$$

Using an axisymmetric representation of magnetic field, the magnetic induction equation 3.5 can be rewritten as

$$\begin{aligned} \dot{\psi} &= -\mathbf{v}\cdot\nabla\psi + \eta\Delta^*\psi \tag{3.10} \\ \dot{f} &= r^2\nabla\cdot\left(-\left(\frac{f}{r^2}\mathbf{v}\right) + \omega\mathbf{B} + \frac{\eta}{r^2}\nabla f\right) \tag{3.11} \end{aligned}$$

where $\omega = v_\phi/r$ is the plasma fluid angular speed.

3.1.1 Conservation properties (continuous equations)

The system described by equations 3.1-3.4, 3.10, 3.11 has a number of exact conservation laws expressed by corresponding continuity equations. The obvious one is conservation of particles, expressed by equation 3.1, with the boundary condition $\mathbf{v}_\perp|_\Gamma = 0$, corresponding to impermeable walls, where the subscript $\perp$ implies the component perpendicular to the boundary. Another conserved quantity is toroidal flux, defined as

$$\Phi = \int B_\phi\,dr\,dz = \int \frac{f}{r}\,dr\,dz = \frac{1}{2\pi}\int \frac{f}{r^2}2\pi r\,dr\,dz = \frac{1}{2\pi}\int \frac{f}{r^2}\,dV$$

Equation 3.11 implies that the rate of change of system toroidal flux is

$$\dot{\Phi} = \frac{1}{2\pi}\int \nabla\cdot\left(-\frac{f}{r^2}\mathbf{v} + \omega\mathbf{B} + \frac{\eta}{r^2}\nabla f\right)dV = \frac{1}{2\pi}\int\left(-\frac{f}{r^2}\mathbf{v} + \omega\mathbf{B} + \frac{\eta}{r^2}\nabla f\right)\cdot d\boldsymbol{\Gamma} \tag{3.12}$$

With appropriate boundary conditions, for example $\mathbf{v}|_\Gamma = \mathbf{0}$ and $(\nabla_\perp f)|_\Gamma = 0$, or $\mathbf{v}_\perp|_\Gamma = \mathbf{0}$ and $\left(B_{\theta\perp}\,v_\phi + \eta\left(\frac{\nabla_\perp f}{r}\right)\right)|_\Gamma = 0$, toroidal flux is conserved. Note that the electric field at the system boundary is

$$\mathbf{E}|_\Gamma = (-\mathbf{v} \times \mathbf{B} + \eta \nabla \times \mathbf{B})|_\Gamma$$
$$= (-\mathbf{v}_\phi \times \mathbf{B}_\theta - \mathbf{v}_\theta \times \mathbf{B}_\phi - \mathbf{v}_\theta \times \mathbf{B}_\theta + \eta(-\Delta^*\psi\,\nabla\phi + \nabla f \times \nabla\phi))|_\Gamma \qquad \text{(use eqn. 3.8)}$$
$$= \left(-\mathbf{v}_\phi \times \left(\mathbf{B}_{\theta\|} + \mathbf{B}_{\theta\perp}\right) - B_\phi\left(\mathbf{v}_{\theta\perp} + \mathbf{v}_{\theta\|}\right) \times \hat{\boldsymbol\phi} + (\mathbf{v}\cdot\nabla\psi)\nabla\phi + \eta\left(-\Delta^*\psi\,\nabla\phi + \frac{\nabla f}{r}\times\hat{\boldsymbol\phi}\right)\right)|_\Gamma$$

Here, the subscript $\|$ implies the component parallel to the boundary. Hence, the poloidal component of the electric field parallel to the boundary is

$$E_{\theta\|}|_\Gamma = \left(B_{\theta\perp}\,v_\phi - B_\phi\,v_{\theta\perp} + \eta\frac{\nabla_\perp f}{r}\right)|_\Gamma \qquad (3.13)$$

Therefore, either of the sets of boundary conditions listed above for toroidal flux conservation correspond to having the poloidal component of the electric field perpendicular to the boundary, the condition, in the case of azimuthal symmetry, for perfectly electrically conducting walls.

Conservation of angular momentum is established after noting that in the axisymmetric case

$$(\mathbf{v}\cdot\nabla\mathbf{v})_\phi = v_r\frac{\partial v_\phi}{\partial r} + \frac{v_r v_\phi}{r} + v_z\frac{\partial v_\phi}{\partial z} = \frac{v_r}{r}\frac{\partial(rv_\phi)}{\partial r} + \frac{v_z}{r}\frac{\partial(rv_\phi)}{\partial z} = \frac{1}{r}\mathbf{v}\cdot\nabla(rv_\phi)$$

and that the ϕ coordinate of the divergence of the viscous stress tensor, which is transpose symmetric, is

$$(\nabla\cdot\boldsymbol{\pi})_\phi = \frac{1}{r}\frac{\partial}{\partial r}(r\pi_{r\phi}) + \frac{\partial}{\partial z}(\pi_{z\phi}) + \frac{\pi_{r\phi}}{r} = \frac{1}{r^2}\frac{\partial}{\partial r}(r^2\pi_{r\phi}) + \frac{1}{r^2}\frac{\partial}{\partial z}(r^2\pi_{z\phi}) = \frac{1}{r}\nabla\cdot(r\pi_{r\phi}\hat{\mathbf{r}} + r\pi_{z\phi}\hat{\mathbf{z}})$$

The continuity equation for angular momentum density is then

$$\frac{\partial}{\partial t}(\rho v_\phi r) = m_i \dot{n} v_\phi r + \rho \dot{v}_\phi r$$
$$= -\left[m_i v_\phi r \nabla\cdot(n\mathbf{v}) + \rho\mathbf{v}\cdot\nabla(rv_\phi)\right] - \nabla\cdot(r\pi_{r\phi}\hat{\mathbf{r}} + r\pi_{z\phi}\hat{\mathbf{z}}) + \frac{1}{\mu_0}\mathbf{B}\cdot\nabla f \qquad (3.14)$$
$$= -\nabla\cdot\left(\rho v_\phi r\mathbf{v} + r\pi_{r\phi}\hat{\mathbf{r}} + r\pi_{z\phi}\hat{\mathbf{z}} - \frac{f}{\mu_0}\mathbf{B}\right)$$

Hence, the rate of change of total system angular momentum is

$$\dot{P}_\phi = \frac{\partial}{\partial t}\left(\int(\rho r v_\phi)\,dV\right) = -\int\left(\rho v_\phi r\mathbf{v} + r\pi_{r\phi}\hat{\mathbf{r}} + r\pi_{z\phi}\hat{\mathbf{z}} - \frac{f}{\mu_0}\mathbf{B}\right)\cdot d\boldsymbol{\Gamma}$$

With appropriate boundary conditions, total system angular momentum is conserved. One set of appropriate boundary conditions is as follows. The first term here vanishes with the boundary conditions for impermeable walls, $\mathbf{v}_\perp|_\Gamma = \mathbf{0}$. Referring to equation 3.17, it can be seen that with the boundary condition $(\nabla_\perp\omega)|_\Gamma = 0$, the second and third terms vanish too. Note that angular momentum conservation is not physical when there is friction between the fluids and the boundary wall. The boundary condition $(\nabla_\perp\omega)|_\Gamma = 0$ is physical only in unusual cases; for example, there may be no viscosity at the wall due to rotation of the wall. The last term is zero with the boundary condition $\left(\nabla_\|\psi\right)|_\Gamma = 0$ (*i.e.*, $\psi|_\Gamma = C$ (constant)), corresponding to having the magnetic field parallel to the boundary.

To prove energy conservation, we note that $-\mathbf{v}\cdot\nabla\mathbf{v} = -\nabla(v^2/2) + \mathbf{v}\times(\nabla\times\mathbf{v})$. Expressing the total system energy as the sum of kinetic, thermal and magnetic energy, the continuity equation for energy

density is

$$
\begin{aligned}
\dot{u}_{Total} &= \dot{u}_K + \dot{u}_{Th} + \dot{u}_M \\
&= \frac{\partial}{\partial t}\left(\frac{\rho \mathbf{v}^2}{2} + \frac{p}{\gamma - 1} + \frac{1}{2\mu_0 r^2}\left((\nabla\psi)^2 + f^2\right)\right) \\
&= \frac{m_i \dot{n}\mathbf{v}^2}{2} + \rho\mathbf{v}\cdot\dot{\mathbf{v}} + \frac{\dot{p}}{\gamma - 1} + \frac{1}{\mu_0 r^2}\left(\nabla\psi\cdot\left(\nabla\dot{\psi}\right) + f\dot{f}\right) \\
&= -\left[\frac{m_i \mathbf{v}^2}{2}\nabla\cdot(n\mathbf{v}) + \rho\mathbf{v}\cdot\nabla\frac{\mathbf{v}^2}{2}\right] \\
&\quad -\left[\mathbf{v}\cdot\nabla p + \frac{\mathbf{v}\cdot\nabla p + \gamma p\nabla\cdot\mathbf{v}}{\gamma - 1}\right] \\
&\quad -\left[\frac{1}{\mu_0 r^2}\Delta^*\psi(\mathbf{v}\cdot\nabla\psi) + \frac{1}{\mu_0 r^2}\nabla\psi\cdot\nabla(\mathbf{v}\cdot\nabla\psi)\right] \\
&\quad -\left[\frac{1}{\mu_0}\frac{f}{r^2}(\mathbf{v}\cdot\nabla f) + \frac{1}{\mu_0}f\nabla\cdot\left(\frac{f}{r^2}\mathbf{v}\right)\right] \\
&\quad +\left[\frac{1}{\mu_0}\omega\mathbf{B}\cdot\nabla f + \frac{1}{\mu_0}f\nabla\cdot\left(\omega\mathbf{B}\right)\right] \\
&\quad +\left[\frac{\eta(\Delta^*\psi)^2}{\mu_0 r^2} + \frac{1}{\mu_0 r^2}\nabla\psi\cdot\nabla(\eta\Delta^*\psi)\right] \\
&\quad +\left[\frac{\eta(\nabla f)^2}{\mu_0 r^2} + \frac{f}{\mu_0}\nabla\cdot\left(\frac{\eta}{r^2}\nabla f\right)\right] \\
&\quad -\left[\nabla\cdot(\mathbf{q}_i + \mathbf{q}_e)\right] \\
&\quad -\left[\mathbf{v}\cdot(\nabla\cdot\underline{\boldsymbol{\pi}}) + \underline{\boldsymbol{\pi}}:\nabla\mathbf{v}\right] \\
&= -\nabla\cdot\left(\frac{m_i n\mathbf{v}^2}{2}\mathbf{v} + \frac{\gamma p}{\gamma - 1}\mathbf{v} + \frac{(\mathbf{v}\cdot\nabla\psi)}{\mu_0 r^2}\nabla\psi\right. \\
&\quad \left. +\frac{f^2}{\mu_0 r^2}\mathbf{v} - \frac{1}{\mu_0}\omega f\,\mathbf{B} - \frac{\eta\Delta^*\psi}{\mu_0 r^2}\nabla\psi - \frac{\eta f}{\mu_0 r^2}\nabla f + \mathbf{q}_i + \mathbf{q}_e + \underline{\boldsymbol{\pi}}\cdot\mathbf{v}\right)
\end{aligned}
\tag{3.15}
$$

Note that the five magnetic terms involving μ_0 in the final full-divergence expression constitute the Poynting flux. Taking the integral over the final expression for $\dot{u}_{total}$ over the system volume, and applying Gauss's theorem, it can be seen how total system energy is conserved with appropriate boundary conditions, for example $\mathbf{v}|_\Gamma = \mathbf{0}$, $\mathbf{q}_{i\perp}|_\Gamma = \mathbf{q}_{e\perp}|_\Gamma = \mathbf{0}$, $(\nabla_\perp\psi)|_\Gamma = 0$ and $(\nabla_\perp f)|_\Gamma = 0$, or $\mathbf{v}_\perp|_\Gamma = \mathbf{0}$, $\mathbf{q}_{i\perp}|_\Gamma = \mathbf{q}_{e\perp}|_\Gamma = \mathbf{0}$, $(\nabla_\perp\psi)|_\Gamma = 0$ and $\left(B_{\theta\perp}v_\phi + \eta\left(\frac{\nabla_\perp f}{r}\right)\right)|_\Gamma = 0$. Referring to equation 3.13, note that either of these sets of boundary conditions also eliminate energy loss associated with Poynting flux. Note that the terms $+\frac{(\mathbf{v}\cdot\nabla\psi)}{\mu_0 r^2}\nabla\psi$ and $-\frac{\eta\Delta^*\psi}{\mu_0 r^2}\nabla\psi$ in the final full-divergence expression in equation 3.15 constitute the part of the Poynting flux that arises due to the toroidal component of the electric field at the boundary. The boundary condition $(\nabla_\perp\psi)|_\Gamma = 0$ or $(\Delta^*\psi)|_\Gamma = 0$ is required to eliminate this contribution. Referring to equation 3.10, it can be seen that the combination of boundary conditions $\mathbf{v}_\perp|_\Gamma = \mathbf{0}$ and $\psi|_\Gamma = 0$ automatically leads to the boundary condition $(\Delta^*\psi)|_\Gamma = 0$. Therefore, the boundary condition $(\nabla_\perp\psi)|_\Gamma = 0$ included above in the list of requirements for maintenance of system energy conservation may be replaced with the requirement $\psi|_\Gamma = 0$.

3.2 Discretised MHD model

In this section, the full set of discretised equations for a two-temperature MHD model is presented. The model has been constructed so as to preserve the global conservation laws inherent to the original continuous system of equations. In order to preserve the conservation laws of the system in discrete form, the pairs of terms which constitute full divergences, denoted with square brackets in equations 3.14 and 3.15, have been discretised in compatible way, *i.e.*, the appropriate corresponding discrete operators are used in these terms, and with particular boundary conditions, the operator properties lead to the cancellation of each pair. The discretisation may not be unique - several different schemes can be obtained with the same conservation properties. More details on the construction of the scheme are given in [11]. The resulting set of discretised equations is:

$$\dot{\overline{n}} = -\overline{\overline{\nabla}} \cdot (\overline{n}\ \mathbf{v}) + \widehat{\overline{\nabla}} \cdot \left(\widehat{\zeta} \left(\widehat{\overline{\nabla}}\ \overline{n} \right) \right)$$

$$\dot{\overline{v}}_r = \underbrace{-\overline{Dr} * \left(\frac{\overline{v}^2}{2} \right) - \overline{v}_z \left(\overline{Dz} * \overline{v}_r - \overline{Dr} * \overline{v}_z \right) + \overline{v}_\phi \left(\overline{Dr} * (\overline{r}\ \overline{v}_\phi) \right) / \overline{r}}_{-(\mathbf{v}\cdot\nabla\mathbf{v})_r = \left(-\nabla(v^2/2) + \mathbf{v}\times(\nabla\times\mathbf{v}) \right)_r} - \underbrace{\left(\overline{Dr} * \overline{p} \right) / \overline{\rho}}_{\frac{1}{\rho}(\nabla p)_r} - \underbrace{\overline{\Pi}_r / \overline{\rho}}_{\frac{1}{\rho}(\nabla\cdot\boldsymbol{\pi})_r}$$

$$+ \underbrace{\left(-(\overline{Dr} * \overline{\psi})\ (\overline{\Delta^*}\ \overline{\psi}) - \left(\overline{f}\ (\overline{Dr} * \overline{f}) \right) \right) / \left(\mu_0\ \overline{r}^2\ \overline{\rho} \right)}_{\frac{1}{\rho}(\mathbf{J}\times\mathbf{B})_r} + \overline{f}_{\zeta r} / \overline{\rho}$$

$$\dot{\overline{v}}_\phi = \underbrace{-\overline{\mathbf{v}} \cdot \left(\overline{\overline{\nabla}}\ (\overline{r}\ \overline{v}_\phi) \right) / \overline{r}}_{-(\mathbf{v}\cdot\nabla\mathbf{v})_\phi = \left(-\nabla(v^2/2) + \mathbf{v}\times(\nabla\times\mathbf{v}) \right)_\phi} - \underbrace{\overline{\Pi}_\phi / \overline{\rho}}_{\frac{1}{\rho}(\nabla\cdot\boldsymbol{\pi})_\phi} + \underbrace{\left(\widehat{W} * \left(\widehat{\mathbf{B}}_\theta \cdot \left(\widehat{\overline{\nabla}}\ \overline{f} \right) \right) \right) / (\mu_0\ \overline{r}\ \overline{\rho})}_{\frac{1}{\rho}(\mathbf{J}\times\mathbf{B})_\phi} + \overline{f}_{\zeta\phi} / \overline{\rho}$$

$$\dot{\overline{v}}_z = \underbrace{-\overline{Dz} * \left(\frac{\overline{v}^2}{2} \right) + \overline{v}_r \left(\overline{Dz} * \overline{v}_r - \overline{Dr} * \overline{v}_z \right) + \overline{v}_\phi \left(\overline{Dz} * (\overline{r}\ \overline{v}_\phi) \right) / \overline{r}}_{-(\mathbf{v}\cdot\nabla\mathbf{v})_z = \left(-\nabla(v^2/2) + \mathbf{v}\times(\nabla\times\mathbf{v}) \right)_z} - \underbrace{\left(\overline{Dz} * \overline{p} \right) / \overline{\rho}}_{\frac{1}{\rho}(\nabla p)_z} - \underbrace{\overline{\Pi}_z / \overline{\rho}}_{\frac{1}{\rho}(\nabla\cdot\boldsymbol{\pi})_z}$$

$$+ \underbrace{\left(- \left(\overline{Dz} * \overline{\psi} \right)\ \left(\overline{\Delta^*}\ \overline{\psi} \right) - \overline{f}\ \left(\overline{Dz} * \overline{f} \right) \right) / \left(\mu_0\ \overline{r}^2\ \overline{\rho} \right)}_{\frac{1}{\rho}(\mathbf{J}\times\mathbf{B})_z} + \overline{f}_{\zeta z} / \overline{\rho}$$

$$\dot{\overline{p}}_i = -\overline{\mathbf{v}} \cdot \left(\overline{\overline{\nabla}}\ \overline{p}_i \right) - \gamma\,\overline{p}_i\ \left(\overline{\overline{\nabla}} \cdot \mathbf{v} \right) + (\gamma - 1) \left[-\widehat{\overline{\nabla}} \cdot \widehat{\mathbf{q}}_i + \overline{Q}_{ie} + \underbrace{\overline{Q}_\pi}_{-\boldsymbol{\pi}:\nabla\mathbf{v}} + \overline{Q}_\zeta \right]$$

$$\dot{\overline{p}}_e = -\overline{\mathbf{v}} \cdot \left(\overline{\overline{\nabla}}\ \overline{p}_e \right) - \gamma\,\overline{p}_e\ \left(\overline{\overline{\nabla}} \cdot \mathbf{v} \right) + (\gamma - 1) \left[-\widehat{\overline{\nabla}} \cdot \widehat{\mathbf{q}}_e - \overline{Q}_{ie} \right.$$

$$\left. + \underbrace{(\overline{\eta}/\mu_0)\ \left((\overline{\Delta^*}\ \overline{\psi}) / \overline{r} \right)^2}_{\eta' J_\phi^2} + \underbrace{\widehat{W} * \left((\widehat{\eta}/\mu_0)\ \left(\left(\widehat{\overline{\nabla}}\ \overline{f} \right) / \widehat{r} \right)^2 \right)}_{\eta' J_\theta^2} \right]$$

$$\dot{\overline{\psi}} = -\overline{\mathbf{v}} \cdot \left(\overline{\overline{\nabla}}\ \overline{\psi} \right) + \overline{\eta}\ \left(\overline{\Delta^*}\ \overline{\psi} \right)$$

$$\dot{\overline{f}} = \underline{r}^2 \left[-\overline{\overline{\nabla}} \cdot \left(\overline{f}\ \overline{\mathbf{v}} / \overline{r}^2 \right) + \widehat{\overline{\nabla}} \cdot \left(\widehat{\mathbf{B}}_\theta\ \widehat{\omega} \right) + \widehat{\overline{\nabla}} \cdot \left(\widehat{\eta}\ \left(\widehat{\overline{\nabla}}\ \overline{f} \right) / \widehat{r}^2 \right) \right] \tag{3.16}$$

Here, $\widehat{\eta} = <\overline{\eta}>^e$, and $\widehat{\omega} = <\overline{v}_\phi / \overline{r}>^e$ (equation 2.7). $\widehat{W}$ is the volume-averaging operator (equation 2.8), and $\widehat{\mathbf{B}}_\theta = \left(- \left(\widehat{Dz} * \overline{\psi} \right) \widehat{\mathbf{r}} + \left(\widehat{Dr} * \overline{\psi} \right) \widehat{\mathbf{z}} \right) / \widehat{r}$. These discretised equations are written in a form which is a direct analogue of their continuous representations with inclusion of several extra terms. Namely, the continuity equation has an artificial density diffusion term, which is required for density smoothing and

15

avoiding negative density regions. The density diffusion coefficient $\zeta\,[\mathrm{m^2/s}]$ can be spatially held constant or can be increased where density gradients are high or density values approach zero. The components of force per volume vector $\bar{\mathbf{f}}_\zeta = (\bar{f}_{\zeta r}, \bar{f}_{\zeta\phi}, \bar{f}_{\zeta z})^T$ in the velocity equations and the heating term $\overline{Q}_\zeta$ in the ion pressure equation are included to cancel the effect of artificial density diffusion on the total system momentum and energy. The expressions for these terms will be defined in section D.

To close the system of equations, we need to specify the forms of the viscous terms $\overline{\boldsymbol{\Pi}}$ and $\overline{Q}_\pi$, the species heat exchange term $\overline{Q}_{ie}$, the resistive diffusion coefficient $\overline{\eta}$, and the heat flux density terms $\hat{\mathbf{q}}_i$ and $\hat{\mathbf{q}}_e$. For the viscous terms, we use, for simplicity, the unmagnetised version of the viscous stress tensor in axisymmetric cylindrical coordinates, which is given as [18]:

$$\underline{\boldsymbol{\pi}} = -\mu \begin{pmatrix} 2\frac{\partial v_r}{\partial r} - \frac{2}{3}\nabla\cdot\mathbf{v} & r\frac{\partial}{\partial r}\left(\frac{v_\phi}{r}\right) & \frac{\partial v_z}{\partial r} + \frac{\partial v_r}{\partial z} \\ r\frac{\partial}{\partial r}\left(\frac{v_\phi}{r}\right) & 2\frac{v_r}{r} - \frac{2}{3}\nabla\cdot\mathbf{v} & \frac{\partial v_\phi}{\partial z} \\ \frac{\partial v_z}{\partial r} + \frac{\partial v_r}{\partial z} & \frac{\partial v_\phi}{\partial z} & 2\frac{\partial v_z}{\partial z} - \frac{2}{3}\nabla\cdot\mathbf{v} \end{pmatrix} \tag{3.17}$$

where $\mu\,[\mathrm{kg\,m^{-1}s^{-1}}]$ is dynamic viscosity. The components of $\overline{\boldsymbol{\Pi}}$ represent the discrete forms of the components of $\nabla\cdot\underline{\boldsymbol{\pi}}$, and are defined as

$$\overline{\Pi}_r = \left[-2\widehat{\overline{Dr}} * \left(\hat{\mu}\,\hat{r}\,\left(\overline{Dr}*\overline{v}_r\right)\right) - \widehat{\overline{Dz}}*\left(\hat{\mu}\,\hat{r}\,\left(\overline{Dr}*\overline{v}_z + \overline{Dz}*\overline{v}_r\right)\right)\right]/\overline{r}$$

$$+\frac{2}{3}\left(\widehat{\overline{Dr}}*\left(\hat{\mu}\,\left(\widehat{\overline{\nabla}}\cdot\mathbf{v}\right)\right)\right) +2\,\overline{\mu}\,\overline{v}_r\,/\,\overline{r}^2$$

$$\overline{\Pi}_\phi = -\left(\widehat{\overline{\nabla}}\cdot\left(\hat{\mu}\,\hat{r}^2\,\left(\widehat{\overline{\nabla}}\,\varpi\right)\right)\right)/\overline{r}$$

$$\overline{\Pi}_z = \left[-2\widehat{\overline{Dz}} * \left(\hat{\mu}\,\hat{r}\,\left(\overline{Dz}*\overline{v}_z\right)\right) - \widehat{\overline{Dr}}*\left(\hat{\mu}\,\hat{r}\,\left(\overline{Dr}*\overline{v}_z + \overline{Dz}*\overline{v}_r\right)\right)\right]/\overline{r}$$

$$+\frac{2}{3}\left(\widehat{\overline{Dz}}*\left(\hat{\mu}\,\left(\widehat{\overline{\nabla}}\cdot\mathbf{v}\right)\right)\right) \tag{3.18}$$

Here, $\hat{\mu} = <\overline{\mu}>^e$ (equation 2.7). The contraction (inner product) of two second order tensors is defined as $\underline{\boldsymbol{T}}:\underline{\boldsymbol{U}} = \sum_i\sum_j T_{ij}U_{ij}$, and $\nabla\mathbf{v}$, in cylindrical coordinates with azimuthal symmetry, is

$$\nabla\mathbf{v} = \begin{pmatrix} \frac{\partial v_r}{\partial r} & -\frac{v_\phi}{r} & \frac{\partial v_r}{\partial z} \\ \frac{\partial v_\phi}{\partial r} & \frac{v_r}{r} & \frac{\partial v_\phi}{\partial z} \\ \frac{\partial v_z}{\partial r} & 0 & \frac{\partial v_z}{\partial z} \end{pmatrix}$$

In the expression for $\dot{\bar{p}}_i$, $\overline{Q}_\pi$ is the discrete form of $-\underline{\boldsymbol{\pi}}:\nabla\mathbf{v}$:

$$\overline{Q}_\pi = \widehat{\overline{W}} * \left[\hat{\mu}\left\{2\left(\overline{Dr}*\overline{v}_r\right)^2 + 2\left(\overline{Dz}*\overline{v}_z\right)^2 + \left(\hat{r}\,\left(\widehat{\overline{\nabla}}\,\varpi\right)\right)^2\right.\right.$$

$$\left.\left. + \left(\overline{Dr}*\overline{v}_z + \overline{Dz}*\overline{v}_r\right)^2 - \frac{2}{3}\left(\widehat{\overline{\nabla}}\cdot\mathbf{v}\right)^2\right\}\right] + 2\,\overline{\mu}\,\left(\overline{v}_r\,/\,\overline{r}\right)^2 \tag{3.19}$$

The representations in equations 3.18 and 3.19 are consistent with the discrete form of energy conservation, as will be shown in section 3.3.4. $\hat{\mu}\,[\mathrm{kg\,m^{-1}s^{-1}}] = \hat{\rho}\,\hat{\nu}$ specifies dynamic viscosity at element centroids, where $\hat{\nu}\,[\mathrm{m^2/s}]$ specifies kinematic viscosity. A certain minimum level of artificial viscosity, which depends on the time-step, simulation type, and mesh resolution, is required for numerical stability. Simulations presented in this work, which involve CT formation and consequent extreme plasma acceleration and steep gradients

in the velocity fields, are run with dynamic viscosity set to constant $\mu = \rho_0 \nu_0$, for typical code input $\nu_0 \sim 700 [\text{m}^2/\text{s}]$, where $\rho_0 \sim 6 \times 10^{-6} [\text{kg}/\text{m}^3]$ is a typical representative mass density.

The resistive diffusion coefficient is based on the Spitzer formula

$$\bar{\eta} = \frac{m_e}{1.96\, e^2\, \mu_0} \,/\, (Z\, \bar{n}\, \bar{\tau}_{ei}) = \left(418\, Z \left(\bar{T}_e\, [\text{eV}] \right)^{-\frac{3}{2}} \right) [\text{m}^2/\text{s}]$$

where the electron-ion collision time is

$$\bar{\tau}_{ei} = \left(\frac{6\sqrt{2}\pi^{1.5}\epsilon_0^2 \sqrt{m_e}}{\Lambda\, e^4 Z^2} \right) \left(\bar{T}_e\, [\text{J}] \right)^{\frac{3}{2}} /\, \bar{n} = \left(3.45 \times 10^{10} \frac{\left(\bar{T}_e\, [\text{eV}] \right)^{\frac{3}{2}} /\, \bar{n}\, [\text{m}^{-3}]}{Z^2} \right) [\text{s}]$$

Here, $\Lambda = 10$ is the Coulomb logarithm. In general, to limit the timestep to acceptably high values, simulations are run with an upper limit on η of around $5000 [\text{m}^2/\text{s}]$.

The heat exchange term $\overline{Q}_{ie}$ gives the rate at which energy is imparted from the electrons to the ions due to collisions between ion and electron fluids:

$$\overline{Q}_{ie} = 3(m_e/m_i)\, Z\, \bar{n} \left(\bar{T}_e[\text{J}] - \bar{T}_i[\text{J}] \right) /\, \bar{\tau}_{ei}$$
$$= \left(7.6 \times 10^{-33} Z^3 \left(\bar{T}_e[\text{eV}] - \bar{T}_i[\text{eV}] \right) \left(\bar{T}_e\, [\text{eV}] \right)^{-\frac{3}{2}} \left(\bar{n}\, [\text{m}^{-3}] \right)^2 /\mu_i \right) [\text{W}/\text{m}^3]$$

Here, μ_i is the ion mass in units of proton mass.

To include the effect of significantly enhanced thermal diffusion parallel to the magnetic field, we include anisotropy in the model for thermal diffusion. The species heat flux density can be expressed as

$$\mathbf{q}_\alpha = - \left(\kappa_{\|\alpha} \nabla_\| T_\alpha + \kappa_{\perp\alpha} \nabla_\perp T_\alpha \right)$$
$$= - \left(\left(\kappa_{\|\alpha} - \kappa_{\perp\alpha} \right) \nabla_\| T_\alpha + \kappa_{\perp\alpha} \nabla T_\alpha \right)$$

where $\kappa_{\|\alpha}$ and $\kappa_{\perp\alpha}$ $[(\text{m-s})^{-1}]$ are the thermal conductivities for species α, pertaining to thermal diffusion parallel and perpendicular to the magnetic field. With azimuthal symmetry, the toroidal component of $\nabla_\| T_\alpha$ can be dropped as it will not make a finite contribution to $\nabla \cdot \mathbf{q}_\alpha$, so that the discrete forms of $\mathbf{q}_\alpha$ may be expressed as

$$\hat{\mathbf{q}}_\alpha = - \left\{ \left(\hat{\kappa}_{\|\alpha} - \hat{\kappa}_{\perp\alpha} \right) \left(\hat{\mathbf{B}}_\theta \left(\hat{\mathbf{B}}_\theta \cdot \left(\hat{\overline{\overline{\nabla}}}\, \overline{T}_\alpha \right) \right) /\, \hat{B}^2 \right) + \hat{\kappa}_{\perp\alpha} \left(\hat{\overline{\overline{\nabla}}}\, \overline{T}_\alpha \right) \right\} \tag{3.20}$$

Physically, the thermal conductivities vary with local conditions. The simulations presented in this work were run with constant conductivities, of the order $\kappa_{\|\alpha} = n_0 \chi_{\|\alpha}$ and $\kappa_{\perp\alpha} = n_0 \chi_{\perp\alpha}$, where $n_0\, [\text{m}^{-3}]$ is a typical representative number density, and the thermal diffusion coefficients $\chi_{\|\alpha}$, $\chi_{\perp\alpha}$ $[\text{m}^2/\text{s}]$ are held constant.

The code uses explicit time-stepping, with options of forward Euler, Runge-Kutta 2 or Runge-Kutta 4 schemes. Although extremely low or high diffusion coefficient values can be used while maintaining numerical stability if the timestep is reduced, lower and upper limits need to be imposed on diffusion coefficients in order to achieve numerical stability in combination with acceptably short simulation runtimes. This is consistent with the standard stability criteria [19] that timestep is limited by the constraints $dt \lesssim D_{min}/v_{max}^2$ and $dt \lesssim h_e^2/D_{max}$, where D_{min} and $D_{max} [\text{m}^2/\text{s}]$ are the minimum and maximum diffusion coefficients, and v_{max} is the maximum speed associated with the system.

3.3 Conservation properties (discrete form of equations)

Here, we demonstrate that the discretised system of equations 3.16 has the same global conservation laws as the original continuous system.

3.3.1 Particle count conservation

Integrating the discrete form of the continuity equation 3.16 over volume, we obtain the rate of change of the total number of particles in the system:

$$\dot{N} = \overline{dV}^T * \dot{\overline{n}}$$
$$= \overline{dV}^T * \left\{ -\overline{\overline{\nabla}} \cdot (\overline{n}\,\mathbf{v}) + \widehat{\overline{\nabla}} \cdot \left(\widehat{\zeta} \left(\overline{\overline{\nabla}}\,\overline{n} \right) \right) \right\}$$

With boundary conditions $\overline{\mathbf{v}}_\perp|_\Gamma = \mathbf{0}$, or $\overline{\mathbf{v}}|_\Gamma = \mathbf{0}$, identity C.9 determines that the first term is zero. The second term is always zero, due to property 2.20. Hence, total particle count is conserved. Note that if no boundary conditions are explicitly applied to density, $\overline{n}$ will automatically evolve to satisfy the natural boundary condition $(\zeta\,\nabla_\perp n)\,|_\Gamma = 0$, as a consequence of the properties of the element-to-node divergence operation (section 2.5).

3.3.2 Toroidal flux conservation

Analogous to equation 3.12, the discrete expression for the rate of change of system toroidal flux follows from the discrete expression for $\dot{\overline{f}}$ in equation 3.16

$$\dot{\Phi} = \frac{1}{2\pi} \overline{dV}^T * \left\{ \dot{\overline{f}} / \overline{r}^2 \right\}$$
$$= \frac{1}{2\pi} \overline{dV}^T * \left\{ -\overline{\overline{\nabla}} \cdot \left(\overline{f}\,\overline{\mathbf{v}} / \overline{r}^2 \right) + \widehat{\overline{\nabla}} \cdot \left(\widehat{\mathbf{B}}_\theta\,\widehat{\omega} \right) + \widehat{\overline{\nabla}} \cdot \left(\widehat{\eta} \left(\overline{\overline{\nabla}}\,\overline{f} \right) / \widehat{r}^2 \right) \right\}$$

Once again, with boundary conditions $\overline{\mathbf{v}}_\perp|_\Gamma = \mathbf{0}$, identity C.9 determines that the first term is zero. The second and third terms are zero, due to property 2.20. Hence, system toroidal flux is conserved. Note that in this case $\overline{f}$ will automatically evolve to satisfy the natural boundary condition $(\mathbf{B}_{\theta\perp}\omega + \eta\,(\nabla_\perp f)\,/r^2)\,|_\Gamma = 0$ if no boundary conditions are explicitly imposed on $\overline{f}$. In combination with the boundary condition $\overline{\mathbf{v}}_\perp|_\Gamma = \mathbf{0}$, this corresponds to having the poloidal component of the electric field perpendicular to the boundary, the condition, in the case of azimuthal symmetry, for a perfectly electrically conducting boundary (see equation 3.13).

   Simulations that include CT formation and compression are run with the boundary conditions $\overline{v}_\beta|_\Gamma = 0$ applied explicitly to each velocity component, so that the automatically imposed boundary condition for f, corresponding to the physical case of a perfectly electrically conducting boundary, becomes $(\nabla_\perp f)\,|_\Gamma = 0$.

   As described in section 5.4, when part of the computational boundary is modelled as an electrical insulator, special care must be taken to define the explicitly applied boundary condition for f along the insulator boundary, in order to maintain global toroidal flux conservation. In such cases, only the conducting boundary regions are allowed to retain the naturally imposed boundary conditions for f.

3.3.3 Angular momentum conservation

The rate of change of system angular momentum is $\dot{P}_\phi = \frac{\partial}{\partial t}\left(\int (\rho r v_\phi)\,dV \right) = m_i \int (r v_\phi \dot{n} + n r \dot{v}_\phi)\,dV$. Here, it will be shown that system angular momentum is conserved for the discrete model when the terms corresponding to density diffusion in the discrete expressions for $\dot{n}$ and $\dot{v}_\phi$ are neglected. In section D, it

will be shown that angular momentum conservation can be maintained even with the inclusion of these terms. In discrete form, the rate of change of angular momentum is

$$\dot{P}_\phi = m_i \overline{dV}^T * \left\{ -(\overline{r}\,\overline{v}_\phi)\ \left(\overline{\overline{\nabla}} \cdot (\overline{n}\,\mathbf{v})\right) + (\overline{n}\,\overline{r})\ \left\{ -\mathbf{v} \cdot \left(\overline{\overline{\nabla}}\,(\overline{r}\,\overline{v}_\phi)\right) / \overline{r} - \overline{\overline{\Pi}}_\phi / \overline{\rho} + \widehat{\overline{W}} * \left(\widehat{\mathbf{B}}_\theta \cdot \left(\widehat{\overline{\nabla}}\,\overline{f}\right)\right) / (\mu_0\,\overline{r}\,\overline{\rho}) \right\} \right\} \quad (3.21)$$

The first two terms here can be simplified to $-m_i \overline{dV}^T * \left\{ (\overline{r}\,\overline{v}_\phi)\ \left(\overline{\overline{\nabla}} \cdot (\overline{n}\,\mathbf{v})\right) + (\overline{n}\,\mathbf{v}) \cdot \left(\overline{\overline{\nabla}}\,(\overline{r}\,\overline{v}_\phi)\right) \right\}$. With boundary conditions $\overline{\mathbf{v}}_\perp|_\Gamma = \mathbf{0}$, this combination vanishes due to identity C.8. With reference to the definition for $\overline{\overline{\Pi}}_\phi$ (equation 3.18), if no boundary conditions are explicitly applied to $\overline{v}_\phi$, the properties of the element-to-node divergence operation will automatically impose the natural boundary conditions $(\nabla_\perp \omega)|_\Gamma = 0$, and the third term in equation 3.21 will vanish due to identity 2.20. With reference to equation 2.11, the fourth term in equation 3.21 can be expressed as

$$\frac{1}{\mu_0} \widehat{dV}^T * \left\{ \widehat{\mathbf{B}}_\theta \cdot \left(\widehat{\overline{\nabla}}\,\overline{f}\right) \right\}$$

$$= \frac{2\pi}{\mu_0} (\widehat{s}\,\widehat{r})^T * \left\{ \left(-\left(\overline{\widehat{Dz}} * \overline{\psi}\right)\ \left(\overline{\widehat{Dr}} * \overline{f}\right) + \left(\overline{\widehat{Dr}} * \overline{\psi}\right)\ \left(\overline{\widehat{Dz}} * \overline{f}\right) \right) / \widehat{r} \right\}$$

$$= \frac{2\pi}{\mu_0} \widehat{s}^T * \left\{ -\left(\overline{\widehat{Dz}} * \overline{\psi}\right)\ \left(\overline{\widehat{Dr}} * \overline{f}\right) + \left(\overline{\widehat{Dr}} * \overline{\psi}\right)\ \left(\overline{\widehat{Dz}} * \overline{f}\right) \right\}$$

$$= \frac{2\pi}{\mu_0} \left(-\left(\overline{\widehat{Dr}} * \overline{f}\right)^T * \left(\widehat{S} * \left(\overline{\widehat{Dz}} * \overline{\psi}\right)\right) + \left(\overline{\widehat{Dz}} * \overline{f}\right)^T * \left(\widehat{S} * \left(\overline{\widehat{Dr}} * \overline{\psi}\right)\right) \right)$$

$$\frac{2\pi}{\mu_0} \overline{f}^T * \left(\left(-\overline{\widehat{Dr}}^T * \widehat{S} * \overline{\widehat{Dz}} + \overline{\widehat{Dz}}^T * \widehat{S} * \overline{\widehat{Dr}} \right) * \overline{\psi} \right)$$

and vanishes due to identity B.4, when the boundary condition $\psi|_\Gamma = 0$ is applied. Thus for angular momentum conservation, no boundary conditions are applied on v_ϕ, and $\psi|_\Gamma$ must be set to zero.
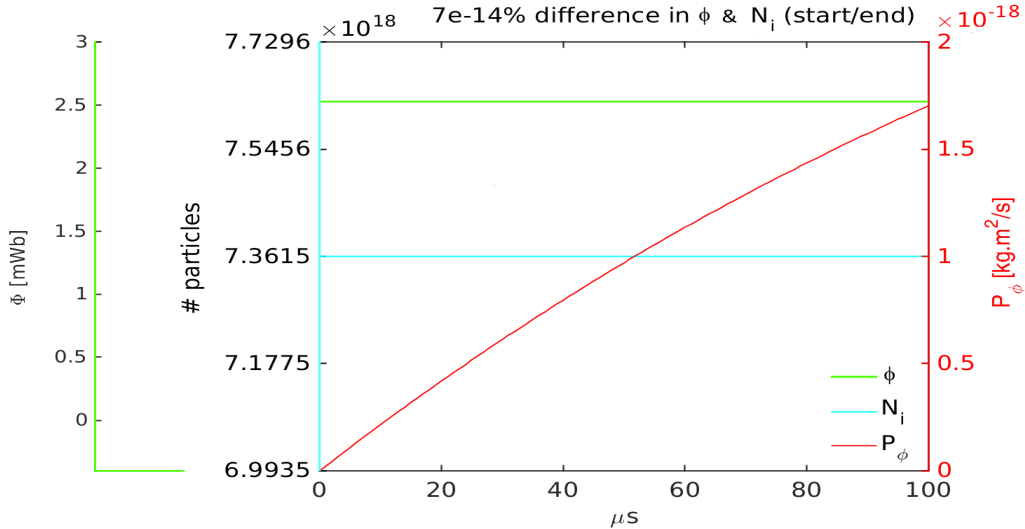

Figure 6: Illustration of particle, toroidal flux, and angular momentum conservation

As shown in figure 6, the total number of particles (*i.e.*, # ions, N_i), toroidal flux, and angular momentum, calculated as the integrals over the computational domain, is conserved to numerical precision for a 100µs simulation that started from a Grad-Shafranov equilibrium, with explicitly applied boundary conditions $v_r|_\Gamma = v_z|_\Gamma = 0$, and $\psi|_\Gamma = 0$. As mentioned in section 3.1.1, angular momentum is not physical when there is friction between the fluids and the boundary wall. The boundary condition $(\nabla_\perp \omega)|_\Gamma = 0$ is physical only in unusual cases; for example, there may be no viscosity at the wall due to rotation of the wall. Angular momentum is not conserved in the simulations of CT formation and magnetic compression that will be presented in section 6, because in those simulations, all velocity components are set to zero at the boundary.

19

3.3.4   Energy conservation

Analogous to the continuous expression 3.15, the discrete expression for total system energy is

$$
\begin{aligned}
\dot{U}_{Total} &= \dot{U}_K + \dot{U}_{Th} + \dot{U}_M \\[4pt]
&= \frac{\partial}{\partial t}\left(\overline{dV}^T * \left\{\frac{\overline{\rho}\,\overline{\mathbf{v}}^2}{2} + \frac{\overline{p}}{\gamma-1} + \frac{1}{2\mu_0}\overline{f}^2/\overline{r}^2\right\} + \widehat{dV}^T * \left\{\frac{1}{2\mu_0}\left(\widehat{\overline{\nabla}}\,\overline{\psi}\right)^2/\hat{r}^2\right\}\right) \\[4pt]
&= \overline{dV}^T * \left\{\frac{m_i\,\dot{\overline{n}}\,\overline{\mathbf{v}}^2}{2} + \overline{\rho}\,\overline{\mathbf{v}}\cdot\dot{\overline{\mathbf{v}}} + \frac{\dot{\overline{p}}}{\gamma-1} + \frac{1}{\mu_0}\overline{f}\,\dot{\overline{f}}/\overline{r}^2\right\} + \widehat{dV}^T * \left\{\frac{1}{\mu_0}\left(\widehat{\overline{\nabla}}\,\overline{\psi}\right)\cdot\left(\widehat{\overline{\nabla}}\,\dot{\overline{\psi}}\right)/\hat{r}^2\right\} \\[4pt]
&= -\left[\overline{dV}^T * \left\{\frac{1}{2}\overline{v}^2\left(\overline{\overline{\nabla}}\cdot(\overline{\rho}\,\overline{\mathbf{v}})\right) + \frac{1}{2}(\overline{\rho}\,\overline{\mathbf{v}})\cdot\left(\overline{\overline{\nabla}}\,\overline{v}^2\right)\right\}\right] \\[4pt]
&\quad -\left[\overline{dV}^T * \left\{\overline{\mathbf{v}}\cdot\left(\overline{\overline{\nabla}}\,\overline{p}\right) + \frac{1}{\gamma-1}\left(\overline{\mathbf{v}}\cdot\left(\overline{\overline{\nabla}}\,\overline{p}\right) + \gamma\,\overline{p}\left(\overline{\overline{\nabla}}\cdot\overline{\mathbf{v}}\right)\right)\right\}\right] \\[4pt]
&\quad -\left[\frac{1}{\mu_0}\overline{dV}^T * \left\{\left(\overline{\mathbf{v}}\cdot\left(\overline{\overline{\nabla}}\,\overline{\psi}\right)\right)\left(\overline{\overline{\Delta^*}}\,\overline{\psi}\right)/\overline{r}^2\right\} + \widehat{dV}^T * \left\{\left(\widehat{\overline{\nabla}}\,\overline{\psi}\right)\cdot\left(\widehat{\overline{\nabla}}\left(\overline{\mathbf{v}}\cdot\left(\overline{\overline{\nabla}}\,\overline{\psi}\right)\right)\right)/\hat{r}^2\right\}\right] \\[4pt]
&\quad -\left[\frac{1}{\mu_0}\overline{dV}^T * \left\{\left(\overline{f}\,\overline{\mathbf{v}}/\overline{r}^2\right)\cdot\left(\overline{\overline{\nabla}}\,\overline{f}\right) + \overline{f}\left(\overline{\overline{\nabla}}\cdot\left(\overline{f}\,\overline{\mathbf{v}}/\overline{r}^2\right)\right)\right\}\right] \\[4pt]
&\quad +\left[\frac{1}{\mu_0}\overline{dV}^T * \left\{\overline{\omega}\left(\widehat{\overline{W}} * \left(\hat{\mathbf{B}}_\theta\cdot\left(\widehat{\overline{\nabla}}\,\overline{f}\right)\right)\right) + \overline{f}\left(\widehat{\overline{\nabla}}\cdot\left(\hat{\mathbf{B}}_\theta\,\hat{\omega}\right)\right)\right\}\right] \\[4pt]
&\quad +\left[\frac{1}{\mu_0}\overline{dV}^T * \left\{\overline{\eta}\left(\left(\overline{\overline{\Delta^*}}\,\overline{\psi}\right)/\overline{r}\right)^2\right\} + \widehat{dV}^T * \left\{\left(\widehat{\overline{\nabla}}\,\overline{\psi}\right)\cdot\left(\widehat{\overline{\nabla}}\left(\overline{\eta}\left(\overline{\overline{\Delta^*}}\,\overline{\psi}\right)\right)\right)/\hat{r}^2\right\}\right] \\[4pt]
&\quad +\left[\frac{1}{\mu_0}\overline{dV}^T * \left\{\widehat{\overline{W}} * \left(\left(\hat{\eta}\left(\widehat{\overline{\nabla}}\,\overline{f}\right)/\hat{r}^2\right)\cdot\left(\widehat{\overline{\nabla}}\,\overline{f}\right)\right) + \overline{f}\left(\widehat{\overline{\nabla}}\cdot\left(\hat{\eta}\left(\widehat{\overline{\nabla}}\,\overline{f}\right)/\hat{r}^2\right)\right)\right\}\right] \\[4pt]
&\quad -\left[\overline{dV}^T * \left\{\widehat{\overline{\nabla}}\cdot(\hat{\mathbf{q}}_i + \hat{\mathbf{q}}_e)\right\}\right] \\[4pt]
&\quad -\left[\overline{dV}^T * \left\{\overline{\mathbf{v}}\cdot\overline{\boldsymbol{\Pi}} - \overline{Q}_\pi\right\}\right]
\end{aligned}
\tag{3.22}
$$

Note that each set of square brackets has a counterpart in equation 3.15, the continuous form of $\dot{u}_{Total}$. The poloidal magnetic energy is expressed in terms of the element-centered gradient of $\overline{\psi}$, as required for consistency with the definition of the second order $\overline{\overline{\Delta^*}}$ differential operator. Here, it will be shown how, using the various mimetic properties of the differential operators, that the terms in each set of square brackets cancel when appropriate boundary conditions are applied, leading to total system energy conservation.

The terms in the first set of square brackets here represents the contribution to $\dot{U}_K$ due to advection, and vanish, with boundary conditions $\mathbf{v}_\perp|_\Gamma = \mathbf{0}$, due to equation C.8 (where $\overline{\mathbf{P}} = \overline{\rho}\,\overline{\mathbf{v}}$ and $\overline{U} = \overline{v}^2$). The terms in the second of square brackets represents the contribution to $\dot{U}_{Th}$ from compressional heating and, with the same boundary conditions, also vanish due to equation C.8 (with $\overline{\mathbf{P}} = \overline{\mathbf{v}}$ and $\overline{U} = \overline{p}$).

The terms in the third, fourth and fifth sets of square brackets in equation 3.22 represent the contribution to $\dot{U}_K$ that arises from the discrete forms of the components of $(\mathbf{J}\times\mathbf{B})$ in combination with the ideal (non-resistive) part of $\dot{U}_M$. Using identity 2.23 to expand the $\overline{\overline{\Delta^*}}$ operator, the terms in the third set of square brackets can be expressed as

$$
-\frac{1}{\mu_0}\left[\overline{dV}^T * \left\{\left(\overline{\mathbf{v}}\cdot\left(\overline{\overline{\nabla}}\,\overline{\psi}\right)\right)\left(\widehat{\overline{\nabla}}\cdot\left(\left(\widehat{\overline{\nabla}}\,\overline{\psi}\right)/\hat{r}^2\right)\right)\right\} + \widehat{dV}^T * \left\{\left(\left(\widehat{\overline{\nabla}}\,\overline{\psi}\right)/\hat{r}^2\right)\cdot\left(\widehat{\overline{\nabla}}\left(\overline{\mathbf{v}}\cdot\left(\overline{\overline{\nabla}}\,\overline{\psi}\right)\right)\right)\right\}\right]
$$

These terms cancel due to identity 2.18, where $\hat{\mathbf{P}} = \left(\left(\widehat{\overline{\nabla}}\,\overline{\psi}\right)/\hat{r}^2\right)$ and $\overline{U} = \overline{\mathbf{v}}\cdot\left(\overline{\overline{\nabla}}\,\overline{\psi}\right)$.

With boundary condition $\mathbf{v}\perp|_\Gamma = \mathbf{0}$, the terms in the fourth set of square brackets cancel due to identity C.8. Using equation 2.9, where $\overline{Q} = \overline{\omega} = \overline{v}_\phi/\overline{r}$, the terms in the fifth set of square brackets can be expressed as

$$\frac{1}{\mu_0}\left[\widehat{dV}^T * \left\{\left(\widehat{\mathbf{B}}_\theta\,\widehat{\omega}\right)\cdot\left(\overline{\widehat{\nabla}}\,\overline{f}\right)\right\} + \overline{dV}^T * \left\{\overline{f}\,\left(\widehat{\nabla}\cdot\left(\widehat{\mathbf{B}}_\theta\,\widehat{\omega}\right)\right)\right\}\right]$$

This combination cancels due to identity 2.18, where $\widehat{\mathbf{P}} = \left(\widehat{\mathbf{B}}_\theta\,\widehat{\omega}\right)$ and $\overline{U} = \overline{f}$.

The terms in the sixth set of square brackets represent the rate of increase of thermal energy due to ohmic heating from toroidal currents (first term), in combination with the rate of decrease of magnetic energy associated with poloidal field, due to resistive decay of the toroidal currents (second term). As is true in the continuous case, these terms are balanced in the discrete case. Using identity 2.23, the combination may be expressed as

$$\frac{1}{\mu_0}\left[\overline{dV}^T * \left\{\left(\overline{\eta}\,\left(\overline{\overline{\Delta}^*}\,\overline{\psi}\right)\right)\,\left(\widehat{\nabla}\cdot\left(\left(\overline{\widehat{\nabla}}\,\overline{\psi}\right)/\widehat{r}^2\right)\right)\right\} + \widehat{dV}^T * \left\{\left(\left(\overline{\widehat{\nabla}}\,\overline{\psi}\right)/\widehat{r}^2\right)\cdot\left(\overline{\widehat{\nabla}}\,\left(\overline{\eta}\,\left(\overline{\overline{\Delta}^*}\,\overline{\psi}\right)\right)\right)\right\}\right]$$

and vanishes due to identity 2.18, where $\widehat{\mathbf{P}} = \left(\left(\overline{\widehat{\nabla}}\,\overline{\psi}\right)/\widehat{r}^2\right)$ and $\overline{U} = \overline{\eta}\,\left(\overline{\overline{\Delta}^*}\,\overline{\psi}\right)$.

The terms in the seventh set of square brackets in equation 3.22 represent the rate of increase of thermal energy due to ohmic heating from poloidal currents (first term), in combination with the rate of decrease of magnetic energy associated with toroidal magnetic field, due to resistive decay of the poloidal currents (second term). Again, these terms cancel, which is physically representative. Referring to equation 2.11, the combination vanishes due to identity 2.18, where $\widehat{\mathbf{P}} = \left(\widehat{\eta}\,\left(\overline{\widehat{\nabla}}\,\overline{f}\right)/\widehat{r}^2\right)$ and $\overline{U} = \overline{f}$.

With reference to the definitions of the discrete forms for the thermal flux $\overline{\widehat{\nabla}}\cdot\widehat{\mathbf{q}}_\alpha$, where $\widehat{\mathbf{q}}_\alpha$ is defined in equation 3.20, it can be seen how the terms in the eighth set of square brackets in equation 3.22 vanish due to equation 2.20. Boundary conditions that are explicitly applied to the pressure fields break computational-domain-energy conservation, and enable thermal losses in accordance with the thermal conduction model and the values explicitly applied to n_0, $\left(\chi_{\parallel\alpha}\right)|_\Gamma$ and $\left(\chi_{\perp\alpha}\right)|_\Gamma$, but thermal energy fluxes through the boundary may be systematically accounted for.

To deal with the viscosity related terms in the final set of square brackets in equation 3.22, the substitutions $\overline{\mathbf{P}_1} = \left(\overline{v}_r/\overline{r}\right)\widehat{\mathbf{r}}$, $\overline{\mathbf{P}_2} = \left(\overline{v}_z/\overline{r}\right)\widehat{\mathbf{z}}$ and $\overline{\mathbf{P}_3} = \left(\overline{v}_z/\overline{r}\right)\widehat{\mathbf{r}} + \left(\overline{v}_r/\overline{r}\right)\widehat{\mathbf{z}}$ are made, and the expansion of terms, using equations 3.18, 3.19, and 2.11 is

$$\overline{dV}^T * \left\{-\overline{\mathbf{v}}\cdot\overline{\mathbf{\Pi}} + \overline{Q}_\pi\right\}$$
$$= 2\left[\overline{dV}^T * \left\{\overline{\mathbf{P}_1}\cdot\left(\overline{\widehat{\nabla}}\,\left(\widehat{\mu}\,\widehat{r}^2\,\left(\overline{\widehat{\nabla}}\cdot\overline{\mathbf{P}_1}\right)\right)\right)\right\} + \widehat{dV}^T * \left\{\widehat{\mu}\,\widehat{r}^2\,\left(\overline{\widehat{\nabla}}\cdot\overline{\mathbf{P}_1}\right)^2\right\}\right]$$
$$+ 2\left[\overline{dV}^T * \left\{\overline{\mathbf{P}_2}\cdot\left(\overline{\widehat{\nabla}}\,\left(\widehat{\mu}\,\widehat{r}^2\,\left(\overline{\widehat{\nabla}}\cdot\overline{\mathbf{P}_2}\right)\right)\right)\right\} + \widehat{dV}^T * \left\{\widehat{\mu}\,\widehat{r}^2\,\left(\overline{\widehat{\nabla}}\cdot\overline{\mathbf{P}_2}\right)^2\right\}\right]$$
$$+ \left[\overline{dV}^T * \left\{\overline{\mathbf{P}_3}\cdot\left(\overline{\widehat{\nabla}}\,\left(\widehat{\mu}\,\widehat{r}^2\,\left(\overline{\widehat{\nabla}}\cdot\overline{\mathbf{P}_3}\right)\right)\right)\right\} + \widehat{dV}^T * \left\{\widehat{\mu}\,\widehat{r}^2\,\left(\overline{\widehat{\nabla}}\cdot\overline{\mathbf{P}_3}\right)^2\right\}\right]$$
$$- \frac{2}{3}\left[\overline{dV}^T * \left\{\overline{\mathbf{v}}\cdot\left(\overline{\widehat{\nabla}}\,\left(\widehat{\mu}\,\left(\overline{\widehat{\nabla}}\cdot\overline{\mathbf{v}}\right)\right)\right)\right\} + \widehat{dV}^T * \left\{\widehat{\mu}\,\left(\overline{\widehat{\nabla}}\cdot\overline{\mathbf{v}}\right)^2\right\}\right]$$
$$+ \left[\overline{dV}^T * \left\{\underline{\omega}\,\left(\overline{\widehat{\nabla}}\cdot\left(\widehat{\mu}\,\widehat{r}^2\,\left(\overline{\widehat{\nabla}}\,\overline{\omega}\right)\right)\right)\right\} + \widehat{dV}^T * \left\{\widehat{\mu}\,\widehat{r}^2\,\left(\overline{\widehat{\nabla}}\,\overline{\omega}\right)^2\right\}\right]$$
$$- 2\left[\overline{dV}^T * \left\{\overline{\mu}\,\left(\overline{v}_r/\overline{r}\right)^2 - \overline{\mu}\,\left(\overline{v}_r/\overline{r}\right)^2\right\}\right]$$

The terms in the first to fourth sets of square brackets here vanish due to equation 2.17, where, for example, for the first set of square brackets, $\overline{\mathbf{P}} = \overline{\mathbf{P}_1}$ and $\widehat{U} = \widehat{\mu}\,\widehat{r}^2\,\left(\overline{\widehat{\nabla}}\cdot\overline{\mathbf{P}_1}\right)$. The terms in the fifth set of square brackets vanish due to equation 2.18 where $\overline{U} = \overline{\omega}$ and $\widehat{\mathbf{P}} = \widehat{\mu}\,\widehat{r}^2\,\left(\overline{\widehat{\nabla}}\,\overline{\omega}\right)$, and the terms in the final set obviously cancel. Thus, the volume-integrated rate of increase of thermal energy due to viscous heating is

balanced by the volume-integrated rate of decrease of kinetic energy due to viscous dissipation, which is also a property of the physical system.
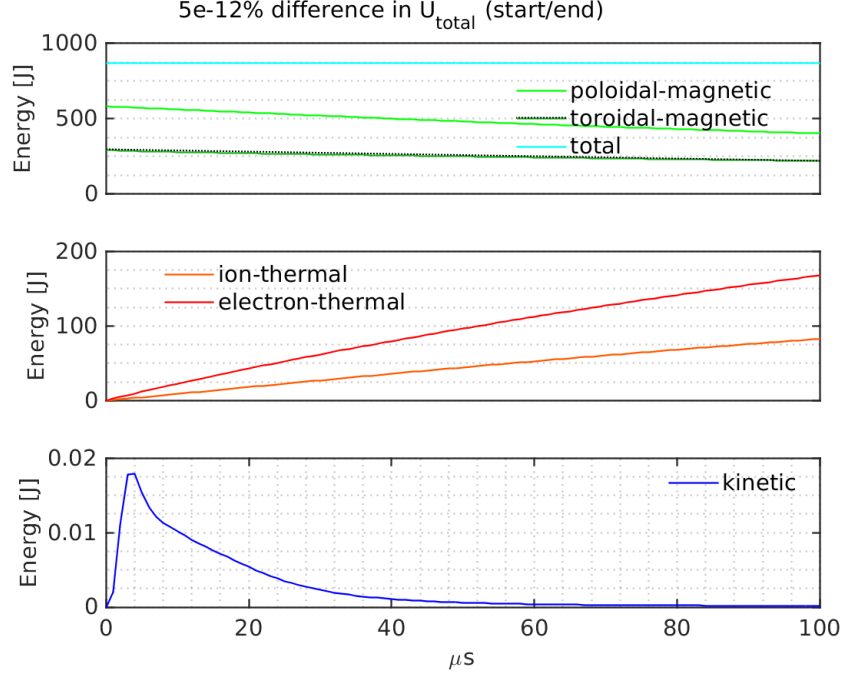

Figure 7: Energy partitions for Grad-Shafranov solution

Figure 7 shows the partition of energy, and how total energy is conserved approximately to machine precision for a 100μs simulation with moderate time-step and mesh resolution, using Runge-Kutta second order time-stepping, that started from a Grad-Shafranov equilibrium. The only explicitly applied boundary conditions are $v_r|_\Gamma = v_z|_\Gamma = \psi|_\Gamma = 0$. In contrast, simulations presented in section 6 include magnetic levitation and magnetic compression, and are run with explicitly applied boundary conditions for ψ that are determined by experiment. This enables inward electromagnetic energy fueling and outward electromagnetic losses (Poynting flux). In those simulations, boundary conditions are explicitly applied to the pressure fields to enable thermal losses in accordance with the thermal conduction model, and boundary conditions for f are explicitly applied only on the parts of the domain boundary that represent insulating regions.

4   Experiment overview
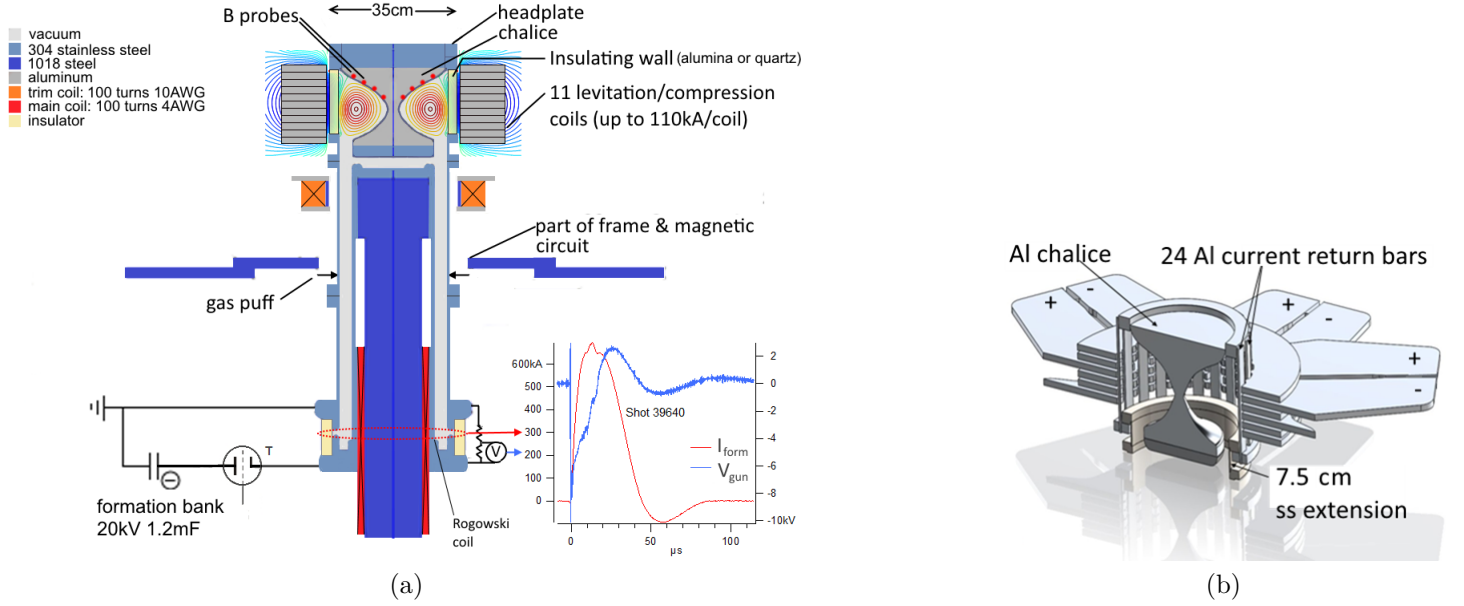
Figure 8: Machine schematic (a) and view of CT confinement region surrounded by the stack of six coil plates (b)

The structure and experiment design of the SMRT magnetic compression device can be seen in figure 8(a), with CT and levitation ψ (poloidal flux) contours from an equilibrium model superimposed, and with a schematic of the formation circuit. Measurements of formation current ($I_{form}(t)$), and voltage across the formation electrodes ($V_{gun}(t)$) are also indicated. Note that the principal materials used in the machine construction, and some key components, are indicated by the color-key at the top left of the figure. Eleven levitation/compression coils are located outside the insulating tube around the CT containment region. Figure 8(b) indicates, for the original configuration with six coils, the coils, inner tungsten-coated aluminum chalice flux conserver, stainless steel extension, and aluminum return current bars that carry axial current outside the insulating wall that is depicted in figure 8(a). A more thorough overview of the experiment can be found in [11, 12]. The sequence of machine operation is as follows:

(i) $t \sim -3$s   Main coil is energised with steady state ($\sim$ 4s duration) current, $I_{main} \sim 70$A
(ii) $t = t_{gas} \sim -400\mu$s   Gas is injected into vacuum
(iii) $t = t_{lev} \sim -400\mu$s \rightarrow -40\mu$s Levitation banks are fired ($I_{lev} \sim 180$kA)
(iv) $t = 0$s   Formation banks are fired ($I_{form} \sim 700$kA)
(v) $t = t_{comp} \sim 40\mu$s \rightarrow 150\mu$s Compression banks are fired ($I_{comp} \sim 1.2$MA)

5 Model for CT formation, levitation and magnetic compression

5.1 Boundary conditions

No boundary condition is explicitly applied to density, so that the natural boundary condition is automatically imposed:

$$(\nabla_\perp n)\,|_\Gamma = 0$$

Simulations of CT formation, levitation and magnetic compression presented here are run with all velocity components set to zero on the boundary *i.e.*, the no-slip condition for an impermeable boundary:

$$\mathbf{v}|_\Gamma = \mathbf{0}$$

Boundary conditions for pressures follow from equations 3.6, with temperatures T_i, T_e set to approximately zero at the boundary:

$$T_i|_\Gamma = T_e|_\Gamma = 0.02\text{eV} \approx 20^o\text{C}$$

Toroidal currents in the main, and levitation/compression coils constitute sources of poloidal flux, which can be included in the model with the application of appropriate boundary conditions for ψ. After assigning the material properties, solution frequencies, and peak coil currents pertaining to either the main stuffing field, the levitation field or the compression field, and running a FEMM [20] model for the relevant configuration, the values of ψ_{main}, ψ_{lev}, and ψ_{comp} at the boundary nodes are extracted to file. In the experiment, the main (stuffing) coils are energised around three seconds before the formation banks are fired, so the stuffing field can soak entirely through all materials in the model and can be modelled as being steady state, therefore the solution frequency input to FEMM for obtaining ψ_{main} is 0Hz. The solution frequency for obtaining ψ_{lev} is taken as a function of $|t_{lev}|$, the time over which the levitation field is allowed to soak into the machine before firing the formation bank. $|t_{lev}|$ is taken as the quarter-period of the current waveform input to FEMM, so that the solution frequency is $\sim$ 5kHz for typical values, from experiment, of $|t_{lev}| = 50\mu$s. Similarly, as the rise time of the compression current is $\sim 20\mu$s, the solution frequency for obtaining ψ_{comp} is taken as $\sim$ 12.5kHz. Field diffusion times in the most electrically conducting parts of the machine are much longer than the timescales associated with the levitation and compression fields. Magnetic boundary conditions are applied at all boundary nodes, but levitation boundary values are significant only on the levitation/compression coil boundaries and on the boundaries of the regions representing the stainless steel above and below the insulating wall, while compression boundary values are significant only on the coil boundaries, and are approximately zero at other boundary regions.

(a) $\widetilde{I}_{lev}(t)$ (b) $\widetilde{I}_{comp}(t)$

Figure 9: Normalised levitation (a) and compression (b) current signals

The boundary conditions for $\psi_{main}(\mathbf{r})$ are held constant over time, while boundary values obtained for $\psi_{lev}(\mathbf{r}, t)$ and $\psi_{comp}(\mathbf{r}, t)$, which pertain to the peak levitation/compression currents, are scaled over time according to the experimentally measured waveforms for $I_{lev}(t)$ and $I_{comp}(\text{t})$:

$$\psi(\mathbf{r}, t)|_\Gamma = \psi_{main}(\mathbf{r})|_\Gamma + \psi_{lev}(\mathbf{r}, t)|_\Gamma + \psi_{comp}(\mathbf{r}, t)|_\Gamma \tag{5.1}$$

Figure 9(a) shows $\widetilde{I}_{lev}(t)$, the normalised levitation current signal, as measured with Rogowski coils during the experiment; similarly, figure 9(b) shows $\widetilde{I}_{comp}(t)$. For this simulation, $t_{comp} = 45\mu s$, and the simulation was run until around 220µs. Note that $\widetilde{I}_{lev} < 1$ at $t = 0$, because $t_{lev} = -50\mu s$, *i.e.*, in the experiment, the levitation capacitor banks were fired 50µs before the formation banks. With a rise time of $\sim 40\mu s$, the levitation current peaks at $t \sim -10\mu s$, when $\widetilde{I}_{lev} = 1$. Typical peak levitation currents were $\sim 180\text{kA}$ total, peak compression currents were up to 1.2 MA.

No boundary conditions are explicitly applied to f on boundary regions representing electrical conductors. In combination with the boundary conditions for velocity, the natural boundary conditions

$$(\nabla_\perp f)\,|_\Gamma = 0$$

are automatically imposed, corresponding to the condition for a perfectly electrically conducting boundaries. Since $f = rB_\phi = \mu_0 I_\theta/2\pi$ (from Ampere's law when $\frac{\partial}{\partial\phi} = 0$), the boundary condition $(\nabla_\perp f)\,|_\Gamma = 0$ implies that any poloidal currents that flow into or out of the wall (*e.g.*, radial intra-electrode formation current or crowbarred shaft current during magnetic compression) flow perpendicular to the wall, *i.e.*, $\mathbf{E}$ has no component parallel to the boundary. Since no currents can flow in insulating regions, f must be spatially constant on the part of the boundary representing the insulating wall surrounding the CT confinement region (see section 5.2 below). As detailed below in section 5.4, the value of that constant, consistent with conservation of toroidal flux in the combined domains, is calculated at each timestep and explicitly applied as a boundary condition for f on the interface shared by the plasma and insulating domains.

5.2 Vacuum field in insulating region

As described in [11, 12], levitated CT lifetime and temperature, and the recurrence rate of shots in which the CT conserved most of its poloidal flux during compression, was increased significantly when the original six levitation/compression coil configuration was replaced with an eleven coil configuration. It is thought that the improvement in levitated CT lifetime and temperature was due to reduced levels of levitation field displacement and interaction between the plasma and insulating wall during the CT formation process, leading to consequent reductions in sputtering, plasma impurity concentration, and radiative cooling.

(a) Full mesh

(b) Full mesh (close up)

(c) Plasma mesh with indication of magnetic probe locations
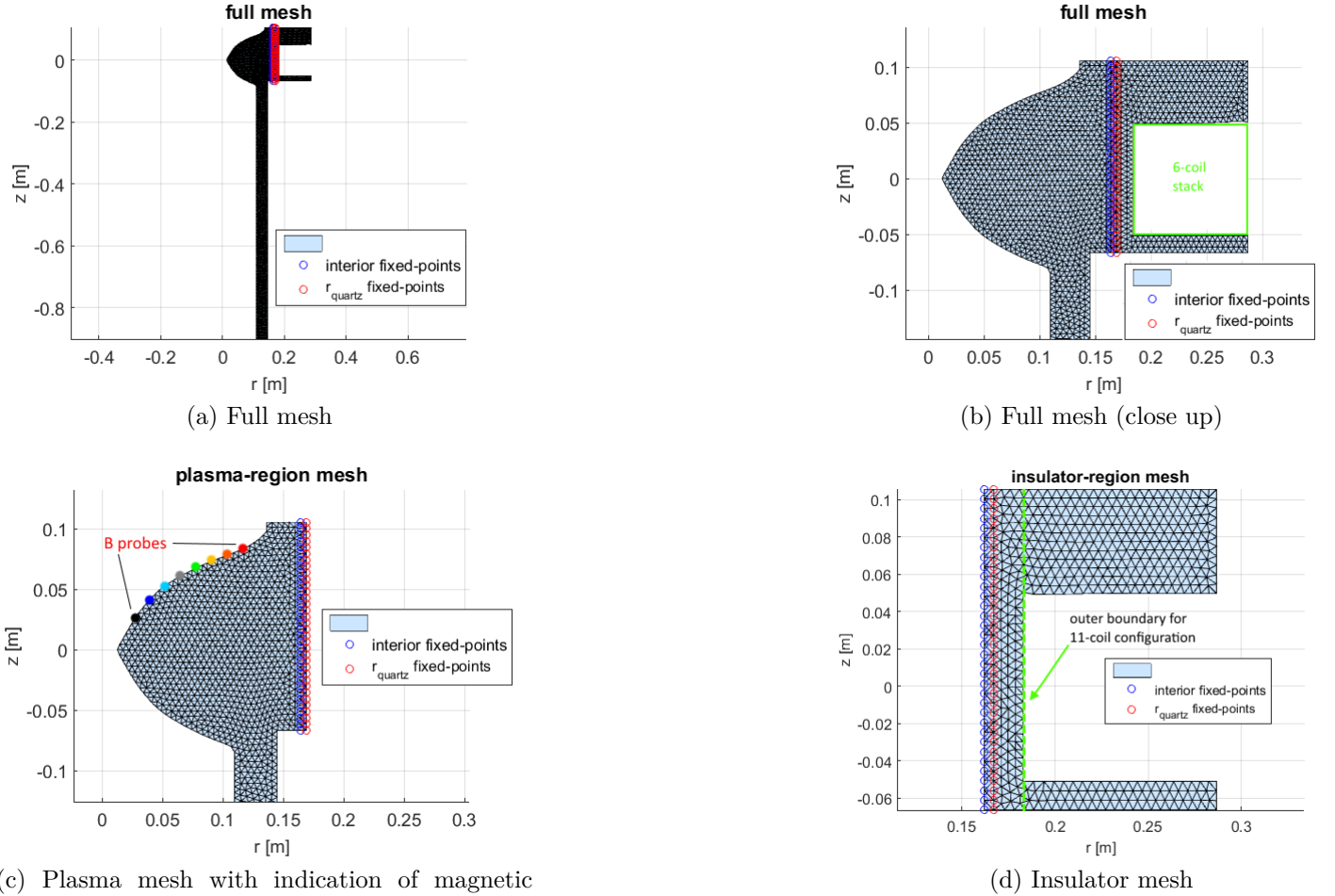

(d) Insulator mesh

Figure 10: Computational mesh with insulating region, 6-coil configuration. Note that the magnetic probe locations are indicated in (c).

In order to model the interaction of plasma with the insulating wall during the CT formation process, a vacuum field should be solved for in the insulating area between the inner radius of the insulating outer wall and the levitation/compression coils. The insulating area includes the wall itself as well as the air between the wall and the coil-stack, and the air above and below the coil-stack. If this area is included in the domain in which the plasma fields are solved, then unphysical currents will be allowed to flow in insulating regions. To solve for a vacuum field in the insulating region and couple it to the plasma fields, the computational grid for the combined plasma and insulating domain is split in two, as shown in figure 10, in which the original six levitation/compression coil configuration is being modelled. The six coil stack representation is specifically indicated in figure 10(b). For the 11-coil configuration, in which the stack of coils extends along the entire height of the insulating wall, the main part of the mesh (figure 10(c)) is unchanged, while the parts of the insulator mesh located above and below the 6-coil stack are deleted, as indicated in figure 10(d). To couple between the plasma and vacuum solutions at each timestep, we use the two vertical rows of shared fixed mesh points indicated in the figure to exchange boundary values along the plasma/insulating interface.

No currents can flow in a vacuum, so

$$\Delta^* \psi_v = 0 \tag{5.2}$$

where ψ_v represents ψ in a vacuum (or insulator). Defining $\overline{\psi}_v = \overline{\psi}_{v\Gamma} + \overline{\psi}_{vi}$, where $\overline{\psi}_{v\Gamma}$ and $\overline{\psi}_{vi}$ have the values of ψ set to zero at the nodes corresponding to internal / boundary nodes respectively, the discrete

form of equation 5.2 leads to $\overline{\overline{\Delta^*}}\,\overline{\psi}_v = \overline{\overline{\Delta^*}}\,\overline{\psi}_{v\Gamma} + \overline{\overline{\Delta_0^*}}\,\overline{\psi}_{vi} = \overline{0}$, so that:

$$\overline{\psi}_{vi} = -\left(\overline{\overline{\Delta_0^*}}\right)^{-1} * \left(\overline{\overline{\Delta^*}}\,\overline{\psi}_{v\Gamma}\right) \tag{5.3}$$

The discrete operator $\overline{\overline{\Delta_0^*}}$ is designed to produce the same results as $\overline{\overline{\Delta^*}}$ at internal nodes if the boundary values of the operand field are set to zero. The boundary values of $\overline{a}$ are preserved in the operation $\overline{c} = \overline{\overline{\Delta_0^*}}\,\overline{a}$, and do not contribute to the values calculated for elements corresponding to internal nodes in $\overline{c}$. Defining $\overline{b}\,[N_n \times 1]$ as the logical vector defining the indexes of the boundary nodes, $\overline{\overline{\Delta_0^*}}$ is defined as $\overline{\overline{\Delta_0^*}} = \overline{\overline{\Delta^*}}$, with $\overline{\overline{\Delta_0^*}}(\overline{b}, :) = \overline{\overline{\Delta_0^*}}(:, \overline{b}) = 0$, and $\overline{\overline{\Delta_0^*}}(\overline{b}, \overline{b}) = 1$. $\overline{\overline{\Delta^*}}$ and $\overline{\overline{\Delta_0^*}}$ operators based on the geometries of the plasma domain and the insulating domain were constructed. With zero initial simulated plasma density everywhere, ψ in the entire domain is initially a vacuum field, so additional $\overline{\overline{\Delta^*}}$ and $\overline{\overline{\Delta_0^*}}$ operators based on the geometry of the combined domain are required in order to construct the initial vacuum ψ solution. For formation simulations, initially the time-relevant boundary values for ψ are applied at the boundary points of the combined mesh, according to equation 5.1, and the vacuum field in the combined domain is obtained using equation 5.3. The sequence of subsequent steps followed at each timestep to couple the solutions is as follows:

1. After evolving ψ_{plasma} at the nodes in the plasma domain according to equations 3.16, boundary conditions $\psi(\mathbf{r}, t)|_\Gamma$ are applied separately to the boundary points of the plasma and insulator meshes.

2. The values at the nodes along the left boundary ("interior points" - blue circles in figure 10(d)) of the insulator mesh are overwritten using the equivalent values from ψ_{plasma}.

3. Equation 5.3 is used to calculate ψ_v in the insulating area.

4. Finally, the values at the outer right boundary of the plasma-grid (red circles in figure 10(c)) are overwritten using the equivalent values from the insulating region solution ψ_v.

5.3   Formation Simulation

Physically, CT formation in a magnetized Marshall gun is achieved as a result of $\mathbf{J}_r \times \mathbf{B}_\phi$ forces acting on plasma, where $\mathbf{J}_r$ is the radial formation current density across the plasma between the electrodes, and $\mathbf{B}_\phi$ is the toroidal field due to the axial formation current in the electrodes. Open stuffing magnetic field lines that are resistively pinned to the electrodes, and frozen into the conducting plasma, are advected with the plasma by the $\mathbf{J}_r \times \mathbf{B}_\phi$ force, into the containment region, where they reconnect to form CT closed flux surfaces. Simulated formation is initiated with the addition of toroidal flux below the physical locations of the gas puff valves - initial radial formation current is assumed to occur at the z-coordinate of the valves, where the gas density is initially highest.

When this external source of toroidal flux is included, the continuous form of the expression for the time-rate of change of f is

$$\dot{f}(\mathbf{r}, t) = r^2 \nabla \cdot \left(-\frac{f}{r^2}\mathbf{v} + \omega\mathbf{B} + \frac{\eta}{r^2}\nabla f \right) + \dot{f}_{form}(z, t) \tag{5.4}$$

In practice, the expression for f_{form} is added to the existing value for f at the beginning of each timestep, so that the natural toroidal flux conserving boundary condition $((\nabla_\perp f)|_\Gamma = 0)$ is maintained on electrically conducting boundaries. Conservation of the system's intrinsic toroidal flux implies that the total system flux is equal to the initial flux plus the flux added due to $f_{form}(z, t)$, at each time.

Integrating Faraday's law in the poloidal plane over the area defining the formation current path (up the outer gun electrode as far as the region with the initially highest gas concentration at the z-coordinate of the valves, through the plasma across the intra-electrode gap, and down the inner electrode) we have:

$$\int \nabla \times \mathbf{E}_\theta(\mathbf{r}, t) \cdot d\mathbf{S} = -\int \dot{\mathbf{B}}_\phi(\mathbf{r}, t) \cdot d\mathbf{S}$$

$$\Rightarrow \int \mathbf{E}_\theta(\mathbf{r}, t) \cdot d\mathbf{l} = V(t) = -\dot{\Phi}_{form}(t)$$

$$\Rightarrow \Phi_{form}(t) = -\int_0^t V(t') \, dt' \tag{5.5}$$

Here,

$$V(t) = V_{gun}(t) + I_{form}(t) \, R(t) \tag{5.6}$$

where $V_{gun}(t)$ is the voltage measured across the formation electrodes and $I_{form}(t) \, R(t)$ is the resistive voltage drop along the formation current path. $\mathbf{E}_\theta(\mathbf{r}, t)$ is the poloidal electric field that is established through the application of $V_{gun}(t)$, and $\dot{\mathbf{B}}_\phi(\mathbf{r}, t)$ and $\dot{\Phi}_{form}(t)$ are the time-rates of change of the toroidal magnetic field and toroidal flux induced in the area bounded by the path along which formation current driven by $\mathbf{E}_\theta(\mathbf{r}, t)$ flows.

For the simplifying assumption of a fixed formation current path of constant inductance, $-V(t) = \dot{\Phi}_{form}(t) = L\dot{I}_{form}(t)$, where $I_{form}(t)$ is the formation current and L is the inductance of the formation current path. $R(t)$ in equation 5.6 is a resistance that depends on the resistivity of the metal along the formation current path, and also on the resistivity of the plasma between the gun electrodes. In addition, it is expected that when plasma, which is advected upwards during the formation process, occupies the gap between the chalice and the inner gun electrode (see figure 8(a)), that part of the formation current will flow on a path up the outer electrode, through the aluminum bars located outside the insulating wall (see figure 8(b)), down the chalice, across the plasma in the gap and down the inner electrode. Physically, $R(t)$ includes the contribution of the resistance of the plasma in the gap shortly after initiation of the formation process. Note that the chalice (*i.e.*, the inner flux conserver indicated in figure 8(b)) and inner electrode are modelled as a continuous conductor - we do not have sufficient information, for example the voltage measured across the gap, to properly model the effect of the gap. For simplicity, we assume here that R is constant in time. Thus the expression for the voltage measured across the formation electrodes is

$$-V_{gun}(t) = L\dot{I}_{form}(t) + I_{form}(t)R$$

$$= \dot{\Phi}_{form}(t) + \frac{\Phi_{form}(t)}{\tau_{LR}} \tag{5.7}$$

where $\tau_{LR} = L/R$ is the LR time determining the formation current decay rate. This time constant can be estimated from the e-folding time of the toroidal field that is experimentally measured at the probes indicated in figure 8(a). The toroidal field at the probes is a measure of the crow-barred shaft current that flows poloidally around the machine after formation. The value of τ_{LR} varies depending on the formation current path and resistances of the intra-electrode plasma and the plasma in the gap between the chalice and the gun inner electrode, so it can vary from shot to shot depending on plasma conditions. For relatively long-lived magnetically levitated CTs, $\tau_{LR} \sim 90\mu s$. Reduced values of τ_{LR} can be chosen as a simulation input when shorter-lived CTs (*e.g.*, for simulations with relatively high thermal diffusion coefficients, or low flux CTs associated with reduced V_{form} and I_{main}) are being modelled. Equation 5.7 can be solved as

$$\Phi_{form}(t) = -e^{-\frac{t}{\tau_{LR}}} \int_0^t V_{gun}(t') \, e^{\frac{t'}{\tau_{LR}}} \, dt' \tag{5.8}$$

By definition,

$$\Phi_{form}(t) = \int \frac{f_{form}(z,t)}{r} dr\ dz \tag{5.9}$$

$f_{form}(z,t)$ may be expressed as

$$f_{form}(z,t) = A_{form}(t)\,g_{form}(z,t) \tag{5.10}$$

where $A_{form}(t)$ determines the amplitude of $f_{form}(z,t)$, and $g_{form}(z,t)$ is a geometric profile that determines where plasma formation current flows. The smooth logistic profile

$$g_{form}(z,t) = \frac{e^{m\,z_I(t)}}{e^{m\,z_I(t)} + e^{m\,z}} \tag{5.11}$$

defines $g_{form}(z,t)$, where $m \sim 40$ defines the profile slope, and $z_I(t)$ is the z coordinate at which the greatest concentration of radial formation current flows between the machine electrodes. For simplicity, we neglect the time dependence in g_{form} by replacing $z_I(t)$ with $z_{gp} = -0.43$m, the z coordinate of the machine's gas puff valves, around which the greatest concentration of radial formation current is expected to flow.

(a)

(b)
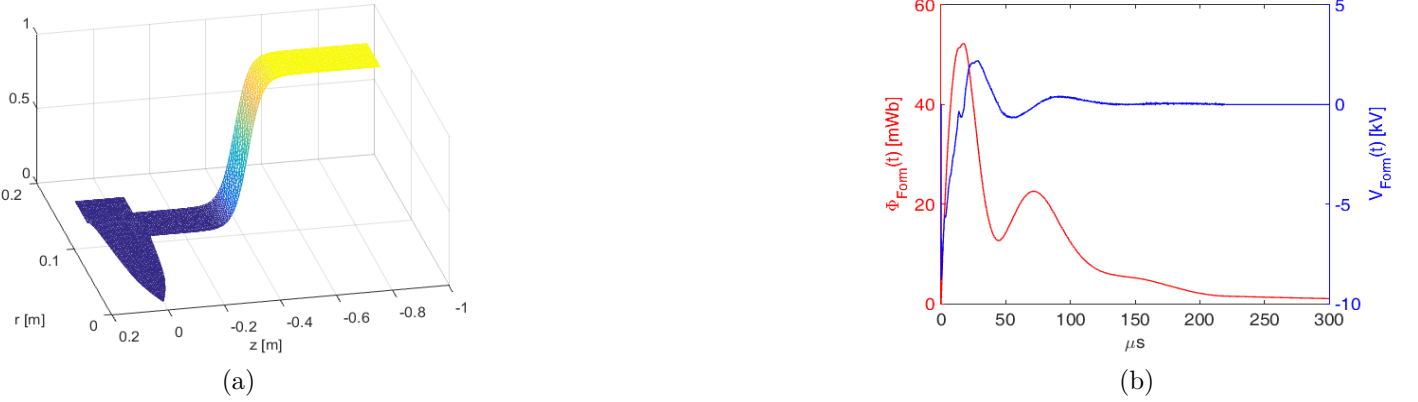
Figure 11: Logistic function $g_{form}(z)$ profile for formation flux input (a), and measured $V_{gun}(t)$ with calculated $\Phi_{form}(t)$ (b)

The logistic function formation profile is shown in figure 11(a). As outlined in [11], it is possible to reproduce the measured formation current over the bulk of the simulated formation process, when the time dependence of g_{form} is included. Figure 11(b) shows the experimentally measured formation voltage signal (right axis) which is numerically integrated over time to evaluate $\Phi_{form}(t)$ (left axis) as defined by equation 5.8.

Combining equations 5.9 and 5.10, we have:

$$\Phi_{form}(t) = A_{form}(t) \int \frac{g_{form}(z)}{r} dr\ dz \tag{5.12}$$

Together with equation 5.8, this gives:

$$A_{form}(t) = \frac{-e^{-\frac{t}{\tau_{LR}}} \int_0^t V_{gun}(t')\,e^{\frac{t'}{\tau_{LR}}}\ dt'}{\int \frac{g_{form}(z)}{r} dr\ dz} \tag{5.13}$$

Combining equations 5.10 and 5.13 yields the expression for $f_{form}(z,t)$, which is used in equation 5.4 to simulate the formation process:

$$f_{form}(z,t) = \left(-e^{-\frac{t}{\tau_{LR}}} \int_0^t V_{gun}(t')\,e^{\frac{t'}{\tau_{LR}}}\ dt'\right)\left(\frac{g_{form}(z)}{\int \frac{g_{form}(z)}{r} dr\ dz}\right) \tag{5.14}$$

5.4 Φ conservation with insulating wall

Integrating toroidal field over the area of the total domain (combined plasma and insulating wall regions) in the poloidal plane, we have:

$$\Phi_{tot}(t) = \underbrace{\int_{\Omega_P} \frac{f_P(\mathbf{r},t)}{r} dr\, dz + \int_{\Omega_I} \frac{f_I(t)}{r} dr\, dz}_{\Phi_{PI}(t)} + \underbrace{\int_{\Omega_P+\Omega_I} \frac{f_{form}(z,t)}{r} dr\, dz}_{\Phi_{form}(t)} \tag{5.15}$$

The subscripts P and I refer to plasma and insulating wall regions. Note that the insulating wall area includes the insulating wall only, and not the insulating (air) regions above and below the coil stack as depicted in figure 10. Poloidal currents in the aluminum bars located outboard of the insulating wall (depicted in figure 8(b)) add toroidal flux to the system only in the insulating wall and plasma regions. Since no currents can flow in insulators, f must be spatially constant in the insulating wall inside aluminum bars. The flux-conserving natural boundary condition that is imposed on f_P (which is evolved according to equation 5.4) must be overwritten on the interface between the insulating wall and the plasma domain. The second term in equation 5.15 can be re-expressed as $\int_{\Omega_I} \frac{f_I(t)}{r} dr\, dz = f_I(t)\, h_I \ln(r_{out}/r_{in})$, where h_I is the height of the rectangular cross-section of the insulating wall, and r_{out} and r_{in} are the outer and inner radii of the wall. Initial system toroidal flux is zero, and $\Phi_{PI}(t)$ is to be conserved by design, so the system's only source of toroidal flux is $\Phi_{form}(z,t)$:

$$\Phi_{tot}(t) = \Phi_{form}(t) \Rightarrow \Phi_{PI}(t) = 0$$
$$\Rightarrow \int_{\Omega_P} \frac{f_P(\mathbf{r},t)}{r} dr\, dz + \int_{\Omega_I} \frac{f_I(t)}{r} dr\, dz = 0$$
$$\Rightarrow \sum_{i=1}^{N_n} \left(\frac{f_{P_i}(t)\, s_i}{3 r_i} \right) + f_I(t)\, (h_I \ln(r_{out}/r_{in})) = 0 \tag{5.16}$$

Here, N_n is the number of nodes in the non-insulating part of the domain (*i.e.*, the plasma domain) in which the MHD equations are solved, $s_i/3$ is the area, and r_i is the radial coordinate, associated with node i. The summation is over all nodes in the plasma domain, which includes the fixed-point nodes along the inner radius of the insulating wall, at which we want to evaluate f_I. Equation 5.16 can be solved for the constant f_I if f_{P_i} is temporarily set to zero at the fixed-point nodes along the inner wall of the insulator (see figure 10), so that $f_P \to f_{P0}$. Equation 5.16 is modified as:

$$\sum_{i=1}^{N_n} \left(\frac{f_{P0_i}(t)\, s_i}{3 r_i} \right) + \left(\sum_{j=1}^{N_{int}} \left(\frac{s_j}{3 r_j} \right) + h_I \ln(r_{out}/r_{in}) \right) f_I(t) = 0 \tag{5.17}$$

Here, $\sum_{j=1}^{N_{int}}$ implies summation over the interface fixed-point nodes along the inner insulating wall. In equation 5.17, $\tilde{L}_{ins} = h_I \ln(r_{out}/r_{in})$ is related to the inductance of the insulating wall's cross-sectional area (recall that the inductance of a co-axial cable is $L_{coaxial} = \frac{\mu_0}{2\pi} l \ln(r_{out}/r_{in})$, where l is the length of the coaxial cable and r_{out}/r_{in} are the cable's outer and inner radii), and $\tilde{L}_{int\Delta} = \sum_{j=1}^{N_{int}} \left(\frac{s_j}{3 r_j} \right)$ is related to the inductance of the area of the parts of the triangular elements in the plasma domain that are associated with the interface fixed point nodes. The resulting expression for f_I is:

$$f_I(t) = \frac{-1}{\tilde{L}_{ins} + \tilde{L}_{int\Delta}} \sum_{i=1}^{N_n} \left(\frac{f_{P0_i}(t) s_i}{3 r_i} \right) \tag{5.18}$$

The constant f_I is calculated at each timestep and is applied as a boundary condition for f on the interface shared by the plasma domain and the insulating domain, resulting in conservation of total toroidal flux in the combined domains.
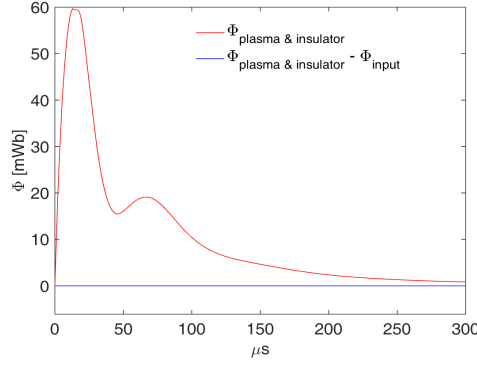
Figure 12: Indication of toroidal flux conservation for MHD simulation of CT formation

Now, with the natural boundary condition $(\nabla_\perp f)\,|_\Gamma = 0$ imposed at all boundary points in the plasma domain (in combination with the explicitly applied boundary conditions $\overline{\mathbf{v}}|_\Gamma = \mathbf{0}$), and with equation 5.18 used to overwrite the values for f_P on the interface, intrinsic toroidal flux conservation is ensured in the combined computational domain. As indicated in figure 12 toroidal flux is conserved over time for simulations of CT formation - total flux less input (formation-associated) flux is zero at all times.

6 Simulation results, and comparison with experiment

In this section, results from an MHD simulation of CT formation into a levitation field, and magnetic compression will be presented and compared with experimental results. The models described in section 5 have been incorporated. All simulation and experiment results presented will correspond to the machine configuration with eleven levitation/compression coils, with the exception that simulations of CT formation will be compared across the two configuration in section 6.2. Note that code verification studies have been performed to confirm convergence of the field solutions with decreasing element size or timestep. In addition, the Grad-Shafranov equilibrium and q profile solutions have been benchmarked against the corresponding solutions from the well-established Corsica code [21]. Verification studies, and the methods implemented to evaluate the equilibrium and q profile solutions within the DELiTE framework, are presented in [11].

In total, there are over one hundred code input parameters. Principal code input parameters for the simulation results presented in this section are as follows:

- h_e=2mm defines the mesh resolution.

- $V_{form} = 16$kV, $I_{main} = 70$A, $V_{lev} = 16$kV, $V_{comp} = 18$kV: The formation gun voltage waveform used to calculate $\Phi_{form}(t)$ in the expression for $f_{external}(z,t) = f_{form}(z,t)$ (equation 5.8) is taken from an experimental measurement for a typical shot with $V_{form} = 16$kV, where V_{form} is the voltage to which the formation capacitor banks were charged. As described in section 5.1, the boundary conditions for ψ, pertaining to ψ_{main}, ψ_{lev}, and ψ_{comp} are obtained using FEMM models. For the FEMM model used to find ψ_{main}, the dc current in the main coil was set to $I_{main} =$70A. Similarly, the currents in the levitation and compression coils in the FEMM models, used to obtain boundary conditions for ψ_{lev} and ψ_{comp}, were set to the experimentally measured values corresponding to experimentally recorded $V_{lev} = 16$kV and $V_{comp} = 18$kV (voltages to which the levitation and compression capacitor banks were charged) respectively. Note that the waveform for V_{form}, and the boundary values pertaining to the peak values of ψ_{main}, ψ_{lev}, and ψ_{comp}, can be linearly scaled according to the settings for V_{form}, I_{main}, V_{lev} and V_{comp} that are required for a particular simulation.

31

- $t_{comp} = 45\mu s$ means that magnetic compression (*i.e.*, superimposition of the ψ_{comp} boundary conditions, scaled by experimentally recorded $\widetilde{I}_{comp}(t)$, on the ψ_{main} and ψ_{lev} boundary conditions, see section 5.1) is started 45μs into the simulation.

- $m_0 = 4$ implies that the ion mass is four proton masses ($m_p = 1.67 \times 10^{-27}$kg), which is relevant for modeling helium plasmas.

- $Z = 1.3$ defines the estimate for the (volume averaged) ion charge, and determines the ratio of electron to ion number density ($n_e = Z\,n_i$). The plasma is being modeled as a single fluid, while the energy equation is split into ion and electron components, so Z determines the ratio between the ion and electron pressures ($p = p_i + p_e = n\,(T_i[\text{J}] + Z\,T_e[\text{J}])$, where $n \iff n_i$). Z also enters into the determination of plasma Spitzer resistivity and the ion-electron heat exchange term Q_{ie}. Fully ionized pure helium plasma would have $Z = 2$, here we assume that a proportion of the helium atoms are only singly ionized. Z can be increased to include some of the effects of the inclusion of high ionic-charge impurities in the plasma.

- Code inputs $n_0[\text{m}^{-3}] = 9 \times 10^{20}[\text{m}^2/\text{s}]$ and $\sigma_n^2 = 0.005$ [m^2] determine the initial plasma density distribution. σ_n^2 [m^2] defines the variance of the Gaussian function that defines the distribution, which is centered around $z_{gp} = -0.43$m, the z coordinate of the physical location of the machine gas puff valves. The initial number density distribution is

$$n_{t0}(z) = n_0\,((n_{high} - n_{low})\,\widetilde{g}(z) + n_{low}) \tag{6.1}$$

where $\widetilde{g}(z) = g(z)/\max(g(z))$. Here, $g(z) = \frac{1}{\sqrt{2\pi\,\sigma_n^2}} exp\left(\frac{-(z-z_{gp})^2}{2\sigma_n^2}\right)$. n_{high} and n_{low} are typically set to 10 and 0.1 respectively. Note that n_{low} must be finite - density is not allowed to approach too close to zero anywhere in the computational domain. The sound speed of a neutral gas is given by $V_s = \sqrt{\frac{\gamma p}{\rho}}$. At room temperature, for helium gas, this is $V_s \approx 900$m/s. In a typical shot, gas is puffed into the vacuum vessel through the eight gas valves spaced toroidally on the outer electrode, around 400μs before firing the formation capacitors. A simple estimate of d_n, the maximum spread of the neutral gas around the valves can be estimated using this time and the sound speed, as $d_n = 0.36$m, so that choosing $\sigma_n^2 = 0.005$m^2, corresponding to a Gaussian base width of around 0.45m, is a reasonable estimate for the initial spread. See figure 15(a) for the initial density profile pertaining to these input parameters. Note that for the simulation presented here, interaction between plasma and neutral fluid is included in the model, where the initial neutral particle inventory distribution is also determined by a Gaussian profile centered around the location of the machine gas valves. Results from simulated neutral fluid dynamics, and a description of the model for plasma-neutral interaction, won't be discussed further here; this material is presented separately in [22].

- ζ is the density diffusion coefficient, note that 50 [m^2/s] is close to the minimum value required for numerical stability for simulations that include CT formation and magnetic compression.

- $\nu_{num} = 700$m^2/s and $\nu_{phys} = 410$m^2/s: ν_{num} is the value for the viscosity diffusion coefficient that defines μ, in the viscous terms in the momentum equation (see equation 3.18), as $\mu_{num} = m_i n_0\,\nu_{num}$. To reduce viscous heating of the ions to acceptable levels (*i.e.*, to achieve a match between experimentally measured and simulated ion temperatures), a reduced value $\mu_{phys} = m_i n_0\,\nu_{phys}$ defines μ in the viscous term in the ion energy equation (see equation 3.19). At 700m^2/s, ν_{num} is close to the minimum value required for numerical stability (*i.e*, sufficient velocity field smoothing), while $\nu_{phys} = 410$m^2/s is chosen as a crude estimate for the "physical" viscosity because it leads to simulated ion temperature close to the levels indicated by the ion-Doppler system. Ideally, the strategy of having different values for ν_{num} and ν_{phys} would be avoided because it breaks the conservation of system energy pertaining to the viscous terms (the terms in the last set of square brackets in

equation 3.22). However, it was found that the discrepancy does not, apart from a reduction in ion viscous heating, significantly alter these particular simulation results, and appears at this stage to be an acceptable method for reducing ion heating in simulation scenarios with low density and high plasma velocities.

- Code input parameters pertaining to the thermal diffusion coefficients, which are held constant in this simulation, are $\chi_{\parallel e} \sim 16000 \,[\mathrm{m^2/s}]$, $\chi_{\parallel i} \sim 5000 \,[\mathrm{m^2/s}]$, $\chi_{\perp e} \sim 240 \,[\mathrm{m^2/s}]$, and $\chi_{\perp i} \sim 120 [\mathrm{m^2/s}]$. The high field-parallel thermal diffusion coefficients represent rapid equilibration of temperature along field lines, while the field-perpendicular coefficients are chosen to match the experimentally observed resistive decay rate of CT currents. Enhanced thermal diffusion acts as a proxy for anomalous energy sink mechanisms, including radiative losses.
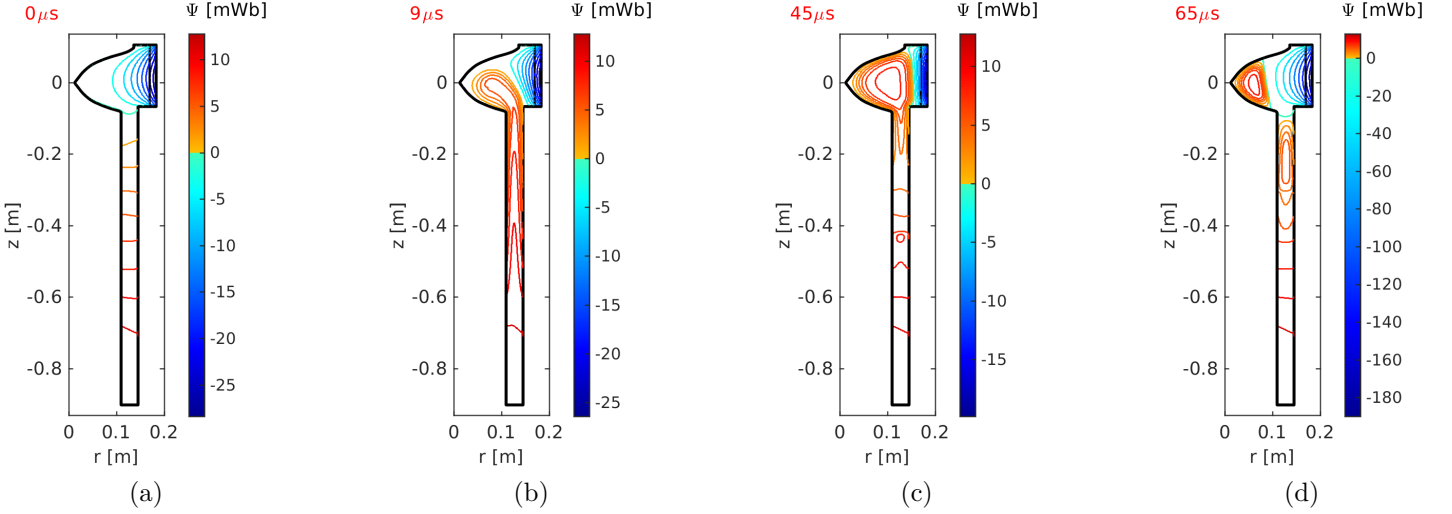
Figure 13: Poloidal flux contours, 11-coil configuration, at 0μs (a), 9μs (b), 45μs (c), 65μs (d). Note that the colorbar scaling changes over time (here and in subsequent contour plots).

Figure 13 shows simulated ψ contours, representing poloidal magnetic field lines, at various times for a simulation of CT formation, levitation and magnetic compression in the eleven coil configuration, with code input parameters as defined above. Note that the vertical black line at the top-right of the figures at $r \sim 17$cm represents the inner radius of the insulating wall. Vacuum field only is solved for to the right of the line, and the plasma dynamics are solved for in the remaining solution domain to the left of the line. The inner radius of the stack of eleven levitation/compression coils (which are not depicted here) is located at the outer edge of the solution domain, at $r \sim 18$cm. Simulation times are notated in red at the top left of the figures. Note that $\max(\psi)$ decreases slowly over time as the CT decays, while $\min(\psi)$ increases as the levitation current in the external coils decays, and then drops off rapidly as the compression current in the external coils is increased, starting at $t_{comp} = 45$μs in this simulation. At time $t = 0$, the stuffing field ($\psi > 0$) due to currents in the main coil fills the vacuum below the containment region, and has soaked well into all materials around the gun, while the levitation field fills the containment region. As described in section 5.3, simulated CT formation is initiated with the addition of toroidal flux below the gas puff valves located at $z = -0.43$m; initial intra-electrode radial formation current is assumed to flow at the z-coordinate of the valves. Open field lines that are resistively pinned to the electrodes, and partially frozen into the conducting plasma, have been advected by the $\mathbf{J}_r \times \mathbf{B}_\phi$ force into the containment region by $t = 9$μs ($\mathbf{J}_r$ is the radial formation current density across the plasma between the electrodes, and $\mathbf{B}_\phi$ is the toroidal field due to the axial formation current in the electrodes). By 45μs, open field lines have reconnected at the entrance to the containment region to form closed CT flux surfaces. At these early times, open field lines remain in place surrounding the CT. Compression starts at 45μs and peak compression is

33

at 65μs. Note magnetic compression causes closed CT poloidal field lines that extend down the gun to be pinched off at the gun entrance, where they reconnect to form a second smaller CT. Field lines that remain open surrounding the main CT are then also reconnectively pinched off, forming additional closed field lines around the main CT, while the newly reconnected open field lines below the main CT act like a slingshot that advects the smaller CT down the gun, as can be seen at 65μs. The CT expands again between after peak compression at 65μs as the compression current in the external levitation/compression coils decreases. Note that 2D simulations, which neglect inherently three dimensional turbulent transport and flux conversion, generally overestimate the level of hollowness of the field profiles.
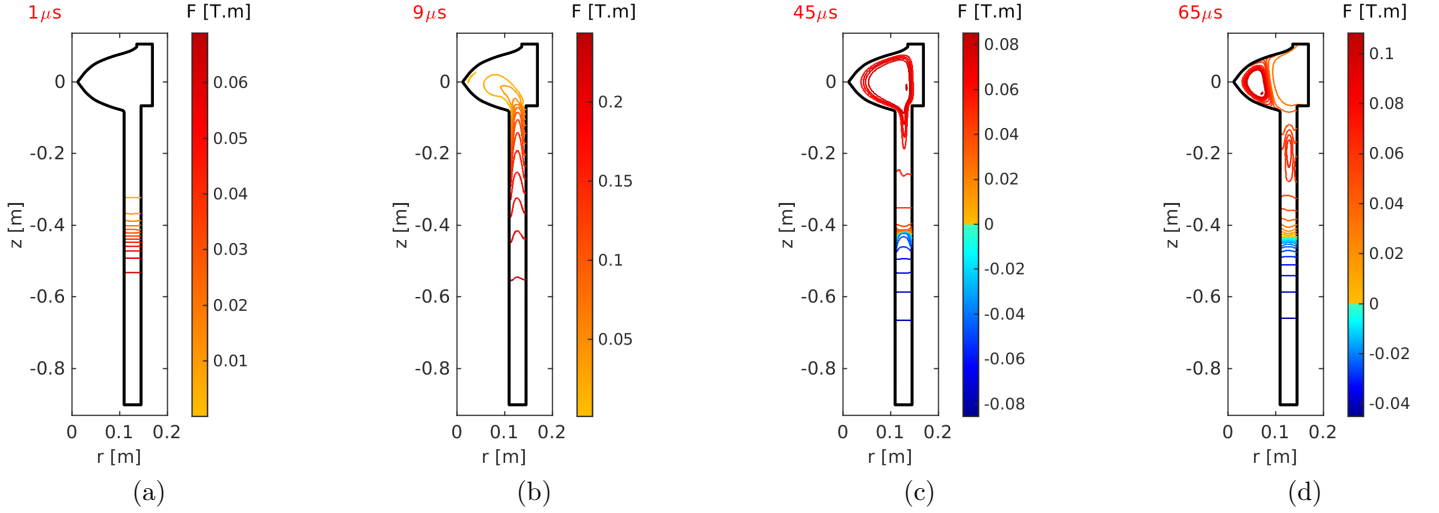
Figure 14: f contours (lines of poloidal current), at 0μs (a), 9μs (b), 45μs (c), 65μs (d)

Contours of f at various times are shown in figure 14. Recall that contours of $f = rB_\phi$ represent lines of poloidal current. Initially, f is zero at all nodes. At 1μs, it can seen how radial formation current between the gun electrodes, corresponding to the axial gradient of f, is concentrated around the gas valve location, at $z = -0.43$m. Closely spaced contours indicate regions of high gradients and high poloidal currents. To simulate formation, toroidal flux is being added to the domain according to the geometric profile shown in figure 11(a). At 1μs, f is constant, at its highest value in the domain, below the lowermost contour at $z \sim -0.55$m representing $f \sim 0.07$ T-m. By 9μs, plasma has been advected upwards, and poloidal current is flowing along open poloidal magnetic field lines that remain resistively pinned to the electrodes down the gun. By 45μs (figure 14(c)) poloidal current is flowing along closed and open poloidal magnetic field lines, and most of the toroidal flux in the domain has been advected with the plasma into the containment region. At this time, as the level of toroidal flux added to the domain below the gas valve locations, which is equal to the total toroidal flux in the domain, falls off (see figure 12), radial currents between the electrodes further down the gun reverse direction, and f becomes negative, as consequences of toroidal flux conservation and upward advection of toroidal flux. As shown in figure 14(d), poloidal current flows around the closed poloidal field lines of the main CT as it is being compressed, and around the closed poloidal field lines of the smaller pinched off CT at 65μs. Total toroidal flux is conserved, leading to induced internal currents between various points on the conducting walls. In particular, the wall-to-wall currents, that are apparent outboard of the CT at peak compression (figure 14 (d)), are thought to be a representation of real physical phenomenon which led to experimentally measured toroidal field signals that suggested the appearance of an external kink instability at compression, as described in detail in [11, 12].
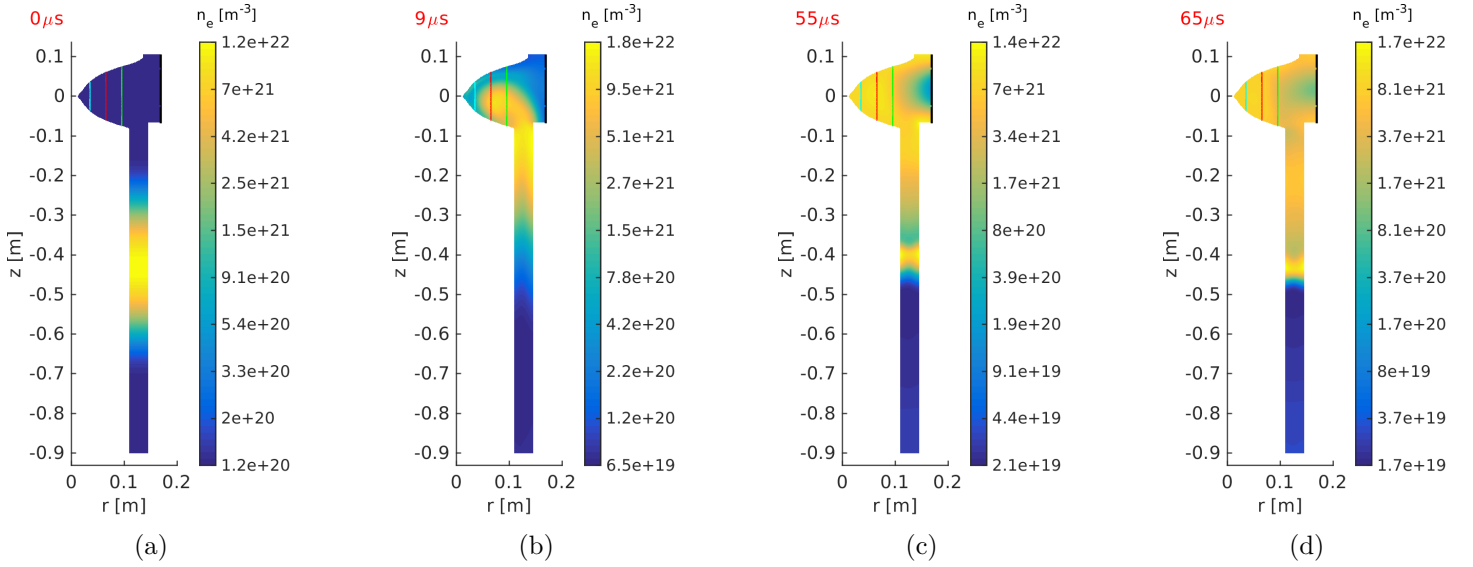
Figure 15: Electron density profiles at 0µs (a), 9µs (b), 55µs (c), 65µs (d). The vertical blue, red and green chords represent the lines of sight of the interferometer measurements, along which simulated line averaged-electron density is evaluated for comparison with experimental data.

The initial electron density profile is shown in figure 15(a). As described earlier, the initial density profile is defined with a Gaussian profile centered around the axial coordinate of the locations of the gas puff valves. Plasma is advected up the gun during CT formation, and bubbles-in to the containment region, as shown in figure 15(b). In figures 15(c) and (d), it can be seen how density rises over compression around the CT core, and that a region of low density remains outboard of the compressed CT.
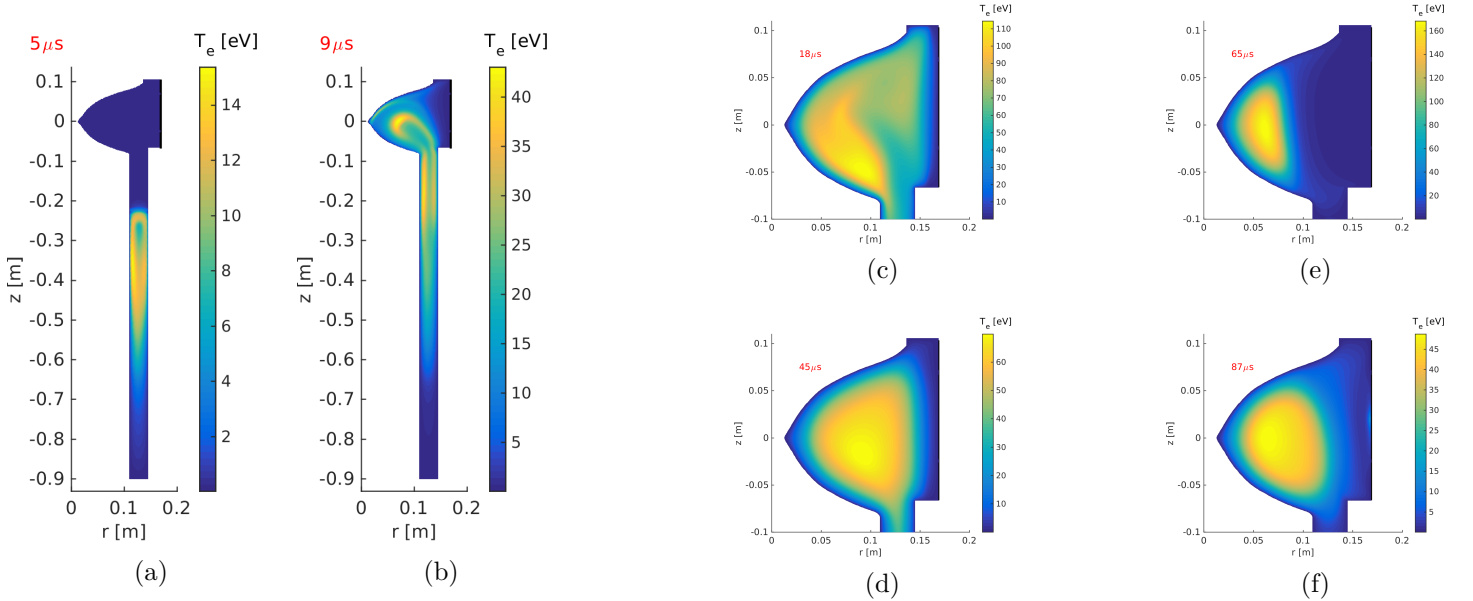
Figure 16: Electron temperature profiles at 5µs (a), 9µs (b), 18µs (c), 45µs (d), 65µs (e), 87µs (f)

Formation current ohmically heats initially cold electrons as plasma is pushed up the gun into the containment region (figures 16(a) and (b)). The 115 eV attained by electrons near the containment region entrance at 18µs (figure 16(c)) is partially due to heat exchange with ions, which, as indicated in figure 17(c)), have been heated to around 280eV near the same area at this time due to viscous heating. Thermal diffusion through the boundary causes the electron temperature around the CT core to be reduced to around 70 eV just prior to magnetic compression at 45µs. Electron temperature is more than doubled, to 165 eV,

35

at peak magnetic compression at 65μs (figure 16(e)). Referring to figure 18, it can be seen how ohmic heating is a principal electron heating mechanism. Compressional heating is the main heating mechanism during magnetic compression, and is supplemented by enhanced ohmic heating. Compression coil current falls to zero by around 87μs, by which time the CT has re-expanded, and core electron temperature has fallen to around 50 eV (figure 16(f)).
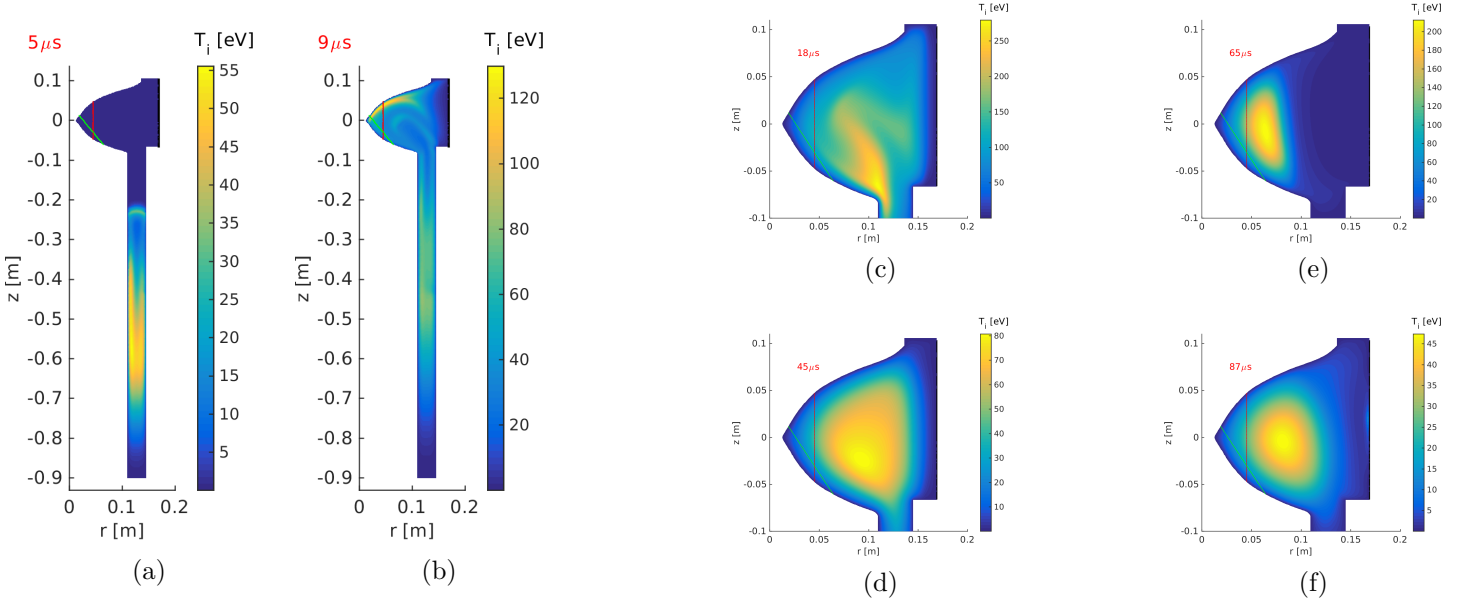

Figure 17: Ion temperature profiles at 5μs (a), 9μs (b), 18μs (c), 45μs (d), 65μs (e), 87μs (f). The vertical red chord and diagonal green chord in the CT containment region represent the lines of sight of the ion-Doppler measurements, along which simulated line-averaged ion temperature is evaluated for comparison with experimental data.

Simulated ion temperatures, at the same times referred to in figure 16 for electron temperatures, are shown in figure 17. Over the early stages of the simulation, ion temperature is significantly higher than electron temperature, due to ion viscous heating during the formation process. Later, ohmic heating of electrons is the main heating source and electron temperature approaches ion temperature. Note that, as a result of compressional heating in combination with heat exchange with the electrons, which are heated ohmically by enhanced currents during compression, ion temperature is more than doubled at peak compression, increasing from around 80 to 210eV from 45μs to 65μs. The vertical red chord and diagonal green chord in the CT containment region in figures 17(a) to (g) represent the lines of sight of the ion-Doppler measurements, along which simulated line-averaged ion temperature is evaluated for comparison with experimental data.
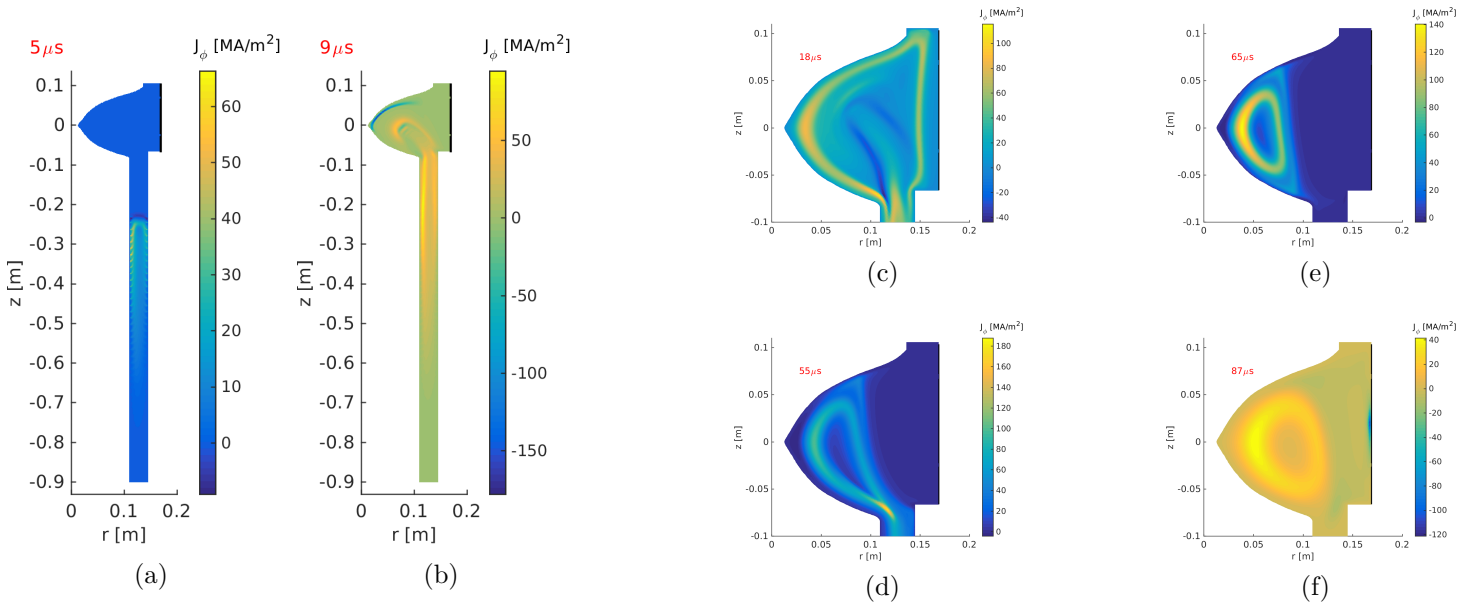
Figure 18: Toroidal current density profiles at 5μs (a), 9μs (b), 18μs (c), 55μs (d), 65μs (e), 87μs (f)

Simulated toroidal current density is shown at various times in figure 18. Comparing with figure 16, it can be seen how ohmic heating is a principal electron heating mechanism. Note the high concentration of J_ϕ near the entrance to the CT confinement region at 55μs (figure 18(d)), relating to the toroidally directed current sheet present between oppositely directed poloidal field lines during the magnetic reconnection process that occurs as closed CT field lines that extend down the gun, and then open field lines surrounding the CT, are pinched off during magnetic compression. A reconnection-related current sheet is also evident when open poloidal field lines reconnect to form closed CT flux surfaces, for example at 18μs (figure 18(c)). Toroidal current, and hence ohmic heating of the electrons, increases significantly over the compression cycle, as seen in figures 18(d) and (e).
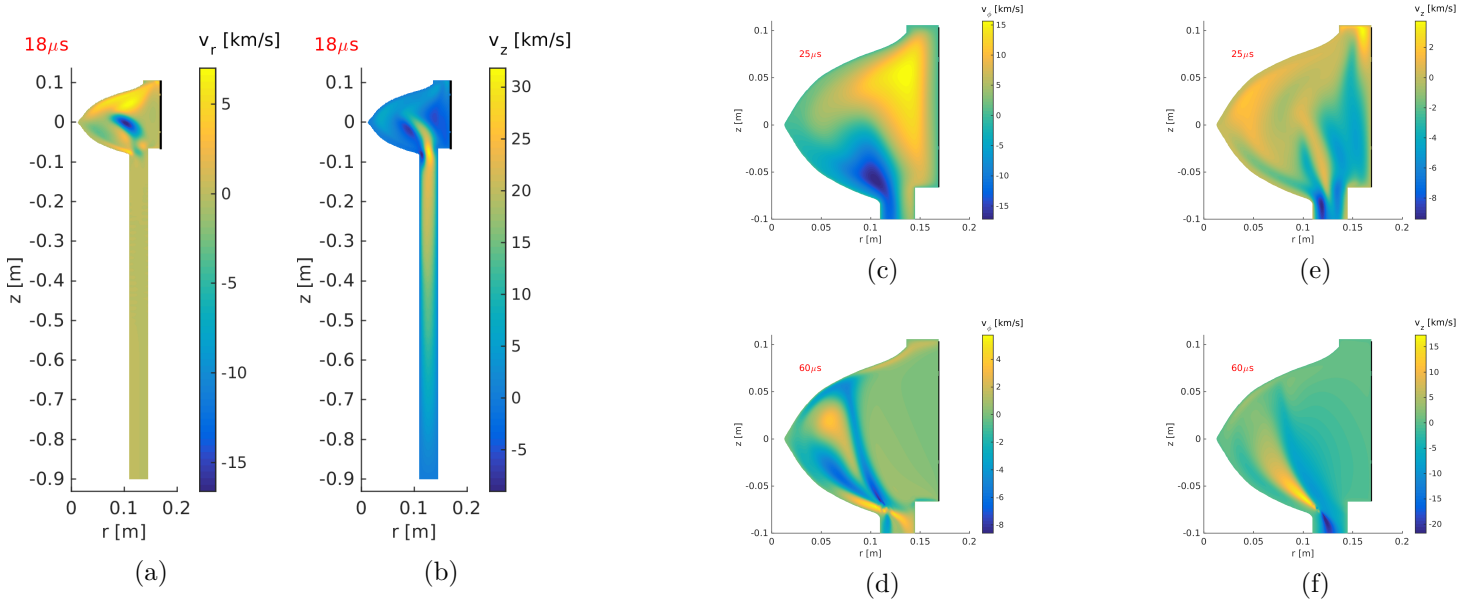

Figure 19: Velocity component profiles: radial velocity component at 18μs (a), azimuthal velocity component at 25μs (c) and 60μs (d), axial velocity component at 18μs (b), 25μs (e), and 60μs (f)

Profiles of v_r and v_z at 18μs are indicated in figure 19(a) and (b). The dynamics are complicated, but some key features can be noted. Velocities, in particular v_z, are especially high around this time during the

CT formation process, and lead to enhanced ion viscous heating (cf figure 17(c)). Pre-compression profiles of v_ϕ and v_z are shown at 25µs in figures 19(c) and (e). The particularly high downward-directed axial velocity near the entrance to the CT containment region at 25µs in figure 19(e) is related to jets of plasma fluid associated with magnetic reconnection during the formation of closed CT flux surfaces. Velocities are gradually dissipated by viscous effects until $t_{comp} = 45$µs, when magnetic compression is initiated and velocities rise sharply in reaction to the various dynamics associated with compression. The structures in the profiles of v_ϕ and v_z near the entrance to the CT containment region at 60µs (figures 19(d) and (f)), just after halfway through the main compression cycle, are related to jets of plasma fluid associated with magnetic reconnection when open poloidal field lines surrounding the CT are pinched off.

6.1 Comparison of simulated and experimental diagnostics

Note that in figures 20 to 22, the experimental diagnostics presented are from a simulation with the same code input parameters as those specified above, with the exception that $V_{comp} = 12$kV instead of 18kV.
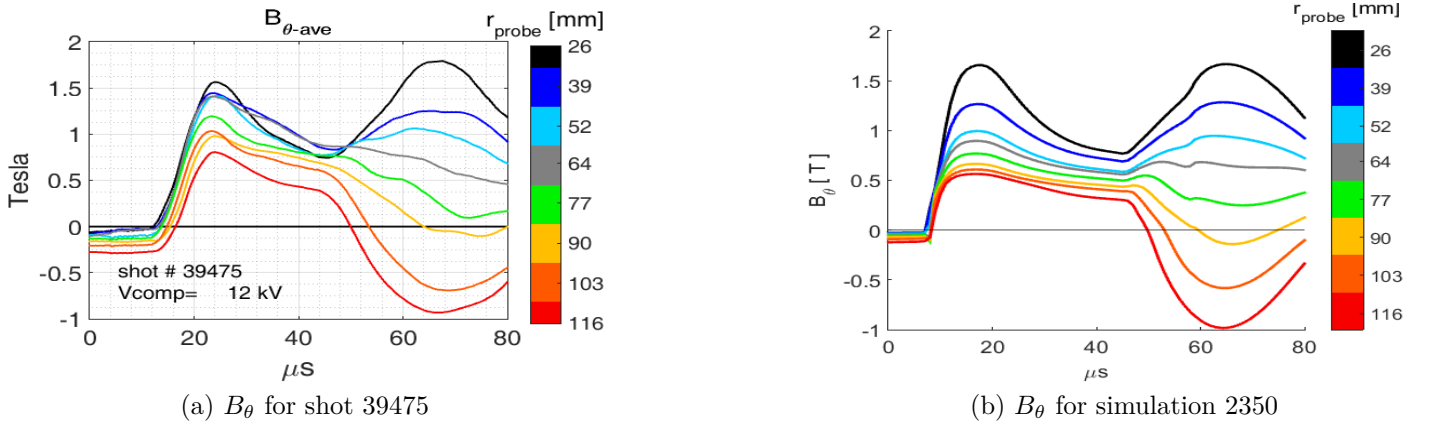

(a) B_θ for shot 39475

(b) B_θ for simulation 2350

Figure 20: Comparison of measured (a) and simulated (b) poloidal magnetic field at magnetic probe locations (V_{comp} =12kV, 11-coil configuration). Poloidal magnetic field signals are colored by the radial coordinates of the probe locations. The magnetic probe locations are indicated in figure 10(c).

A comparison of experimentally measured and simulated B_θ is shown in figure 20. For this shot (and simulation), $V_{comp} = 12$kV and $t_{comp} = 45$µs. Note that in the experiment, multiple magnetic probes were located at the same radial coordinate but at different toroidal angles. For ease of comparison, the magnetic field traces experimentally measured at the same probe radii are averaged in figure 20(a). The locations of the magnetic probes (which record poloidal as well as toroidal field) are indicated in figure 10(c). Note that measured B_θ is the field component parallel to the surface of the inner flux conserver in the poloidal plane. Simulated poloidal field is calculated at the boundary nodes by calculating t_r and t_z, the r and z components of the unit tangents to the computational domain at the boundary nodes, and using the equation

$$(B_\theta)_{bn} = \left(\hat{\mathbf{t}} \cdot \mathbf{B}_\theta \right)_{bn} = (t_r B_r + t_z B_z)_{bn}$$

Here, the subscript bn denotes a particular boundary node. The method using unit tangents allows for consistent evaluation of the sign of the poloidal field, which varies across the separatrix between the CT and levitation/compression field. Referring to figure 20(a), for shot 39475, $t_{lev} = -50$µs, so with a current rise time of ~ 40µs in the levitation coils, the poloidal levitation field measured at the probes reaches its maximum negative value at $t = \sim -10$µs. Formation capacitors are fired at $t = 0$µs and it takes ~ 15µs for the gun (stuffing) flux to be advected up to the probe locations. Until this time the poloidal field measured

at the probes is purely the levitation field. When the magnetised plasma bubbles into the CT confinement region, it displaces the levitation field, and the polarity of the measured field reverses - the stuffing field has opposite polarity to the levitation field, *i.e.*, the toroidal currents in the main solenoidal coil and the levitation coils are in opposite directions. Over the next several tens of µs, during and after reconnection of poloidal field to form closed flux surfaces, the CT resistively decays and undergoes Taylor relaxation during which part of the poloidal flux is converted to toroidal flux. Note that when levitation or compression field is being measured at the probes, $|B_\theta|$ is larger at the outer probes, due to the $1/(r_{coil} - r_{probe})$ scaling of levitation (compression) field with levitation (compression) current in the external coils. On the other hand, when CT field is being measured at the probes, B_θ is larger at the inner probes, due to the $1/r_{probe}^2$ scaling of CT field with CT flux - poloidal field lines are bunched together progressively more at smaller radii. The compression capacitors are fired at $t = t_{comp} = 45$µs, and the total compression current in the external coils rises over ~ 20µs to its peak, for $V_{comp} = 12$kV, of around 850kA, so that the total combined levitation and compression current is around 1MA at the time peak compression, around 65µs. In this shot, the CT is compressed inwards beyond the probes at $r = 90$mm, so B_θ at the probes located at $r \geq 90$mm (*i.e.*, light orange, dark orange, and red traces) is, starting at various times after 45µs, a measurement of the compression field, while the CT poloidal field is measured at the probes with radial coordinates $r < 90$mm. The CT remains stable during compression in this shot, and it expands approximately to its pre-compression state (apart from resistive flux losses and thermal losses) between $t \sim 65$µs and $t \sim 87$µs, when the compression current falls to zero and changes direction. Referring to figure 20(b), axisymmetric MHD simulations allow for only resistive loss of flux and do not capture the mechanisms, discussed in [11, 12], that led to poloidal flux loss in many compression shots. Shot 39475 was a flux-conserving shot, and a reasonable match is found between experimentally inferred and MHD-simulated poloidal field.
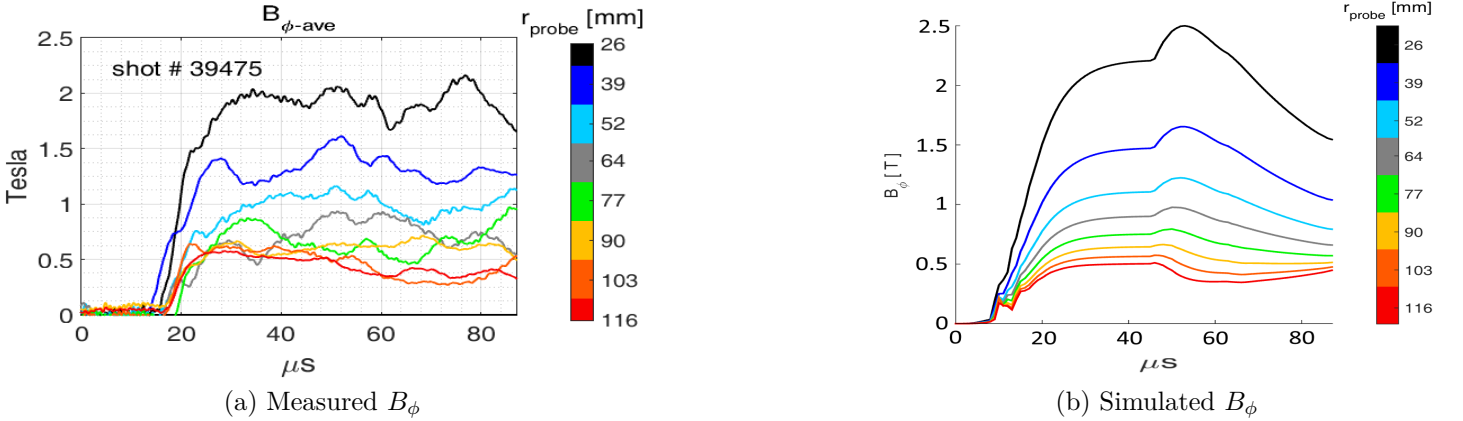

(a) Measured B_ϕ (b) Simulated B_ϕ

Figure 21: Comparison of measured (a) and simulated (b) toroidal magnetic field at magnetic probe locations (V_{comp} =12kV, 11-coil configuration)

Experimentally measured B_ϕ for shot 39475 is shown in figure 21(a). As discussed in [11, 12], B_ϕ at the magnetic probes rises at compression as crow-barred shaft current flowing in conductors (*i.e.*, machine components as well as ambient plasma) surrounding the CT increases when it is able to divert from the aluminum bars outside the insulating wall to a lower inductance path through ambient plasma located outboard of the CT. Due to an instability (thought to be an external kink) that was routinely observed at compression, the current diversion, and hence toroidal magnetic field measured at probes located at the same radii and different toroidal angles, is generally toroidally asymmetric. Measured toroidal field is generally observed to increase over compression at probes located inside the CT boundary, and decrease at probes located outside the boundary; the CT outer boundary is also toroidally asymmetric at compression. The toroidal magnetic field traces experimentally measured at the same radii at different toroidal angles have been averaged in figure 21(a). The asymmetric MHD code cannot capture the inherently 3D instability. However, referring to figure 21(b), toroidal field increases more at compression at the inner probes and

decreases at the outer probes at $r \geq 90$mm, as shaft current is diverted to a path inside the locations of the outer probes, which is also qualitatively evident from the toroidal-averages of the measured toroidal field. Simulated diversion of shaft current to a path through ambient plasma located outboard of the CT is apparent from contours of f at 65μs, see figure 14(d).

(a) Simulated and measured n_e

(b) Simulated and measured T_i

Figure 22: Comparison of measured and simulated line-averaged electron density (a) and line-averaged ion temperature (b) ($V_{comp} = 12$kV, 11-coil configuration)

The comparison between experimentally measured and simulated electron density and ion temperature for shot 39475 is indicated in figures 22(a) and 22(b). The simulated line-averaged electron density along the interferometer chord at $r = 35$mm (see figure 15) hasn't been included in figure 22(a) because the experimental data for that chord is not available. The experimentally measured electron densities are line-averaged quantities obtained with He-Ne laser interferometers looking down the vertical chords at $r = 65$mm and $r = 95$mm that are indicated in figure 15. The time it takes for plasma to be advected up the gun and enter the CT containment region is underestimated by ~ 5μs in this simulation. The density magnitude during CT decay and magnetic compression is approximately reproduced. Referring to figure 22(b), the experimentally measured ion temperatures were evaluated from Doppler broadening of line radiation from singly ionized Helium (He II line at 468.5nm) along the chords indicated in figure 17. Note that the diagonal green coloured chord indicated in figure 17 has its lower point at $r = 70$mm. Simulated line-averaged ion temperature is evaluated along the same chords, producing a reasonable match to the experimental data. For this shot (and simulation), with $V_{comp} = 12$kV, an increase in ion temperature by a factor of over two, from ~ 25eV to ~ 60eV, is indicated in the region of the ion Doppler chords. As outlined in [11, 12], a maximum error in the temperature measurement due to density broadening has been evaluated as $\sim$10eV for density levels associated with shot 39475 at peak compression. Careful analysis was undertaken to confirm that temperature broadening rather than density broadening was the dominant broadening mechanism.

6.2 Simulated plasma-wall interaction

(a) 6-coil configuration   (b) 11-coil configuration

Figure 23: Simulated plasma-wall interaction. Note how poloidal field penetrates the insulating wall during the bubble-in process in the six coil configuration.

As described in [11, 12], levitated CT lifetime and temperature was increased significantly when the original configuration consisting of six levitation/compression coils was replaced with an eleven coil configuration. It is believed that the improvement is related to reduced levels of levitation field displacement and interaction between the plasma and insulating wall during the CT formation process, leading to consequent reductions in sputtering, plasma impurity concentration, and radiative cooling. Spectrometer data indicated a four-fold reduction in total spectral power with the 11-coil configuration, even at increased formation power, confirming that the 11-coil configuration led to reduced impurity concentration. The inclusion of a model for an insulating region representing the wall and air located between the vacuum chamber, in which MHD dynamics are evolved, and the stack of external levitation/compression coils, enables simulations to provide further verification of the proposed explanation for the observed improvement. MHD simulations confirm the reduction of plasma-wall interaction with the eleven coil configuration, as shown in figure 23. In figure 23(a), the stack of six coils is partly located in the blank rectangle on the right, centered around $z = 0$cm, and extends off further to the right (not shown). The region above, below, and just to the left of the coil-stack represents the air around the stack, while the area to the right of the vertical black line at $r = 17$cm represents insulating material. The vertical black line represents the inner radius of the insulating wall, and the outer radius of the insulating wall at $r = 17.7$cm is not indicated. In figure 23(b), the stack of eleven coils extends all the way from the top to the bottom of the insulating wall, the inner radius of the coil stack is the same as that for the six coil stack. In both cases, only ψ, which determines the vacuum poloidal field, is evaluated in the insulating region to the right of the inner radius of the insulating wall. The solution for ψ is coupled to the full MHD solution in the remainder of the domain, as described in section 5.2. To maintain toroidal flux conservation, boundary conditions for f, which has a finite constant value in the insulating wall and is zero outside the current-carrying aluminum bars depicted in figure 8(b), are evaluated for, and applied to, the part of the boundary representing the inner radius of the insulating wall, as described in section 5.4. Both simulations have boundary conditions for ψ_{main} and ψ_{lev} from FEMM models, pertaining to $I_{main} = 70$A, and with the total levitation current such that ψ_{lev} is approximately the same for each configuration. Also, code input V_{form} is set to 16kV for both simulations. Figure 23(a) indicates how poloidal field penetrates the insulating wall during the bubble-in process in the six coil configuration. In practice, ions streaming along and gyro-rotating around the field lines would then sputter insulating material into the plasma, leading to impurity radiation and radiative cooling, with consequent increased resistivity and reduced CT magnetic lifetimes.

6.3 Compression field reversal

When the compression current in the coils changes direction (see figure 9(b)), the CT poloidal field magnetically reconnects with the compression field, and a new CT with polarity opposite to that of the previous CT is induced in the containment region, compressed, and then allowed to expand. The process repeats itself at each change in polarity of the compression current until either the plasma loses too much heat, or the compression current is sufficiently damped.
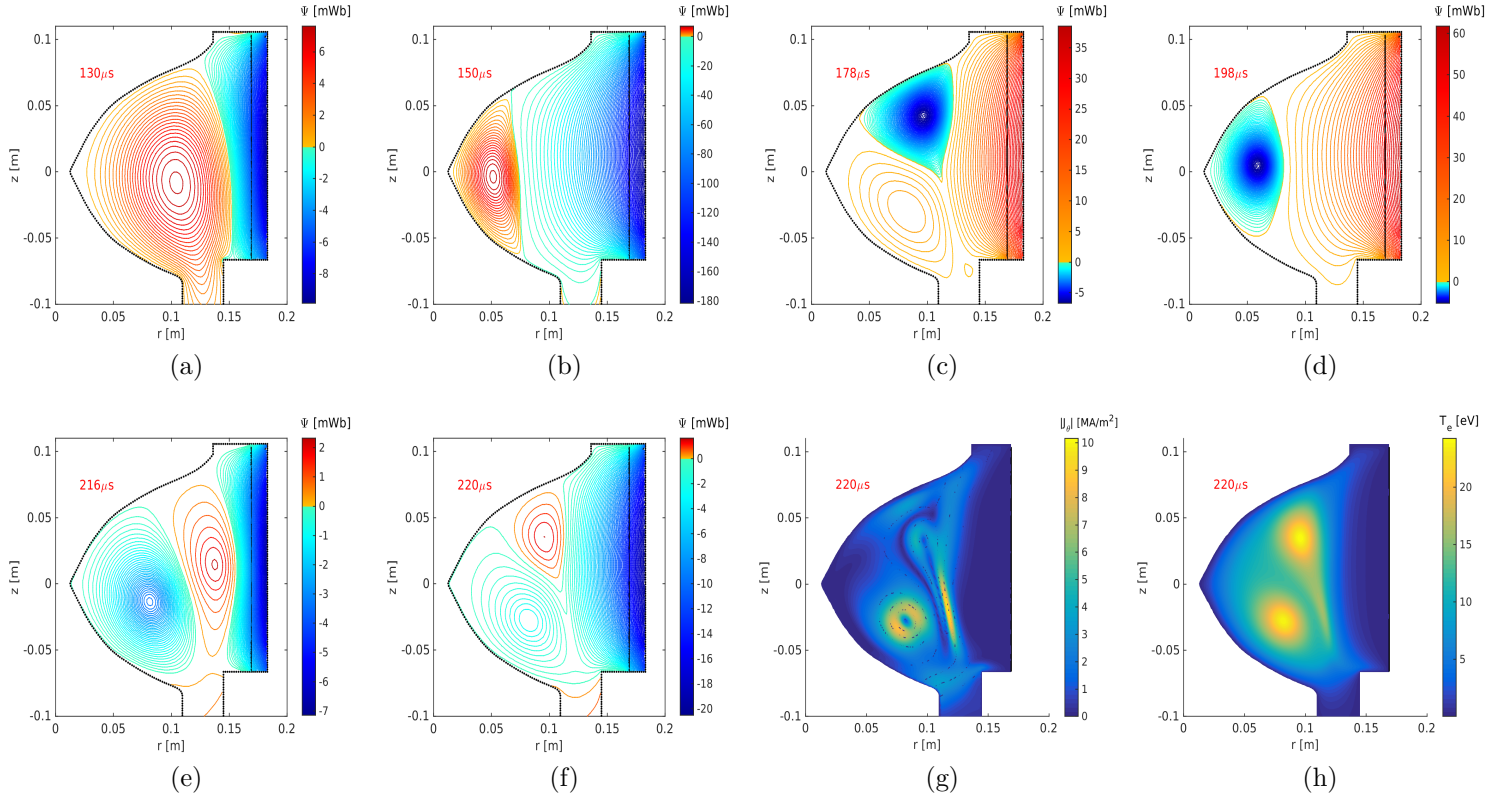

Figure 24: Poloidal flux contours at 130μs (a), 150μs (b), 178μs (c), 198μs (d), 216μs (e), 220μs (f), and profiles of poloidal current density (g) and electron temperature (h) at 220μs, for an MHD simulation with compression current reversal

Figures 24(a) to (f) show ψ contours at various times for a simulation similar to that presented in figures 13 to 19, with the exception that $t_{comp} = 130$μs instead of 45μs. Peak compression is at 150μs (figure 24(b)). By 178μs, the external compression field has changed polarity and starts to reconnect with the CT poloidal field. Toroidal currents are induced to flow in the ambient plasma initially located outboard of the original CT, enabling the formation of a new CT (blue closed contours) with polarity opposite to that of the original CT (figure 24(c)). The new induced CT is magnetically compressed inwards by the increasing reversed polarity compression field, with peak compression at around 198μs (figure 24(d)). The compression field polarity rings back to its original state by 216μs, when a third CT is induced, with the same polarity as the original CT (figure 24(e)). By 220μs, the poloidal field of the second CT is reconnecting with the compression field, and the third CT is being compressed inwards (figure 24(f)). Electron temperature and poloidal current density at 220μs for the two co-existing CTs is presented in 24(g) and (h). Simulated magnetic field measurements from this simulation are presented and compared with relevant experimental measurements in figure 25.
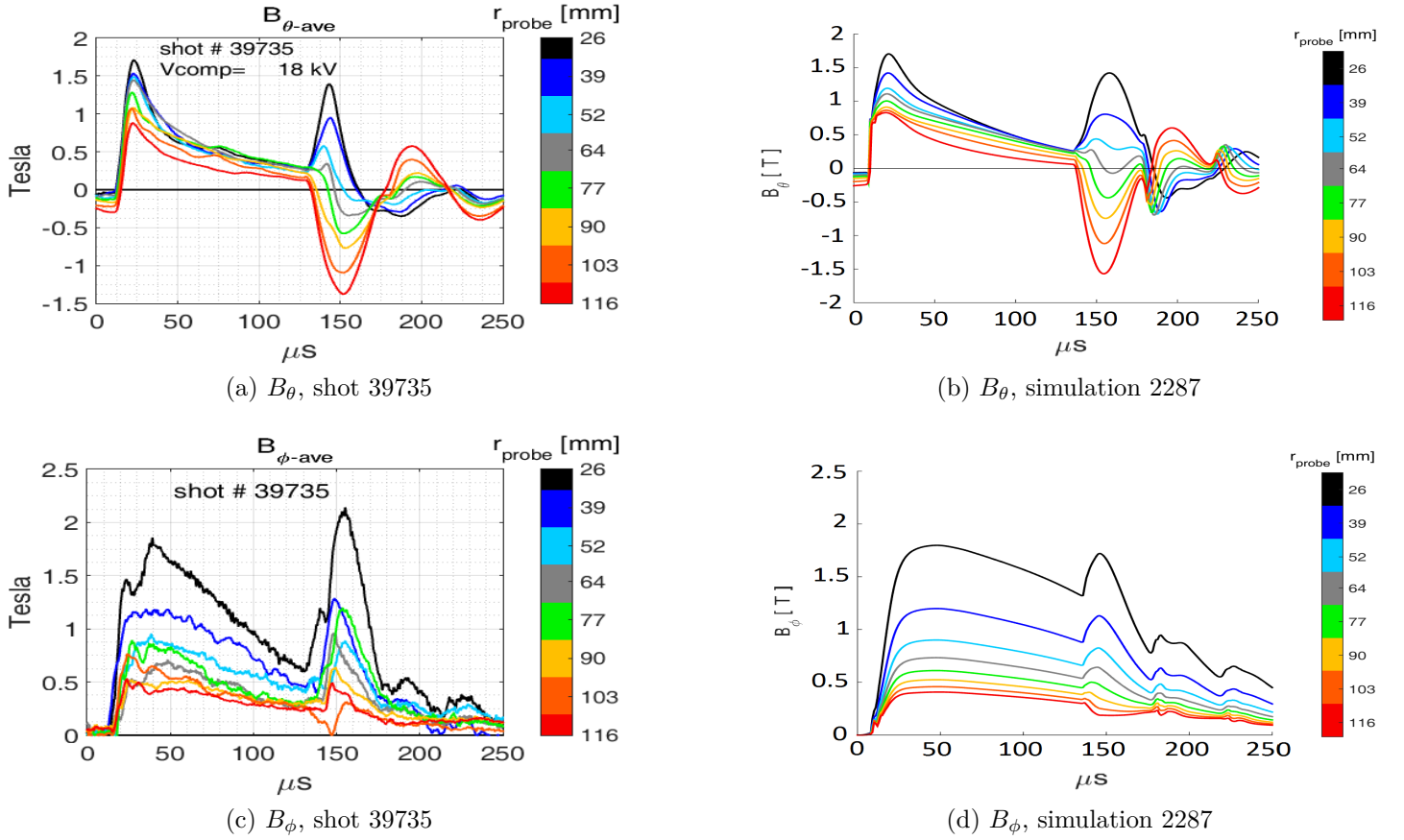
(a) B_θ, shot 39735

(b) B_θ, simulation 2287

(c) B_ϕ, shot 39735

(d) B_ϕ, simulation 2287

Figure 25: Comparison of measured and simulated poloidal and toroidal magnetic field at magnetic probe locations (V_{comp} = 18kV, 11-coil configuration)

The comparison between experimentally measured and simulated poloidal and toroidal field, when the compression current reversals are included, is shown in figure 25. The experimental magnetic field measurements have been toroidally averaged for clarity. Shot 39735 presented here had V_{comp} = 18kV and t_{comp} = 130µs. In shot 39735, the poloidal field measured at the inner probes collapses at $\sim$ 145µs (figure 25(a)) , while the compression coil current peaks at $\sim$ 150µs, implying (as presented in detail in [11, 12]) that poloidal flux was not well conserved during compression. Apart from resistive losses, CT poloidal flux is conserved in the simulation, so the poloidal field at the inner probes (figure 25(b)) continues to rise until the compression coil current peaks.

As discussed in previously reference to figure 21, the compressional instability lead to toroidal field measurements that are toroidally very asymmetric, and the axisymmetric MHD model cannot reproduce this. Comparison of figures 25(c) and (d) shows how the simulated B_ϕ does, in general, rise at the magnetic probes as crowbarred shaft current increases when it is diverted to a lower inductance path. There is a qualitative agreement between the simulated B_ϕ and the toroidal-averages of the measured B_ϕ.

7   Conclusion

It has been shown how various differential operators with useful mimetic properties have been developed, and used to ensure conservation of total energy, particle count, toroidal flux, and (in some scenarios) total angular momentum in an axisymmetric linear finite element numerical scheme that implements the non-linear single fluid, two temperature MHD equations. The principal mimetic qualities of the operators are that they satisfy discrete forms of the differential product rule and the divergence theorem. A novelty of

the code is that all discrete spatial differential operators are represented as matrices, and the discretized forms of continuous differential equations may be obtained by simply replacing the original continuous differentiations with the corresponding matrix operators. The resultant DELiTE framework may be applied to solve a wide range of systems of differential equations, and may serve as an educational tool. The methods developed for simulating CT formation, magnetic levitation and magnetic compression to study a novel experiment have been outlined. Special care has been taken to simulate the poloidal vacuum field in the insulating region between the inner radius of the insulating tube and the levitation/compression coils, and to couple this solution to the evaluation of ψ in the plasma domain, while maintaining toroidal flux conservation, enabling a quantitative model of plasma/wall interaction in various coil configurations. In general, a reasonable match is obtained between simulated and experimental diagnostics.

Weak points of the code include the first order accuracy associated with the linear scheme, and the explicit timestepping scheme, which limits the range of allowable values for the various diffusion coefficients. The diffusive nature of the code is associated with requirements for numerical stability. Presently, angular momentum is conserved only in particular simulation scenarios.

Further code development may include a more generally applicable model for density diffusion with correction terms that maintain angular momentum conservation even in simulation scenarios that include CT formation and magnetic compression. The level to which artificial density diffusion affects the simulated density diagnostic, and the evolution of the other fields, should be investigated further. An implicit timestepping scheme may be implemented as this would enable faster simulation times while enabling the use of a greater range of values for the various diffusion coefficients.

The ability to model part of the domain as a plasma-free material is useful because it expands the code's range of applicability as a problem-solving tool. For example, the feature can easily be adapted to model the penetration of field associated with magnetically confined plasma into surrounding conductors. The effort invested in developing a conservative scheme with many extended features has resulted in a code framework with a solid foundation for further development and improvement. For example, as described in [22], a model of plasma/neutral particle interaction was developed and included in the DELiTE framework, enabling reproduction of the effect observed on another experiment, the General Fusion SPECTOR machine, of neutral gas diffusing up the Marshall gun, leading to markedly increased CT electron density well after completion of the CT formation process.

8   Acknowledgments

A Appendix A

Detailed derivation of the first order node-to-element differential operator

In the following, the element-specific node indexes i, j, k will be replaced with the indexes 1, 2 and 3 for simplicity. From equation 2.2, the radial and axial first spatial derivatives of $U^e(\mathbf{r})$ are constants across the element e, and are given by $\frac{\partial U^e}{\partial r} = B^e$, and $\frac{\partial U^e}{\partial z} = C^e$. Expressions for B^e and C^e are found using equation 2.13:

$$U_1^e - U_3^e = B^e(r_1 - r_3) + C^e(z_1 - z_3)$$
$$U_2^e - U_3^e = B^e(r_2 - r_3) + C^e(z_2 - z_3)$$

$$\Rightarrow B^e = \frac{\partial U^e}{\partial r} = \frac{U_1^e(z_2 - z_3) + U_2^e(z_3 - z_1) + U_3^e(z_1 - z_2)}{2s^e}$$
$$C^e = \frac{\partial U^e}{\partial z} = \frac{U_1^e(r_2 - r_3) + U_2^e(r_3 - r_1) + U_3^e(r_1 - r_2)}{-2s^e} \tag{A.1}$$

The triangle area s^e is introduced here, assuming that vertices are numbered counterclockwise, noting that $2s^e = |\mathbb{R}^e|$, where $|\mathbb{R}^e|$ is the determinant of array $\mathbb{R}^e = \begin{pmatrix} 1 & r_1 & z_1 \\ 1 & r_2 & z_2 \\ 1 & r_3 & z_3 \end{pmatrix}$, so that

$$2s^e = (r_1 - r_3)(z_2 - z_3) - (r_2 - r_3)(z_1 - z_3)$$

The element-specific spatial derivatives can also be expressed in terms of the coefficients in the element-specific pyramid-side functions ψ_1^e, ψ_2^e, and ψ_3^e. As noted earlier, each pyramid-side function is specific to a particular node, and to a particular element, and is defined as $\psi_n^e(\mathbf{r}) = a_n^e + b_n^e r + c_n^e z$, and has the property $\psi_n^e(r_j, z_j) = \delta_{nj}$. This yields, for each element e, the identity $\mathbb{R}^e * \mathbb{C}^e = \mathbb{I}$, or

$$\begin{pmatrix} 1 & r_1 & z_1 \\ 1 & r_2 & z_2 \\ 1 & r_3 & z_3 \end{pmatrix} * \begin{pmatrix} a_1^e & a_2^e & a_3^e \\ b_1^e & b_2^e & b_3^e \\ c_1^e & c_2^e & c_3^e \end{pmatrix} = \begin{pmatrix} 1 & 0 & 0 \\ 0 & 1 & 0 \\ 0 & 0 & 1 \end{pmatrix}$$

$$\Rightarrow \mathbb{C}^e = (\mathbb{R}^e)^{-1} = \frac{1}{2s^e} \begin{pmatrix} (r_2 z_3 - r_3 z_2) & (r_3 z_1 - r_1 z_3) & (r_1 z_2 - r_2 z_1) \\ (z_2 - z_3) & (z_3 - z_1) & (z_1 - z_2) \\ (r_3 - r_2) & (r_1 - r_3) & (r_2 - r_1) \end{pmatrix} \tag{A.2}$$

Comparing equations A.1 with equation A.2, it is evident that

$$\frac{\partial U^e}{\partial r} = \sum_\varepsilon U_\varepsilon^e b_\varepsilon^e$$
$$\frac{\partial U^e}{\partial z} = \sum_\varepsilon U_\varepsilon^e c_\varepsilon^e \tag{A.3}$$

Given the values of the approximation for the piecewise linear function $U(\mathbf{r})$ on the triangle vertices, and the element-specific array $\mathbb{C}^e$ evaluated using equation A.2, equations A.3 can be used to determine the values of the spatial derivatives of $U(\mathbf{r})$ at the interior of each element.

B   Appendix B

Node-to-element operator identities

We demonstrate here a property of the node-to-element operators that is used to demonstrate angular momentum conservation in section 3.3.3. For any continuous scalar functions f and g, the identity (Stoke's theorem) holds that

$$\int (\nabla f \times \nabla g) \cdot d\mathbf{S} = \int \nabla \times (f \nabla g) \cdot d\mathbf{S} = \int f \nabla g \cdot d\mathbf{l} \tag{B.1}$$

With azimuthal symmetry, $\int (\nabla f \times \nabla g) \cdot d\mathbf{S} = \int (f'_z g'_r - f'_r g'_z) \, \widehat{\boldsymbol{\phi}} \cdot d\mathbf{S} = \int (f'_z g'_r - f'_r g'_z) \, ds_\phi$, where ds_ϕ is an elemental area in the poloidal $(r - z)$ plane and $\widehat{\boldsymbol{\phi}}$ is the unit vector in the azimuthal direction. Hence, the discrete form of $\int (\nabla f \times \nabla g) \cdot d\mathbf{S}$, using the node-to-element differential operators, is

$$
\begin{aligned}
\left(\int (\nabla f \times \nabla g) \cdot d\mathbf{S} \right)_{disc.} &= \widehat{s}^T * \left(\left(\overline{\widehat{Dz}} * \overline{f} \right) \left(\overline{\widehat{Dr}} * \overline{g} \right) - \left(\overline{\widehat{Dr}} * \overline{f} \right) \left(\overline{\widehat{Dz}} * \overline{g} \right) \right) \\
&= \left(\overline{\widehat{Dz}} * \overline{f} \right)^T * \widehat{\widehat{S}} * \left(\overline{\widehat{Dr}} * \overline{g} \right) - \left(\overline{\widehat{Dr}} * \overline{f} \right)^T * \widehat{\widehat{S}} * \left(\overline{\widehat{Dz}} * \overline{g} \right) \\
&= \overline{f}^T * \overline{\widehat{Dz}}^T * \widehat{\widehat{S}} * \overline{\widehat{Dr}} * \overline{g} - \overline{f}^T * \overline{\widehat{Dr}}^T * \widehat{\widehat{S}} * \overline{\widehat{Dz}} * \overline{g} \\
&= \overline{f}^T * \left(\overline{\widehat{Dz}}^T * \widehat{\widehat{S}} * \overline{\widehat{Dr}} - \overline{\widehat{Dr}}^T * \widehat{\widehat{S}} * \overline{\widehat{Dz}} \right) * \overline{g} \\
&= \overline{f}^T * \left(\overline{\overline{B}}^T - \overline{\overline{B}} \right) * \overline{g} \\
&= \overline{f}^T * \overline{\overline{A}} * \overline{g} \tag{B.2}
\end{aligned}
$$

where $\overline{\overline{B}} = \overline{\widehat{Dr}}^T * \widehat{\widehat{S}} * \overline{\widehat{Dz}}$. Setting $\overline{f} = \overline{\phi}_m$ and $\overline{g} = \overline{\phi}_n$, where $\overline{\phi}_m$ and $\overline{\phi}_n$ are the vectors defining the nodal values of basis functions ϕ_m and ϕ_n respectively (*i.e.*, $\overline{\phi}_m(k) = \delta_{mk}$ and $\overline{\phi}_n(k) = \delta_{nk}$), equations B.2 and B.1 imply that

$$A_{mn} \equiv A(m, n) = \overline{\phi}_m^T * \overline{\overline{A}} * \overline{\phi}_n = \int \phi_m \nabla \phi_n \cdot d\mathbf{l} \tag{B.3}$$

We will show that each element of $\overline{\overline{A}}$ is zero at internal nodes, *i.e.*, $\left(\overline{\overline{A}} \right)_{int} = 0$. There are four cases to consider: (1) $m \neq n$ and nodes m and n are not adjacent, (2) $m = n$, (3) m and n are the indexes of adjacent internal nodes, and (4) m and n are the indexes of adjacent nodes located on the boundary of the computational domain. In case (1), A_{mn} is obviously zero. In case (2), $A_{mn} = \overline{\phi}_m^T * \left(\overline{\overline{B}}^T - \overline{\overline{B}} \right) * \overline{\phi}_m = \overline{\phi}_m^T * \overline{\overline{B}}^T * \overline{\phi}_m - \overline{\phi}_m^T * \overline{\overline{B}} * \overline{\phi}_m$. The first term scalar term here can be transposed, so that $A_{mn} = 0$ in case (2).
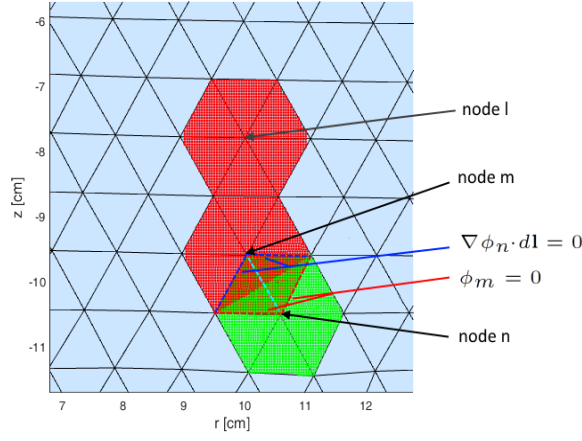
Figure 26: Linear basis function depiction for triangular elements (top view). Note the dark blue dashed lines represent the part of the boundary of basis function ϕ_n that overlaps with ϕ_m, and the red dashed lines represent the part of the boundary of ϕ_m that overlaps with ϕ_n.

Figure 26 is a top-view of figure 1. Referring to equation B.3 and to figure 26, the only contribution to A_{mn} in case (3) is from the contour integral $\int \phi_m \nabla \phi_n \cdot d\mathbf{l}$ along the boundary (depicted with dark blue and red dashed lines) of the diamond-shape representing the overlapping area of the basis functions ϕ_m and ϕ_n. It can be seen that $\phi_m = 0$ along part of the contour, and $\nabla \phi_n \cdot d\mathbf{l} = 0$ along the remaining parts, so that $A_{mn} = 0$ in case (3). In case (4), when m and n are the indexes of adjacent nodes located on the boundary of the computational domain, the integral $\int \phi_m \nabla \phi_n \cdot d\mathbf{l}$ would be finite along the light blue dashed line connecting nodes m and n (in case (4), the light blue dashed line would represent part of the computational domain boundary). Therefore, A_{mn} is finite only when m and n are the indexes of adjacent nodes located on the boundary of the computational domain, leading to the identity

$$\left(\overline{\overline{Dz}}^T * \widehat{\overline{\overline{S}}} * \overline{\overline{Dr}} - \overline{\overline{Dr}}^T * \widehat{\overline{\overline{S}}} * \overline{\overline{Dz}} \right)_{int} = 0 \tag{B.4}$$

C   Appendix C

Node-to-node operator identities

Now we introduce some special mimetic properties of the node-to-node differential operators. $U_r'(\mathbf{r})$, the radial spatial derivative of the approximate solution $U(\mathbf{r})$, can alternatively be expressed, using the basis function expansion (equation 2.3), as

$$U_r'(\mathbf{r}) = \sum_{n=1}^{N_n} U_n \, \phi_{rn}'(\mathbf{r}) \tag{C.1}$$

Applying the Galerkin method, we obtain

$$\int \phi_j \, U_r'(\mathbf{r}) \, dr \, dz = \sum_{n=1}^{N_n} U_n \int \phi_j \, \phi_{rn}' \, dr \, dz \tag{C.2}$$

Again, from equation 2.6, the left side of this equation is $U_{rj}' \, s_j / 3$. On the right side, matrix $\overline{\overline{Lr}}$ of size $N_n \times N_n$ is introduced as

$$\frac{1}{3} \overline{\overline{Lr}}(j, \, n) = \int \phi_j \, \phi_{rn}' \, dr \, dz \tag{C.3}$$

47

Hence, equation C.2 can be re-expressed as

$$\overline{U}'_r(j)\,\overline{s}(j) = \sum_{n=1}^{N_n} \left(\overline{\overline{Lr}}(j,\,n)\,\overline{U}(n)\right) \tag{C.4}$$

or in matrix form: $\overline{\overline{S}} * \overline{\overline{Dr}} * \overline{U} = \overline{\overline{Lr}} * \overline{U}$

$$\Rightarrow \overline{\overline{Dr}} = \overline{\overline{S}}^{-1} * \overline{\overline{Lr}} \tag{C.5}$$

With integration by parts and Green's theorem, equation C.3 implies that

$$\overline{\overline{Lr}}(j,\,n) = 3\int \phi_j\,\phi'_{rn}\,dr\,dz$$

$$= 3\int \left(-\phi'_{rj}\phi_n + (\phi_j\,\phi_n)'_r\right)\,dr\,dz$$

$$= 3\left(-\int \phi_n\,\phi'_{rj}\,dr\,dz + \oint \phi_j\,\phi_n\,dz\right)$$

The boundary term vanishes at internal nodes, so that $\overline{\overline{Lr}}(j,\,n) = -\overline{\overline{Lr}}(n,\,j)$ at the internal nodes. This implies that all elements of the matrix $\overline{\overline{Lr}} + \overline{\overline{Lr}}^T$ are equal to zero, except for the elements corresponding to boundary nodes. Hence, using equation C.5, and noting that the transpose of a diagonal matrix is the same matrix, we obtain

$$\left(\overline{\overline{S}} * \overline{\overline{Dr}} + \overline{\overline{Dr}}^T * \overline{\overline{S}}\right)_{int} = 0 \tag{C.6}$$

where the subscript int denotes all elements of the matrix that correspond to interior (non-boundary) nodes. There is an analogous identity for the $\overline{\overline{Dz}}$ operator:

$$\left(\overline{\overline{S}} * \overline{\overline{Dz}} + \overline{\overline{Dz}}^T * \overline{\overline{S}}\right)_{int} = 0 \tag{C.7}$$

As a consequence of these identities, the node-to-node differential operators have some important properties that mimic properties of the corresponding continuous operators. In particular, the discrete expression for the volume integral in equation 1.1 is

$$\overline{dV}^T * \left[\overline{U}\,\left(\overline{\overline{\nabla}}\cdot\mathbf{P}\right) + \mathbf{P}\cdot\left(\overline{\overline{\nabla}}\,\overline{U}\right)\right]$$

$$= \overline{dV}^T * \left[\overline{U}\,\left(\overline{\overline{Dr}} * \left(\overline{r}\,P_r\right) + \overline{\overline{Dz}} * \left(\overline{r}\,P_z\right)\right)/\overline{r} + P_r\,\left(\overline{\overline{Dr}} * \overline{U}\right) + P_z\,\left(\overline{\overline{Dz}} * \overline{U}\right)\right]$$

$$= \frac{2\pi}{3}\left[\overline{U}^T * \overline{\overline{S}} * \left(\overline{\overline{Dr}} * \overline{\overline{R}} * P_r + \overline{\overline{Dz}} * \overline{\overline{R}} * P_z\right) + \overline{P_r}^T * \overline{\overline{S}} * \overline{\overline{R}} * \overline{\overline{Dr}} * \overline{U} + \overline{P_z}^T * \overline{\overline{S}} * \overline{\overline{R}} * \overline{\overline{Dz}} * \overline{U}\right]$$

$$= \frac{2\pi}{3}\,\overline{U}^T * \left[\left(\overline{\overline{S}} * \overline{\overline{Dr}} + \overline{\overline{Dr}}^T * \overline{\overline{S}}\right) * \overline{\overline{R}} * P_r + \left(\overline{\overline{S}} * \overline{\overline{Dz}} + \overline{\overline{Dz}}^T * \overline{\overline{S}}\right) * \overline{\overline{R}} * P_z\right]$$

Note that in the last step, transpose operations on the scalar expressions have been performed. Hence, due to equations C.6 and C.7

$$\overline{dV}^T * \left[\left(\overline{U}\,\left(\overline{\overline{\nabla}}\cdot\mathbf{P}\right) + \left(\overline{\overline{\nabla}}\,\overline{U}\right)\cdot\mathbf{P}\right)\right] = 0 \qquad\qquad \left(\text{if } \overline{U}\,|_\Gamma = 0 \text{ or } \mathbf{P}_\perp|_\Gamma = 0\right) \tag{C.8}$$

For the particular case of $\overline{U} = \overline{1}$, this implies that

$$\overline{dV}^T * \left[\overline{\overline{\nabla}}\cdot\mathbf{P}\right] = \overline{0} \qquad\qquad \left(\text{if } \mathbf{P}_\perp|_\Gamma = 0\right) \tag{C.9}$$

D Appendix D

Maintenance of energy and momentum conservation with artificial density diffusion

The components of force per volume vector $\overline{\mathbf{f}}_\zeta = (\overline{f}_{\zeta r}, \overline{f}_{\zeta\phi}, \overline{f}_{\zeta z})^T$ in the velocity equations, and in the heating term $\overline{Q}_\zeta$ in the ion pressure equation (equation 3.16) are included to cancel the effect of artificial density diffusion on the total system momentum and energy, maintaining conservation. There are two models for the correction terms. The first model is straightforward and maintains conservation of energy and angular momentum when density diffusion is included in the mass continuity equation. It is evaluated simply by treating the density diffusion as a particle source and assessing the local (*i.e.*, nodal) correction terms as the local effects of the source on momentum and energy. However this model can lead locally to negative ion pressure if the density gradients are extreme, so it is not suitable for inclusion in simulations of CT formation and compression. The model works ok for other simulation types, for example the resistive decay of a magnetised plasma described by an equilibrium model. The second model is more complicated - it maintains conservation of volume integrated energy and can not cause negative ion pressure, but angular momentum conservation is not maintained. Both models for the correction terms compensate for additional r and z directed momentum introduced due to density diffusion - for the first model the compensation is local, while for the second model the compensation is in the volume integrated sense. The simulations presented in section 6 of this paper use the second model.

The correction terms for the first model are derived as follows. For convenience, we use the notation $\overline{\zeta}_n = \widehat{\overline{\nabla}} \cdot \left(\widehat{\zeta} \left(\widehat{\overline{\nabla}} \, \overline{n} \right) \right)$. Referring to equation 3.16, note that $\dot{\overline{n}}|_\zeta = \overline{\zeta}_n$, $\dot{\vec{v}}_\beta|_\zeta = \overline{f}_{\zeta\beta} / \overline{\rho}$, and $\dot{\overline{p}}_i|_\zeta = \overline{Q}_\zeta$ are the parts $\dot{\overline{n}}$, $\dot{\vec{v}}_\beta$, and $\dot{\overline{p}}_i$ respectively that are associated with density diffusion. The local rate of change of the β component (where, here, $\beta = r, z$) of momentum per unit volume due to the local particle source/sink terms arising due to density diffusion is set to zero by design, resulting in

$$\left(\frac{\partial}{\partial t} \left(m_i \, \overline{n} \, \overline{v}_\beta \right) \right)_\zeta = m_i \left(\overline{n} \, \overline{f}_{\zeta\beta} / \overline{\rho} + \overline{\zeta}_n \, \overline{v}_\beta \right) = 0$$

$$\Rightarrow \overline{f}_{\zeta\beta} = -m_i \, \overline{v}_\beta \, \overline{\zeta}_n$$

Naturally, for $\beta = \phi$, this expression for $\overline{f}_{\zeta\beta}$ also locally cancels additional angular momentum per unit volume introduced by density diffusion. The rate of change of energy per unit volume due to local particle source/sink terms associated with density diffusion is also set to zero:

$$\left(\frac{\partial}{\partial t} \left(\frac{1}{2} m_i \, \overline{n} \, \overline{v}^2 + \frac{1}{\gamma - 1} \dot{\overline{p}}_i \right) \right)_\zeta = \frac{1}{2} m_i \, \overline{\zeta}_n \, \overline{v}^2 + \sum_\beta \left(m_i \, \overline{n} \, \overline{v}_\beta \, \overline{f}_{\zeta\beta} / \overline{\rho} \right) + \overline{Q}_\zeta = 0$$

$$\Rightarrow \overline{Q}_\zeta = \frac{1}{2} m_i \, \overline{v}^2 \, \overline{\zeta}_n$$

Hence, the contributions to $\dot{U}_K$ and $\dot{U}_{Th}$ arising from the artificial density diffusion and relevant correction terms cancel by design as:

$$\left(\dot{U}_K + \dot{U}_{Th} \right)_\zeta = \overline{dV}^T * \left\{ m_i \left(\frac{1}{2} - 1 + \frac{1}{2} \right) \overline{v}^2 \, \overline{\zeta}_n \right\} = 0$$

However, note that if density gradients are extreme, $\overline{\zeta}_n$ and hence $\overline{Q}_\zeta$ will have some very large negative values, so that $\overline{p}_i$ can become negative.

For the second model of correction terms, $\overline{Q}_\zeta = \overline{0}$, and a suitable choice of $\overline{f}_{\zeta\beta}$ that ensures maintenance, in a volume integrated sense, of conservation of total energy, is

$$\overline{f}_{\zeta\beta} = \frac{1}{2}m_i\,\zeta\left[\widehat{\overline{W}} * \left(\left(\overline{\widehat{\overline{\nabla}}}\,\overline{n}\right)\cdot\left(\overline{\widehat{\overline{\nabla}}}\,\overline{v}_\beta\right)\right) + \widehat{\overline{\nabla}}\cdot\left(\widehat{v}_\beta\left(\overline{\widehat{\overline{\nabla}}}\,\overline{n}\right)\right) - \overline{v}_\beta\left(\overline{\overline{\Delta}}\,\overline{n}\right)\right] \tag{D.1}$$

Note that while this term also cancels modifications to the r and z directed momentum resulting from density diffusion, modification to angular momentum is not compensated for. This method requires that ζ is spatially constant so that, in this case $\overline{\zeta}_n = \zeta\overline{\overline{\Delta}}\,\overline{n}$. Expressions for $\overline{f}_{\zeta\beta}$ that also conserve angular momentum can be derived if ζ is made to be spatially dependent, but this additional complication has been omitted for now.

Using expression in equation D.1 for $\overline{f}_{\zeta\beta}$, the total contribution to the volume integral of the β component of momentum per unit volume (where $\beta = r,\,z$) from terms associated with density diffusion is

$$\dot{P}_\beta|_\zeta = \overline{dV}^T * \left\{\left(\frac{\partial}{\partial t}\left(m_i\,\overline{n}\,\overline{v}_\beta\right)\right)_\zeta\right\}$$

$$= \overline{dV}^T * \left\{m_i\,\overline{\zeta}_n\,\overline{v}_\beta + \overline{f}_{\zeta\beta}\right\}$$

$$= \overline{dV}^T * \left\{m_i\,\zeta\left(\overline{\overline{\Delta}}\,\overline{n}\right)\overline{v}_\beta + \frac{1}{2}m_i\,\zeta\left[\widehat{\overline{W}}*\left(\left(\overline{\widehat{\overline{\nabla}}}\,\overline{n}\right)\cdot\left(\overline{\widehat{\overline{\nabla}}}\,\overline{v}_\beta\right)\right) + \widehat{\overline{\nabla}}\cdot\cancel{\left(\widehat{v}_\beta\left(\overline{\widehat{\overline{\nabla}}}\,\overline{n}\right)\right)} - \overline{v}_\beta\left(\overline{\overline{\Delta}}\,\overline{n}\right)\right]\right\} \quad \text{(use eqn. 2.20)}$$

$$= \frac{1}{2}m_i\,\zeta\,\overline{dV}^T * \left\{\widehat{\overline{W}}*\left(\left(\overline{\widehat{\overline{\nabla}}}\,\overline{n}\right)\cdot\left(\overline{\widehat{\overline{\nabla}}}\,\overline{v}_\beta\right)\right) + \overline{v}_\beta\left(\overline{\overline{\Delta}}\,\overline{n}\right)\right\}$$

$$= \frac{1}{2}m_i\,\zeta\left[\widehat{\overline{dV}}^T*\left\{\left(\overline{\widehat{\overline{\nabla}}}\,\overline{n}\right)\cdot\left(\overline{\widehat{\overline{\nabla}}}\,\overline{v}_\beta\right)\right\} + \overline{dV}^T*\left\{\overline{v}_\beta\left(\widehat{\overline{\nabla}}\cdot\left(\overline{\widehat{\overline{\nabla}}}\,\overline{n}\right)\right)\right\}\right] \quad \text{(use eqn. 2.11)}$$

$$\Rightarrow \dot{P}_\beta|_\zeta = 0 \quad \text{(use eqn. 2.18)}$$

Note that in the last step, identity 2.18 has been used, with $\widehat{\mathbf{P}} = \overline{\widehat{\overline{\nabla}}}\,\overline{n}$ and $\overline{U} = \overline{v}_\beta$.

The total contribution to energy associated with v_β (where $\beta = r,\,\phi,\,z$) from terms associated with density diffusion is

$$\dot{U}_\beta|_\zeta = \overline{dV}^T * \left\{\left(\frac{\partial}{\partial t}\left(\frac{1}{2}m_i\,\overline{n}\,\overline{v}_\beta^2\right)\right)_\zeta\right\}$$

$$= \overline{dV}^T * \left\{\frac{1}{2}m_i\,\overline{\zeta}_n\,\overline{v}_\beta^2 + \overline{v}_\beta\,\overline{f}_{\zeta\beta}\right\}$$

$$= \overline{dV}^T * \left\{\cancel{\frac{1}{2}m_i\,\zeta\left(\overline{\overline{\Delta}}\,\overline{n}\right)\overline{v}_\beta^2} + \frac{1}{2}m_i\,\zeta\,\overline{v}_\beta\left[\widehat{\overline{W}}*\left(\left(\overline{\widehat{\overline{\nabla}}}\,\overline{n}\right)\cdot\left(\overline{\widehat{\overline{\nabla}}}\,\overline{v}_\beta\right)\right) + \widehat{\overline{\nabla}}\cdot\left(\widehat{v}_\beta\left(\overline{\widehat{\overline{\nabla}}}\,\overline{n}\right)\right) \cancel{- \overline{v}_\beta\left(\overline{\overline{\Delta}}\,\overline{n}\right)}\right]\right\}$$

$$= \frac{1}{2}m_i\,\zeta\,\overline{dV}^T * \left\{\overline{v}_\beta\left[\widehat{\overline{W}}*\left(\left(\overline{\widehat{\overline{\nabla}}}\,\overline{n}\right)\cdot\left(\overline{\widehat{\overline{\nabla}}}\,\overline{v}_\beta\right)\right) + \widehat{\overline{\nabla}}\cdot\left(\widehat{v}_\beta\left(\overline{\widehat{\overline{\nabla}}}\,\overline{n}\right)\right)\right]\right\}$$

$$= \frac{1}{2}m_i\,\zeta\left[\widehat{\overline{dV}}^T*\left\{\widehat{v}_\beta\left(\left(\overline{\widehat{\overline{\nabla}}}\,\overline{n}\right)\cdot\left(\overline{\widehat{\overline{\nabla}}}\,\overline{v}_\beta\right)\right)\right\} + \overline{dV}^T*\left\{\overline{v}_\beta\left(\widehat{\overline{\nabla}}\cdot\left(\widehat{v}_\beta\left(\overline{\widehat{\overline{\nabla}}}\,\overline{n}\right)\right)\right)\right\}\right] \quad \text{(use eqn. 2.9)}$$

$$\Rightarrow \dot{U}_\beta|_\zeta = 0 \quad \text{(use eqn. 2.18)}$$

In the last step, identity 2.18 has been used again, now with $\widehat{\mathbf{P}} = \widehat{v}_\beta\left(\overline{\widehat{\overline{\nabla}}}\,\overline{n}\right)$ and $\overline{U} = \overline{v}_\beta$.

Hence, the modification to total system energy due to density diffusion is canceled with the inclusion of the correction terms using either correction model, thereby ensuring maintenance of global energy conservation. Conservation of angular momentum is maintained using the first model only, but that model is suitable only for simulations that don't involve steep density gradients. Both models compensate for the modifications to radially and axially directed momentum associated with density diffusion.

References

[1] J. B. Perot, *Discrete Conservation Properties of Unstructured Mesh Schemes*, Annual Review of Fluid Mechanics, Vol.43, p.299-318 (2011)

[2] E. J. Caramana, D. E. Burton, M. J. Shashkov, and P. P. Whalen, *The Construction of Compatible Hydrodynamics Algorithms Utilizing Conservation of Total Energy*, J. Comput. Phys. 146, 227–262 (1998)

[3] L. G. Margolin, M. Shashkov, and P. K. Smolarkiewicz, *A discrete operator calculus for finite difference approximations,* Comput. Methods Appl. Mech. Eng. 187 (2000)

[4] X. Zhang, D. Schmidt, and B. Perot, *Accuracy and Conservation Properties of a Three-Dimensional Unstructured Staggered Mesh Scheme for Fluid Dynamics*, J. Comput. Phys. 175, 764–791 (2002)

[5] D. Derigs, A. R. Winters, G. J. Gassner, and S. Walch, *A novel high-order, entropy stable, 3D AMR MHD solver with guaranteed positive pressure*, J. Comput. Phys. 317, 223–256 (2016)

[6] J. G. Liu and W. C. Wang*, An Energy-Preserving MAC–Yee Scheme for the Incompressible MHD Equation*, 174, 12–37 (2001)

[7] E. Franck, M. Hölzl, A. Lessig, and E. Sonnendrücker, *Energy conservation and numerical stability for the reduced MHD models of the non-linear JOREK code*, ESAIM: M2AN 49, 1331 (2015)

[8] T. Hughes, G. Engel, L. Mazzei, and M. G. Larson, *The Continuous Galerkin Method Is Locally Conservative*, J. Comput. Phys. 163, 467–488 (2000)

[9] J. B. Perot, *Conservation properties of unstructured staggered mesh schemes*, J. Comput. Phys. 159, 58 (2000)

[10] M. Shashkov and S. Steinberg, *Support-operator finite-difference algorithms for general elliptic problems*, J. Comput. Phys. 118:131 (1995)

[11] C. Dunlea, *Magnetic Compression of Compact Tori - Experiment and Simulation*, Ph.D. dissertation (University of Saskatchewan, 2019)

[12] C. Dunlea, S. Howard, W. Zawalski, K. Epp, A. Mossman, General Fusion Team, C. Xiao, and A. Hirose, *Magnetic Levitation and Compression of Compact Tori*, Phys. Plasmas 27, 062513 (2020)

[13] https://www.particleincell.com/2012/matlab-fem/

[14] G. Strang, *Computational Science and Engineering*, Wellesley-Cambridge Press, (2007)

[15] P. O. Persson and G. Strang, *A Simple Mesh Generator in MATLAB.* SIAM Review, Volume 46 (2), pp. 329-345 (2004)

[16] P. O. Persson, *Mesh Generation for Implicit Geometries.* Ph.D. thesis, Department of Mathematics, MIT (2004)

[17] http://persson.berkeley.edu/distmesh/

[18] L. D. Cloutman, *A Note on Differencing the Viscous Dissipation Terms for a Newtonian Fluid*, Lawrence Livermore National Laboratory Report UCRL-ID-144159 (2001)

[19] S.C. Jardin, *Computational Methods in Plasma Physics*, Taylor and Francis, Boca Raton (2010)

[20] D. C. Meeker, *Finite Element Method Magnetics (*FEMM*)*, Version 4.0.1, http://www.FEMM.info.

[21] J. A. Crotinger, L. LoDestro, L. D. Pearlstein, A. Tarditi, T. A. Casper, and E. B. Hooper, *CORSICA: A comprehensive simulation of toroidal magnetic-fusion devices. Final report to the LDRD Program.* LLNL Report UCRL-ID-126284, doi:10.2172/522508 (1997)

[22] C. Dunlea, C. Xiao, and A. Hirose, *A model for plasma-neutral fluid interaction and its application to a study of CT formation in a magnetised Marshall gun*, Phys. Plasmas 27, 062103 (2020)